Characterization and modelling of quasi-static and fatigue notch effect in AZ31B-H24 rolled sheet

by

Lin Feng Qian

A thesis

presented to the University of Waterloo

in fulfillment of the

thesis requirement for the degree of

Master of Applied Science

in

Mechanical Engineering

Waterloo, Ontario, Canada, 2018

Author's declaration

I hereby declare that I am the sole author of this thesis. This is a true copy of the thesis, including any required final revisions, as accepted by my examiners.

I understand that my thesis may be made electronically available to the public.

Abstract

The transportation sector releases large amounts of harmful greenhouse gases into Earth's atmosphere. Vehicle weight reduction through the use of magnesium alloys is an effective way to reduce carbon dioxide emission and improve fuel economy. Magnesium is an attractive candidate for use as a structural material. In cars, notched structural members are common. Understanding of the fatigue behaviour of notched magnesium members is needed.

The monotonic and fatigue properties of AZ31B-H24 rolled sheet were characterized. It exhibits strong tensile-compressive yield asymmetry and weak anisotropy. At varying strain levels under strain-controlled loading, the response exhibits several characteristics, including yield asymmetry, mean stress evolution, cyclic strain hardening. Cyclic ratcheting is observed in stress-controlled tests with tensile mean stresses.

A finite-element model was created for the notched specimen. Three material models from Abaqus and LS-DYNA were compared. LS-DYNA material model 233 (MAT_233) was found to perform well in predicting residual strain at the notch root in quasi-static tension-unload as well as cyclic response under stress-controlled loading.

Smith-Watson-Topper (SWT) and Jahed-Varvani (JV) fatigue-life model parameters were obtained from fully-reversed strain-controlled tests on smooth specimens. The fatigue strength at 10 million cycles was estimated using a Weibull function to be about 80 MPa. A 'direct-fit' (df) method is proposed for SWT and JV. Fatigue life predictions using SWT, JV, SWT-df, and JV-df were compared against experimental stress-controlled tests. The direct-fit variants were found to be significantly better predictors of life under strain-controlled loading and marginally better under stress-controlled loading.

SWT with Miner's rule is able to predict reasonably the fatigue lives for variable-amplitude loading (VAL) strain-controlled tests. However, all of the models examined underestimate the fatigue life of notched specimens in VAL load-controlled tests.

Acknowledgements

I would like to express my sincerest gratitude to my supervisor, Dr. Hamid Jahed, and co-supervisor, Dr. Grzegorz Glinka, for the opportunity to work on this project and for their valuable advice and guidance over the entire course of my research.

I would also like to thank Dr. Ali Roostaei for his support and supervision and for sharing his strong knowledge and research experience.

Thanks to River Ling for the optical micrographs and texture measurements.

Thanks to my thesis committee – Dr. Hamid Jahed, Dr. Cliff Butcher, and Dr. Kevin Musselman for reviewing my thesis and seminar.

Thanks to the other members of Fatigue and Stress Lab – Dr. Behzad Behravesh, Dwayne Toscano, Sasan Faghih, Dr. Amir Yazdanmehr, Dr. Sugrib Shaha, Dr. Amir Pahlevanpour, Dr. Jie Wang, and Brent McCleave – for the discussions and constructive criticism.

Thanks to experts at Fiat Chrysler Automobiles (FCA) – Dr. Yung-Li Lee, Dr. Yibing Shi, Mohammed Malik, Umesh Dighrasker, and Marie Mills – for the quality discussions.

Thanks to FCA and NSERC for funding the project.

Thanks to my friends Jason Pan, Jimmy Zhou, Benjamin Tonita, and Clive Chan for proofreading my thesis.

Finally, I owe my deepest gratitude to my parents for their love and support.

Table of contents

List of figures

List of tables

Nomenclature

σ_{max}	Maximum tensile stress
ϵ_a	Strain amplitude
N_f	Number of cycles to fracture
$2N_f$	Number of reversals to fracture
E	Elastic modulus
σ_f'	Fatigue strength coefficient
ϵ_f'	Fatigue ductility coefficient
b	Fatigue strength exponent
c	Fatigue ductility exponent
ΔE_A	Energy due to purely tensile loading
E_e'	Axial fatigue strength coefficient
E_f'	Axial fatigue toughness coefficient
B	Axial fatigue strength exponent
C	Axial fatigue toughness exponent

Chapter 1: Introduction

1.1 Motivation

Climate change is a serious global threat which demands an urgent global response. Adverse impacts of climate change include, but are not limited to [1]:

- Increased flood risk and reduced water supplies in India, China, and South America due to melting glaciers;
- Decreasing access to food due to declining crop yields;
- Decrease in fish stocks and harm to marine ecosystems due to ocean acidification;
- Permanent displacement of tens to hundreds of millions more people due to rising sea levels, heavier floods, and more intense droughts;
- Increased deaths due to malnutrition, heat stress, and vector-borne diseases due to higher temperatures in many areas;
- Reduced biodiversity due to mass extinction of ~15 – 40% of all species.

The consequences of climate change will become more damaging with increased warming [1]. Therefore, it is in humanity's best interest to minimize damage caused by climate change through the reduction of global warming. Greenhouse gases are the largest manmade influence on global climate, with carbon dioxide (CO_2) being one of the highest contributors to radiative forcing of the climate system [2] and the most significant greenhouse gas emitted by the transport sector [3], which accounts for 24% of global CO_2 emissions [4]. Increasing fuel economy could make the largest single contribution to reducing CO_2 emission by transportation [3]. Governments around the world have also adopted regulations requiring higher fuel economy over time, such as CAFE [5].

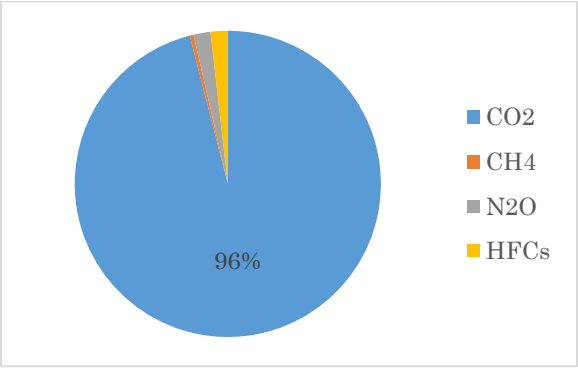

Figure 1 Greenhouse gas emission from vehicular sources [3].

Vehicle weight reduction is an effective option for improving fuel economy and reducing CO_2 emission. A 10% reduction in vehicle weight provides a 6-8% improvement in fuel economy for internal combustion engine (ICE) vehicles and 14% improvement in range for electric vehicles (EVs) [6]. Magnesium has several attractive features as a structural material for automotive applications [7]:

- Magnesium is the lightest engineering metal with a higher specific strength than aluminium [8].
- Magnesium has good ductility, damping, fatigue, and dent resistance characteristics, as well as machinability and thermal conductivity.
- Magnesium can be alloyed with a wide range of elements to improve its properties such as the strength-to-weight ratio.
- Magnesium is abundant on Earth as it is the eighth most common element.

Magnesium alloys have been used in automobiles in significant quantities since World War II with the Volkswagen Beetle, which contained over 20 kg of magnesium alloy per vehicle. At the time, the alloys AS41 and AZ81 were used to produce gearboxes and air-cooled engines. The uses of magnesium alloys at present include the drivetrain, vehicle interior, and other non-structural components in mass-manufactured vehicles [9]. For example, a die-cast AM50 Mg alloy replaced a steel radiator support in the Ford F-150, which saved over 9 kg in mass while maintaining performance [10].

Structural members usually have geometric discontinuities such as weld nuggets and connection holes which result in stress concentrations, so it is important for carmakers to be able to design notched members for magnesium alloys. To do so, a scientific understanding of both quasi-static and fatigue behaviour of notched magnesium members is required.

1.2 Objectives

This project was conducted by researchers at the Fatigue and Stress Analysis Lab (FATSLAB) at the University of Waterloo in partnership with Fiat-Chrysler Canada (FCA) with funding from FCA and the Natural Sciences and Engineering Research Council of Canada (NSERC) with the following objectives:

Characterize monotonic and cyclic material properties of AZ31B-H24 rolled sheet

Monotonic tensile and compressive tests are performed to establish monotonic material properties, and cyclic strain-controlled fully-reversed tests are performed to establish cyclic material properties. Smooth (un-notched) specimens are used. These properties are then used as the numerical basis for further analysis.

Characterize the behavior of AZ31B-H24 notched sheets under constant and variable amplitudes cyclic loads

Cyclic load-controlled fully-reversed and variable-amplitude load (VAL) tests are performed on notched specimens to evaluate existing theoretical models for notch analysis and fatigue-life analysis.

Develop methods for notch analysis in AZ31B-H24 with asymmetric cyclic behaviour

Neuber and Glinka methods of notch analysis are compared against experimental results from tests performed on notched specimens.

Evaluate fatigue life and damage models to find out if they are applicable to this material

Smith-Watson-Topper and Jahed-Varvani fatigue-life models are compared against experimental results from cyclic tests and evaluated for suitability to use with AZ31B-H24 rolled sheet.

Develop numerical finite element models and evaluate their predictive capability in terms of cyclic and quasi-static residual strains & stresses in notched asymmetric magnesium sheets

A finite element model of the notched specimen is created in LS-DYNA. Stress and strain values predicted by finite element simulations are used to generate a fatigue-life prediction and compared against experimental results on notched specimens.

Assess available material models for magnesium alloys

Two material models are found in LS-DYNA which may be suitable for use with magnesium alloys — MAT_124 and MAT_233. They are assessed in terms of their ability to model tensile-compressive yield asymmetry and anisotropy.

Explore the mean stress effect due to tensile-compressive yield asymmetry/effect of under and overloads

Due to tensile-compressive yield asymmetry which is present in all magnesium alloys, strain-controlled fully-reversed cyclic tests on a smooth specimen results in a stabilized hysteresis loop with nonzero mean stresses. This is different from 'symmetric' materials, which would produce a hysteresis loop with zero mean stress. The effects of this phenomenon are explored.

1.3 Thesis overview

This thesis consists of four major parts — background & literature review, material characterization, numerical modelling, and fatigue modelling — made up of six chapters.

Chapter 2 is a literature review on mechanical properties and behaviours of materials, including a discussion on unique aspects of magnesium alloys. Fatigue models and notch effect analysis are also discussed.

Chapter 3 presents experimental results from tests which characterize the properties of the magnesium alloy AZ31B-H24 rolled sheet in terms of its monotonic and cyclic properties.

Chapter 4 describes the setup of a finite element numerical model representing the notched specimen. The stress and strain values under elastoplastic loading predicted by the model is compared against experimental measurements.

Chapter 5 examines fatigue-life behaviour of both smooth and notched specimens and various methods are evaluated in terms of suitability for use with AZ31B-H24 rolled sheet. A novel approach to fatigue-life analysis is proposed and applied to the Smith-Watson-Topper and Jahed-Varvani models.

Chapter 6 concludes work presented in this thesis and recommends new directions for future research.

Chapter 2: Background & literature review

2.1 Material properties

Each material can be characterized by its unique behaviour under single and repeat loads. Mechanical deformation at a given load differs between different materials as well as between singularly applied load and repeatedly applied loads of the same material. Properties of a material under a single load are referred to as monotonic properties and properties under repeated (cyclic) loads are referred to as fatigue properties.

2.1.1 Monotonic

Engineering stress, S, is a measure of mechanical loading and is calculated from the applied load, P, and the original cross-sectional area of the specimen, A_0.

Engineering strain, e, is a measure of deformation and is calculated from the original and current gauge lengths on the specimen, l_0 and l, respectively.

$$S = \frac{P}{A_0}$$

$$e = \frac{l - l_0}{l_0}$$

While engineering stress and strain are based on a specimen's original dimensions, true stress, σ, and true strain, ϵ, relate to the instantaneous condition of the material and is usually more useful.

$$\sigma = \frac{P}{A}$$

$$\epsilon = \ln\frac{l}{l_0}$$

One can convert between engineering and true stresses and strains using the following relations, given that deformation in the material is uniform, i.e. necking has not occurred. When necking occurs, deformation becomes highly localized and strain is no longer uniform throughout the gauge section [11].

$$\sigma = S\,(1 + e)$$

$$\epsilon = \ln(1 + e)$$

The elastic modulus is defined as the slope of the stress-strain curve under elastic deformation, which is present at both initial loading as well as initial unloading. In the case of uniaxial loading, Young's modulus, E, is used.

$$E = \frac{\Delta S}{\Delta e}$$

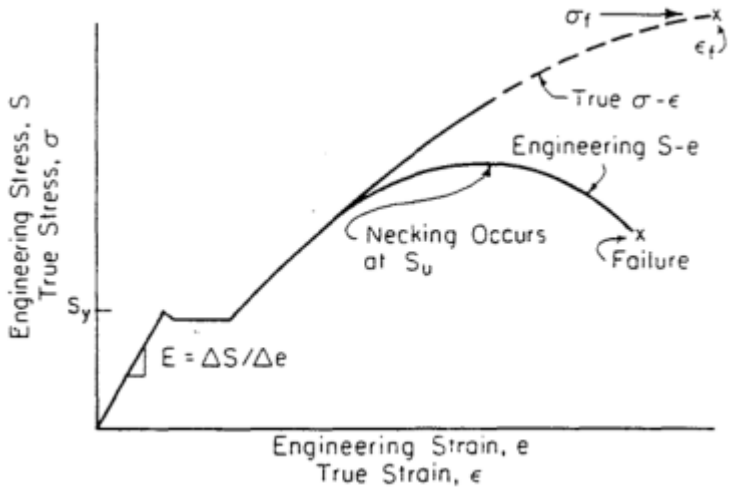

Figure 2 Engineering and true stress-strain relations representative of a typical steel [12].

Strain at any point can be decomposed into elastic strain and plastic strain. Elastic strain, ϵ_e, is the portion which is recovered upon unloading, and plastic strain, ϵ_p, is the portion which cannot be recovered on unloading. Together they sum to total true strain, ϵ_t.

$$\epsilon_t = \epsilon_e + \epsilon_p$$

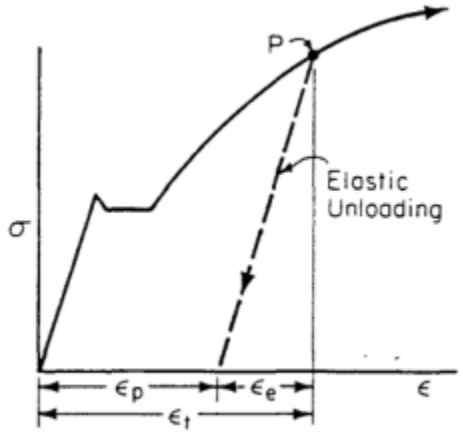

Figure 3 Elastic and plastic strain [12].

Yield strength is the stress at which plastic behaviour begins to be exhibited. For materials which have a smooth transition from elastic to plastic behaviour (i.e. no distinct yield point), the offset yield strength is used. It is found through the intersection of the stress-strain curve with a line parallel to the elastic modulus, starting from 0.2% strain and zero stress.

2.1.2 Fatigue

The cyclic elastic modulus is similar to the monotonic elastic modulus, except that it is calculated from the slope of the stable cyclic stress-strain response. The difference is usually small.

The stress range, $\Delta\sigma$, and strain range, $\Delta\epsilon$, are obtained directly from the stable hysteresis loop. They can also be represented in terms of amplitudes.

$$\epsilon_a = \frac{\Delta\epsilon}{2}$$

$$\sigma_a = \frac{\Delta\sigma}{2}$$

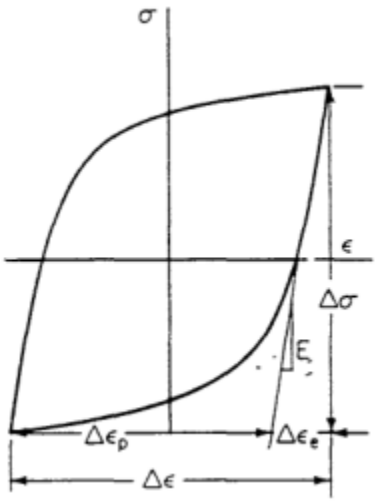

Figure 4 Stable cyclic stress-strain hysteresis loop [12].

The area within the hysteresis loop is the energy per unit volume dissipated during a cycle. This is work done by plastic deformation of the material [12].

2.2 Strain hardening

Ductile materials, such as most metals, exhibit a flattening of the stress-strain curve as plastic deformation occurs. Strain hardening behaviour in magnesium polycrystals resembles that of FCC polycrystals with a tendency to deform by planar glide; the dominant mechanism seems to be the accumulation of a forest of dislocations intersecting the main glide planes [13]–[16]. Hardening is affected by many factors such as type of deformation, deformation rate, temperature, dislocation distribution, crystal orientation, and alloying [16]. In some cases, the effect of temperature and strain rate on yield stress can be non-monotonic [17].

Bülfinger [18] and later Hollomon [19] proposed an empirical relationship between true stress and true plastic strain, where n is the Hollomon strain hardening exponent and K is the Hollomon strength coefficient.

$$\sigma = K\epsilon_p^n$$

Ramberg and Osgood [20] proposed an equation relating directly the true stress with true strain, which is suitable for describing cyclic stress-strain curves. n' is the Ramberg-Osgood cyclic strain hardening exponent and K' is the Ramberg-Osgood cyclic strength coefficient.

$$\epsilon = \frac{\sigma}{E} + \left(\frac{\sigma}{K'}\right)^{1/n'}$$

2.3 Magnesium alloys

Nomenclature of magnesium alloys generally follow the ASTM system [21]. For AZ series magnesium alloys, the A stands for aluminium (Al) and Z for zinc (Zn). AZ31 indicates that the magnesium is alloy is alloyed with ~3% aluminium and ~1% zinc by mass. The 'B' in AZ31B denotes that it is the second registered alloy in the AZ31 series. AZ31B is a wrought alloy with additionally ~0.6% manganese and small amounts of other elements [22]. Temper designation follows the alloy designation with a dash. In AZ31B-H24, 'H24' indicates that the wrought alloy is strain-hardened and then partially annealed [23]. This project focuses on AZ31B-H24 rolled sheet.

Aluminium and zinc are commonly used alloying elements in magnesium. Aluminium has the beneficial influence of enhancing hardness and strength. Aluminium and zinc together

increases strength without reducing ductility [24]. Zinc with nickel and iron impurities also improves corrosion resistance [25].

Wrought products refer to extrusions, forgings, and sheets. Wrought magnesium alloys as compared with their cast counterparts have better microstructural homogeneity and mechanical properties. AZ31B-H24 has good room temperature strength, ductility, corrosion resistance, and weldability. It is also nonmagnetic with high electrical and thermal conductivity [24].

Magnesium exhibits a tensile-compressive yield asymmetry, in which its compressive yield strength is significantly less than tensile yield strength. This is different from most steel and aluminium alloys, and also different from the strength-differential effect [26] seen in high strength steels. This behaviour comes from its hexagonal close-packed (hcp) crystal structure which limits its available slip systems and deformation twinning mechanism which occurs predominantly under compression [27]. In textured wrought products such as rolled sheets, the tensile-compressive yield asymmetry can be large.

Another mechanical characteristic observed in magnesium which differs from other common metals alloys is anisotropy. This is particularly strong in rolled sheets due both to the hcp crystal structure and the strong basal crystallographic texture from the rolling process [28] that makes the material behave differently in rolling and transverse directions.

There has been much research on the quasi-static and cyclic behaviour of magnesium alloys [29]–[41] and in particular AZ31B-H24:

- Characterization. Albinmousa et al. [42]–[45] studied the response of AZ31B extrusion under quasi-static and cyclic loads. They showed that both yield asymmetry and directional anisotropy are strong, and that the Jahed-Varvani (JV) energy-based model is capable of correlating AZ31B life under uniaxial and multi-axial loadings. Wu et al. (2010) [46] showed that texture and twinning/detwinning mechanisms strongly affect low-cycle fatigue behaviour of AZ31B-H24.
- Spot welds. Behravesh et al. [47]–[51] studied AZ31B-H24 rolled sheet under cyclic load and formulated its fatigue behaviour in similar and dissimilar spot welds. They also developed a finite element model to model the asymmetry of AZ31B-H24 rolled

sheet, and utilized that model to predict the life of an automotive demonstrative sub-assembly [52].

- Forging. Toscano et al. [53]–[56] and Grycuc et al. [57] studied the behaviour of AZ31B cast and extrusion under thermomechanical load and found that severe plasticity, such as through forging, at temperatures at 275 °C and above enhances the fatigue life of AZ31B significantly compared to the original cast material.
- Plasticity modelling. Noted among the research work on cyclic plasticity modeling of asymmetric and anisotropic behaviour of AZ31B are the work done by Noban et al. (2011) [58] and Roostaei and Jahed (2018) [59], which are able to model the unique cyclic stress-strain features of magnesium alloys. The model proposed by Noban et al. is based on a modified Armstrong-Fredrick nonlinear model [60], whereas the model proposed by Roostaei and Jahed is based on a Mises yield surface coupled with an anisotropic kinematic hardening rule based on Ziegler's rule [61], [62]. Kondori et al. (2018) [63] developed a quasi-crystal 3D plastic anisotropy model and verified the model using AZ31B-H24 sheets under quasi-static loading.
- Friction stir processing (FSP), friction stir welding (FSW), and cold spray. Darras et al. (2007) [64] found favourable changes in microstructure and mechanical properties of AZ31B-H24 after FSP, such as finer and more homogenized grains. Several groups have studied the change in quasi-static and cyclic properties in friction stir welded AZ31B-H24 with similar [65]–[71] and dissimilar materials such as aluminium 6061-T6 [72] and 5754-O [73], [74]. Marzbanrad et al. [75], [76] studied the effect on mechanical properties of cold spraying aluminium 7075 powder onto an AZ31B-H24 substrate and subsequent friction stir processing. Padmanaban and Balasubramanian (2010) [77] examined the influence of several welding processes — friction stir welding, laser beam welding, and pulsed current gas tungsten arc welding — on fatigue properties of AZ31B-H24.
- Other aspects. Wu et al. (2012) [78] investigated twinning-detwinning behaviour during fatigue crack propagation using in-situ neutron diffraction. Wu et al. (2007) [79] improved fatigue life of AZ31B-H24 by pre-straining via equal-channel-angular pressing (ECAP). Application of joining methods, such as laser assisted self-piercing riveting (LSPR) [80], ultrasonic spot welding (USW) [81], [82], fiber-laser-welding (FLW) and diode-laser-welding (DLW) [83], and adhesives [84], to AZ31B-H24 sheets

have also been examined by several groups. The use of AZ31B-H24 in fiber metal laminates (FMLs) have been studied in terms of general properties [85] and impact properties [86], [87].

2.4 Residual stress and strain

Residual stresses and strains are stresses and strains which are present in a part which is not subjected to an external force. They can be measured by X-ray methods or by measuring the changes in dimensions when a thin layer of material is removed from the surface. Residual stresses can arise when plastic deformation is not uniform throughout the entire cross section of the part being deformed, such as by bending or by applying load to a part with non-uniform cross section. [88]. The residual stress and strain, in this case, is due to plastic deformation, although other mechanisms, such as thermal loading and material phase transformation, can also cause residual stress and strain. Residual stress and strain can be beneficial or detrimental to a component's fatigue behaviour. For example, a compressive surface residual stress is beneficial to fatigue life [12].

2.5 Notch effect and analysis

In the presence of a geometric discontinuity such as a notch, the difference in geometry from uniform parts of a component causes stress and strain concentrations to occur near the discontinuity when the notched specimen is loaded. However, the fatigue life of a notched specimen does not decrease by a factor equal to the stress concentration factor [89]. This is due to the effective stress concentration affected by plastic flow of material and geometry of the notch root. At a high enough load, the stresses at the notch root exceed the material's elastic limit while stresses outside the notch region are still low and fully elastic. Several notch plasticity analysis models have been developed to calculate notch root stresses and strains, taking into consideration the material's yield behaviour, given the nominal load conditions. Two methods of notch analysis are Neuber's and Glinka's methods, which were developed by Neuber (1961) [90] and Molski and Glinka (1981) [91] respectively. Both were used in this project.

Neuber's method, or Neuber's rule, states that the theoretical stress concentration factor is equal to the geometric mean of the actual stress and strain concentration factors [90], which is intuitively reasonable because the stress concentration factor decreases and the

strain concentration factor increases as yielding occurs, while the theoretical stress concentration factor largely remains constant in the absence of general yielding [92].

$$K_t = \sqrt{K_\sigma K_\epsilon}$$

To calculate notch root stress-strain response given the applied load S, the following form of Neuber's equation [12] is used:

$$\sigma\epsilon = \frac{(K_t S)^2}{E}$$

Glinka's method, or equivalent strain energy density (ESED) method, is an energy-based method. The strain energy density at a location of a component under load can be calculated by taking the area underneath the stress-strain curve from the origin to the stress-strain point of the current state. This equation for Glinka's method relates the strain energy density at notch root to the applied load [91]:

$$\int_0^\epsilon \sigma(\epsilon)\, d\epsilon = \frac{(K_t S)^2}{2E}$$

Neuber's rule was found to overestimate significantly the local plastic strains at notch root [91]. Glinka's method is formulated to be less conservative than Neuber's, which may lead to better estimates.

A third method of obtaining stress and strain at a notch root, is through finite element analysis. This requires creating a 3D finite element model and the use of computational resources to solve but it can consider factors such as multiaxial stress states and irregular notch geometry.

Lastly, experimental measurements could be taken directly at the notch root using a strain gauge or a DIC system. However, this only gives the strain and not the stress.

Some recent advancements in understanding magnesium notch behaviour include the following:

- Denk et al. [93], [94] found wedge-shaped bands of twinned grains (BTGs) at notches of AM50 and AZ31B Mg alloys under compressive loading, located adjacent to the notch root on the specimen surface, and the measured strains within the formed

BTGs are strongly localized, up to ten times as high as the strains outside the BTGs. They also found that the high notch sensitivity of AM50 seen in the high-cycle fatigue regime (~10^6 cycles) decreases as fatigue life decreases for fully-reversed load tests with less than $1.5 \cdot 10^4$ cycles, which can also be associated with BTGs. Additionally, they proposed the concept of highly strained volume, its identification from optical strain field measurements, and application as a fatigue-life parameter.

- Karakas (2013) [95] studied notch mean stress effects in welded joints of AZ31 extruded sheet with AZ61A filler under axial loading and showed that fatigue life can be predicted using Smith-Watson-Topper (SWT) damage parameter, Masing loops, Neuber's rule, and applying the concept of reference radius developed by Sonsino et al. [96], [97].
- Kondori et al. (2018) [98] studied fatigue crack voids using synchrotron radiation laminography. They found the notch crack initiation sites to be affected by bluntness or sharpness of the notch, and crack growth to be anisotropic.
- Dallmeier and Huber (2012) [99] used linear elastic FEA with Masing loops and Neuber plasticity correction to model notched AZ31 sheet under cyclic loading and compared the results with experimental stress-controlled constant-amplitude load tests. They found that this method over-predicted fatigue life for smooth specimens and under-predicted fatigue life for notched specimens, possibly due to insufficient description of the hysteresis loops.

2.6 Fatigue modelling

2.6.1 Fatigue-life models

There are numerous damage models which correlate material properties and load conditions with life of a specimen. The Smith-Watson-Topper (SWT) model [100] is one of the most popular fatigue-life models used today. It applies to cases where the failure mechanism is predominantly tensile microcrack growth in the critical plane (maximum tensile strain or stress) and with a mean stress equal to zero.

$$\sigma_{\max}\epsilon_a = \frac{\left(\sigma_f'\right)^2}{E}\left(2N_f\right)^{2b} + \sigma_f'\epsilon_f'\left(2N_f\right)^{b+c}$$

The fatigue coefficients and exponents for the SWT equation come from the Coffin-Manson equation [101], [102], shown below. The elastic component of the equation (fatigue strength)

comes from the relation between the elastic strain amplitude and number of reversals. Similarly, the plastic component of the equation (fatigue ductility) comes from the relation between the plastic strain amplitude and number of reversals.

$$\epsilon_a = \frac{\sigma_f'}{E}\left(2N_f\right)^b + \epsilon_f'\left(2N_f\right)^c$$

The Jahed-Varvani (JV) model [103], [104] is a more recent energy-based fatigue-life model. It is analogous to Coffin-Manson as it has the same mathematical form as well as a distinction between the elastic and plastic components. The elastic component of the equation (fatigue strength) comes from the relation between the positive elastic energy, calculated from max stress and elastic modulus, and number of reversals. The plastic component of the equation (fatigue toughness) comes from the relation between the plastic strain energy, which is equal to the area within the hysteresis loop, and number of reversals.

$$\Delta E_A = E_e'(2N_A)^B + E_f'(2N_A)^C$$

Values from the stabilized hysteresis are used in all equations.

2.6.2 Cycle counting and damage accumulation for variable loads

In variable-amplitude load (VAL) tests, more than one hysteresis loop are present. The rainflow-counting algorithm [105] is used to reduce a complex spectrum of loads into sets of reversals, each corresponding to its own hysteresis loop.

By combining parameters from each hysteresis loop and number of repetitions with the Palmgren-Miner cumulative damage law (Miner's rule) [106], a prediction for the fatigue life can be obtained. Miner's rule states that permanent damage is induced in the material every cycle and that failure occurs after sufficient damage is accumulated. Damage per cycle is calculated using life prediction of another fatigue model. The cumulative damage law is represented by the following equation:

$$\sum \frac{n_i}{N_i} = 1$$

Where n_i is the number of repetitions of the cycle i per VAL block, and N_i is the fatigue life at a constant load level for the cycle i alone.

2.6.3 Mean stress effect

The formation and propagation of a fatigue crack, and subsequently the fatigue life, is greatly affected by the maximum tensile stress and the stress range in each hysteresis cycle. A cyclic test with a tensile mean stress results in a reduced fatigue life relative to a test with zero mean stress and the same stress range, and the opposite is true for compressive mean stress.

2.7 Test methods

2.7.1 Monotonic tests

A material's monotonic and fatigue properties are found through monotonic and fatigue tests, respectively.

A monotonic test consists of a test specimen loaded uniaxially with a slow, gradually increasing load until total fracture of the specimen occurs. The measured load and displacement data are then used to calculate the material's monotonic properties. The load can be tensile or compressive. Tensile test specimens are usually dog-bone shaped and compressive test specimens are usually cuboid or cylindrical.

2.7.2 Fatigue tests

Fatigue tests or cyclic tests include numerous variations, but all of them involve repeated, cyclic loading of the test specimen until fracture. Two common types of fatigue tests are the strain-controlled test and the stress- or load-controlled test.

In a strain-controlled test, the load levels are dependent on strain measurement at a small localized region. In a stress-controlled test, the nominal load applied by the test machine directly to the specimen is usually the value being controlled.

The strain ratio and stress ratio [107] are useful values in characterizing different types of loading. In strain-controlled tests, the strain ratio remains constant throughout the test. Similarly, in stress-controlled tests, the stress ratio remains constant.

$$R_{\text{strain}} = \frac{\epsilon_{\text{min}}}{\epsilon_{\text{max}}}$$

$$R_{\text{stress}} = \frac{S_{\text{min}}}{S_{\text{max}}}$$

The end levels of each load cycle may be the same or different. Constant-amplitude loading (CAL) refers to cases where the load path oscillates back and forth between maximum and minimum load levels. Variable-amplitude loading (VAL) refers to cases where not all load cycles are identical, with varying max and min end levels. Service loads on real life components are usually of variable amplitude, so VAL testing generally aims to reproduce and study the effects of the variable service loads in a laboratory condition.

2.8 Measurement

2.8.1 Extensometer

Extensometers are instruments which measure a change in distance. The extensometers used in this project were contact extensometers mounted to the specimen via strain gauge adhesive and rubber bands and were made by Epsilon and Instron.

2.8.2 Digital image correlation (DIC)

DIC is a measurement technique whereby one or more cameras can be used to capture images of specimens as they change over the course of the experiment. In solid mechanics and fatigue, we are usually interested in measuring surface strain. This is done by first applying a speckle pattern onto the surface of interest, and then tracking the changes in location of the black spots as they appear in each image.

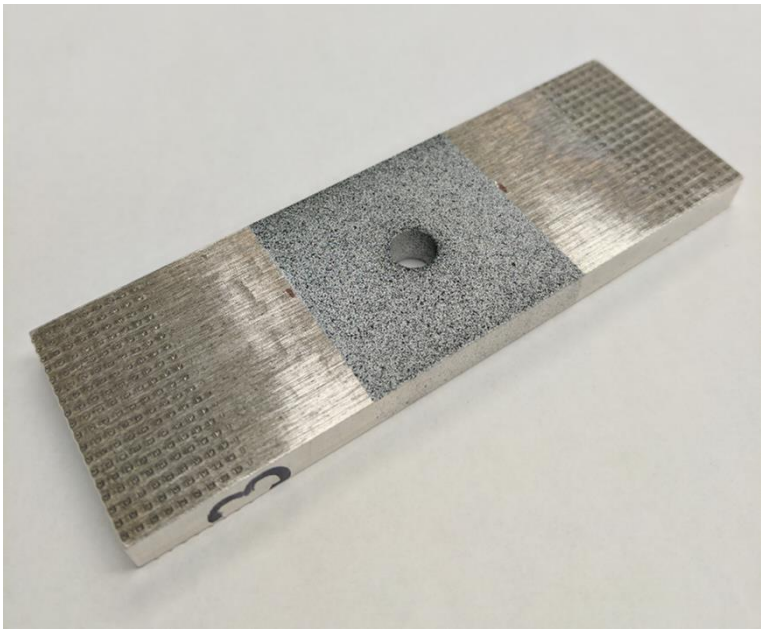

Figure 5 A notched test specimen used in this project made from 6.2 mm thick AZ31B-H24 rolled sheet. The area around the circular notch is spray-painted to obtain the speckle pattern used with DIC.

2.9 Numerical modelling

Finite element analysis (FEA) is a method to study numerical problems constrained by physical laws by creating and solving numerical models using the finite element method. FEA is often used to simulate an experiment to assist with experimental design and compared with experimental results to evaluate a theoretical model. In solid mechanics and fatigue, we are usually interested in solving for stresses and strains and studying the relations between externally applied remote loads and some geometric or material features somewhere on a specimen. The main advantage of FEA over other numerical methods is that it accurately represents complex geometry, so effects such as stress and strain concentration near a notch can be more accurately obtained.

Some examples of popular commercial off-the-shelf FEA software used in solid mechanics include Abaqus, Ansys, Code_Aster, LS-DYNA, and Nastran.

Chapter 3: Experimental setup and characterization of material properties

3.1 Material initial conditions

3.1.1 Chemical composition

The material studied in this project is AZ31B-H24 rolled sheet supplied by Magnesium Elektron with the chemical composition shown in Table 1. It is produced by rolling a cast ingot down to a thickness of 6.2 mm. Individual specimens were produced via CNC milling machine.

Table 1 Percentage chemical composition of magnesium alloy AZ31B as specified by ASTM [22].

Mg	Al	Zn	Mn	Si	Ca	Cu	Fe	Ni	Total other impurities
remainder	2.5-3.5	0.6-1.4	0.20-1.0	0.10	0.04	0.05	0.005	0.005	0.30

3.1.2 Microstructure and texture

Microstructure can be observed via optical micrographs, which are shown in Figure 6. The material directions are the rolling direction (RD), transverse direction (TD), and normal direction (ND) which is also the through-thickness direction of the rolled sheet. The grains at the surface of the rolled sheet are smaller than at the centre, which can be attributed to the higher deformation and faster rate of cooling at the surface of the sheet [108].

(a)

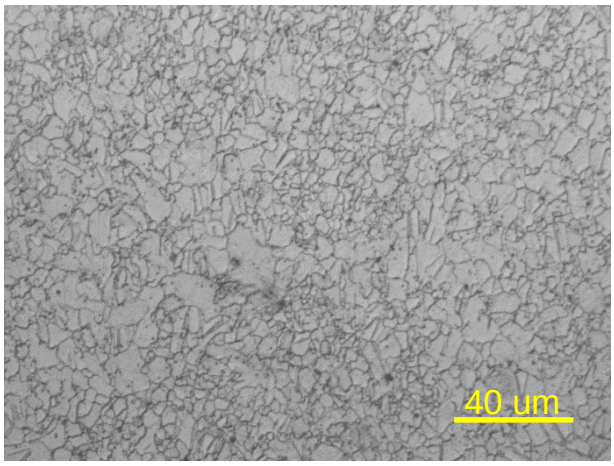

(b)

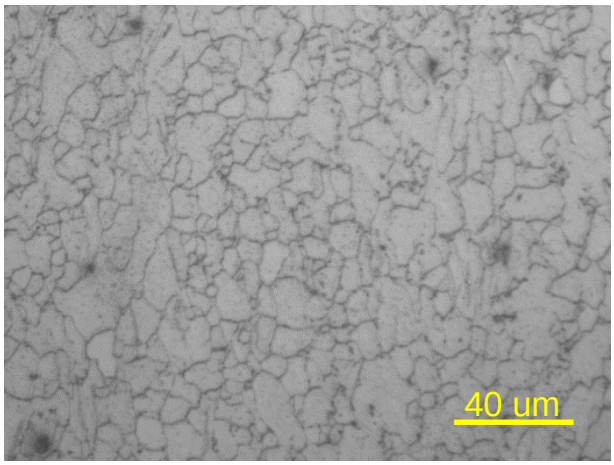

(c)

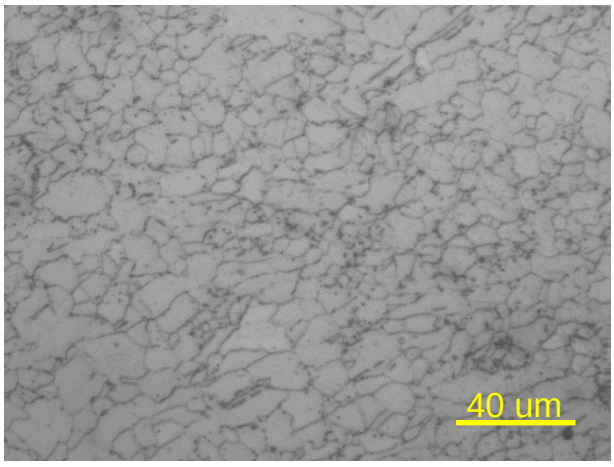

Figure 6 Optical micrographs of as-received AZ31B-H24 rolled sheet in the planes (a) RD-TD, (b) RD-ND, and (c) TD-ND. The RD-TD image was taken from the rolled sheet's outer surface; the others were taken from the centre.

Crystallographic texture measurements were performed; the (0 0 0 2) and the (1 0 $\bar{1}$ 0) pole figures are shown in Figure 7. The texture of the specimens is typical of rolled sheets. The dominant features are the alignment of the (0 0 0 2) (basal) poles with the normal direction (ND) and the uniform distribution of intensity around the perimeter in the (1 0 $\bar{1}$ 0) (prismatic) pole figure. This agrees with literature [109]–[111], [46]. Figure 8 illustrates some examples of crystal orientation found in the sheet.

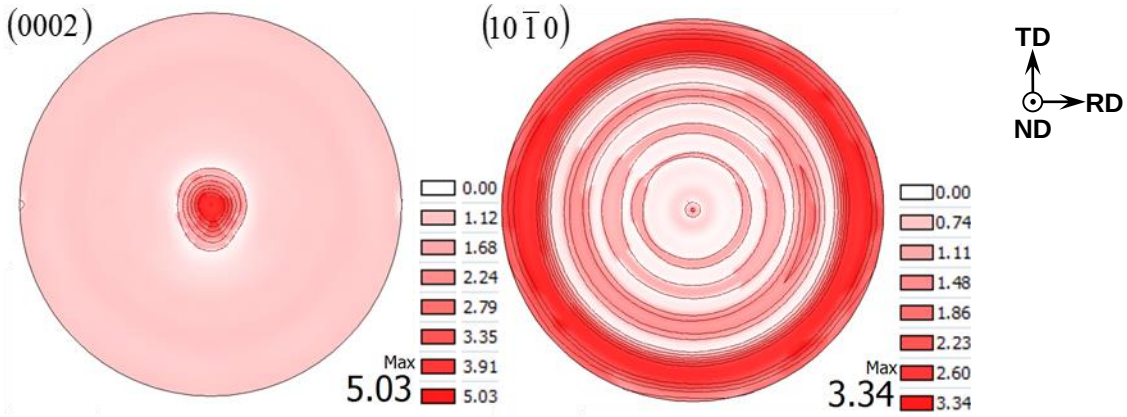

Figure 7 Experimental pole figures of as-received AZ31B-H24 rolled sheet.

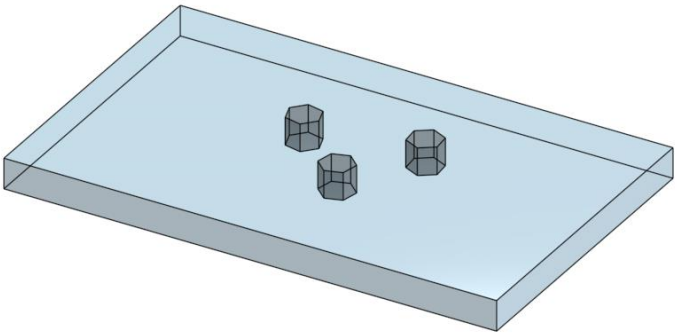

Figure 8 Schematic showing some examples of crystal orientations typically found in the as-received AZ31B-H24 rolled sheet.

3.2 Experimental design and setup

All monotonic tests were performed using a MTS 810 uniaxial servo-hydraulic universal test machine (UTM), which has a load capacity of 50 kN. Strain was measured using GOM ARAMIS 3D 5MP digital image correlation (DIC) system. Strain was controlled with a constant strain rate of 0.015 min^{-1}. All fatigue tests were performed using the MTS 810 and

Instron 8874. Strain measurements were done using Instron and Epsilon uniaxial extensometers. Strain gauge adhesives were used in mid- to high-cycle fatigue tests to allow testing at higher frequency without slippage of the extensometer from the test specimen. For each test case, 2 – 4 specimens were tested. The failure criterion for strain-controlled fatigue tests on smooth specimens was either 15% load drop or sudden fracture of the specimen, whichever one occurred first. For load-controlled tests on smooth specimens, it was sudden fracture. The failure criterion for notched specimens was detection of crack initiation, at about 100 µm. The notch in the notched specimens has an elastic stress concentration factor of 2.5.

The smooth tensile specimen geometry is shown in Figure 9. The compression specimen is a cuboid measuring 6 x 6 x 8 mm. The reason for the relatively thick (6.2 mm) specimens is to ensure that buckling does not occur under high compressive loads, without using an anti-buckling device.

The monotonic compression test was performed with the compression specimen in a special fixture (Figure 10b). Measurement was done using a DIC system. In order to eliminate any effect of dead zones at the top and bottom surfaces due to friction and barrelling [112] at the sides of the specimen, the analysis area used by DIC to calculate strain was specifically selected to include only the centre portion of the specimen. Measurement of the specimen dimensions after the test also indicated no significant barrelling.

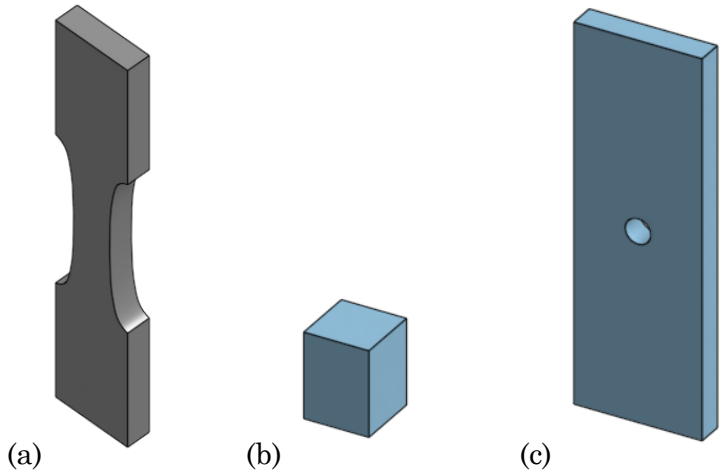

Figure 9 Smooth (a) tensile and (b) compressive specimens, and (c) notched specimen. Not shown to scale. Detailed specifications can be found in Appendix.

VAL strain-controlled tests were performed at three levels of maximum strain amplitude: 0.8%, 0.4%, and 0.25%. Two blocks were designed at max strain amplitude of 0.8%, two at 0.4%, one at 0.25%, and one random block at 0.25%. These VAL program blocks at different max strain amplitudes serve two different purposes:

- The VAL blocks at high max strain amplitude (0.8%) produce high enough plasticity in the stabilized hysteresis to demonstrate the difference in tensile and compressive reversals and to allow for comparison with CAL tests.
- The VAL blocks at low max strain amplitudes (0.4% and 0.25%) have much longer fatigue life, which is much more representative of practical service conditions. In addition, the hysteresis loops were balanced – repetitions of smaller loops were increased such that predicted fatigue damage distribution is not heavily biased toward the largest hysteresis loop, as is the case in the large max strain amplitude. This allows for evaluation on the applicability of Miner's rule on this material.

(a)  (b) 

Figure 10 Quasi-static testing of (a) tensile and (b) compressive specimens on the MTS 810 machine. Green masking tape was used to prevent reflection of light by the smooth metal test frame.

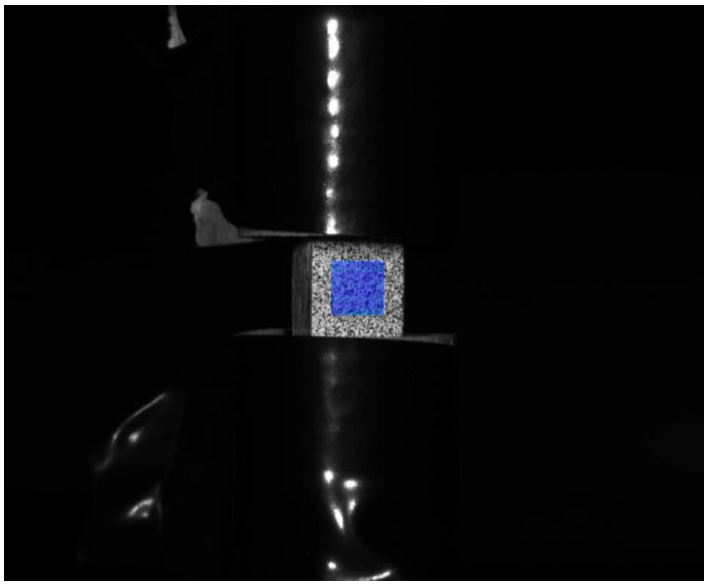

Figure 11 View of compression specimen from a DIC camera. Area highlighted in blue is used for analysis.

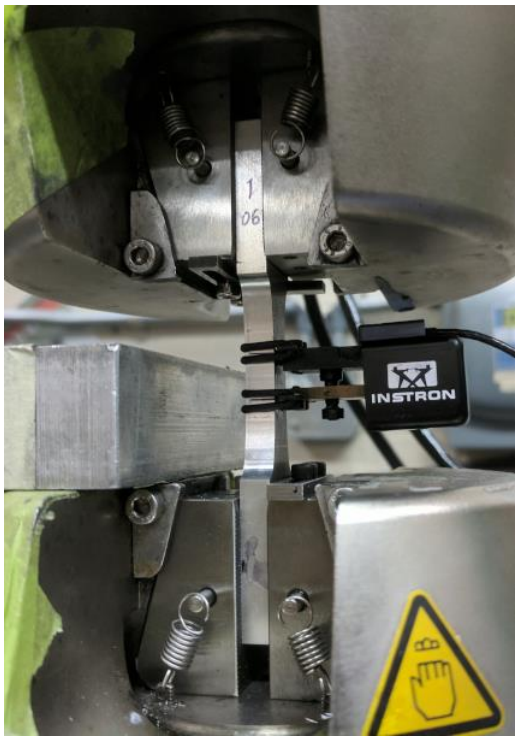

Figure 12 Fatigue testing of smooth specimen on the Instron 8874 machine with strain measurement by extensometer. A block of aluminium was placed beside the specimen as a physical safeguard against accidental crushing of the extensometer.

The following factors were considered when designing the strain-controlled VAL program blocks:

- Maximum strain amplitude and mean strain. To facilitate comparison with the fully-reversed strain-controlled CAL tests, mean strain of zero was selected. Fatigue life of the CAL tests with corresponding strain amplitudes were referenced as approximate upper limits for the VAL tests.
- Internal hysteresis loops locations and repetitions per block. To evaluate Miner's rule, it is desirable for total cumulative damage to be distributed across a variety of hysteresis loops, not dominated by the largest one. Cumulative fatigue contribution of each smaller loop can be altered by adjusting its strain end levels and repetitions per block.
- Load type and strain rate. As material mechanical behaviour differs at high strain rate, a low strain rate was selected along with ramp-type loading in order for the VAL tests to be consistent and comparable.
- Load sequence effect. All hand-designed VAL blocks (i.e. all except for the random block) were designed such that the max load would be achieved on the first reversal. This was done to ensure the VAL blocks have a similar load sequence and that the effect on fatigue life, if any, would be consistent.

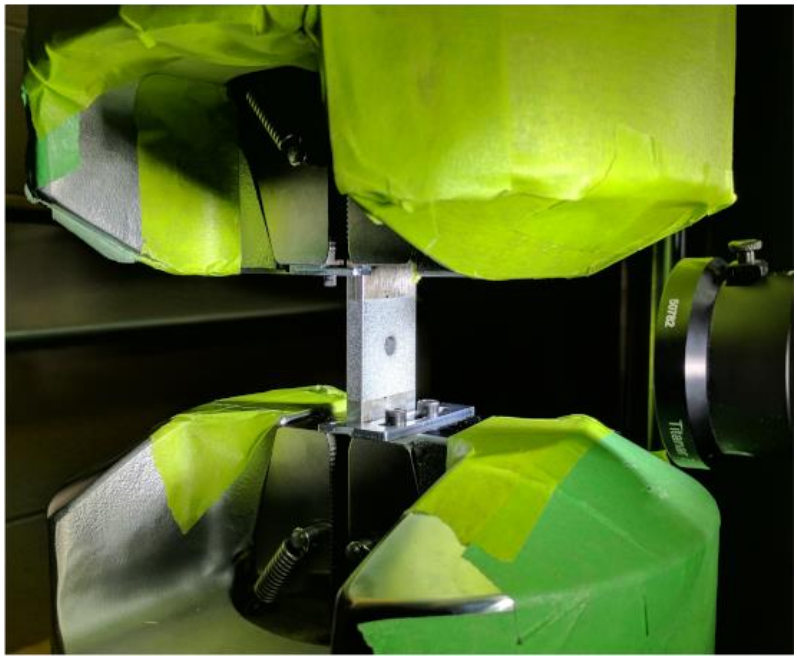

Figure 13 A notched specimen being tested on the MTS 810 machine. DIC camera is on the right.

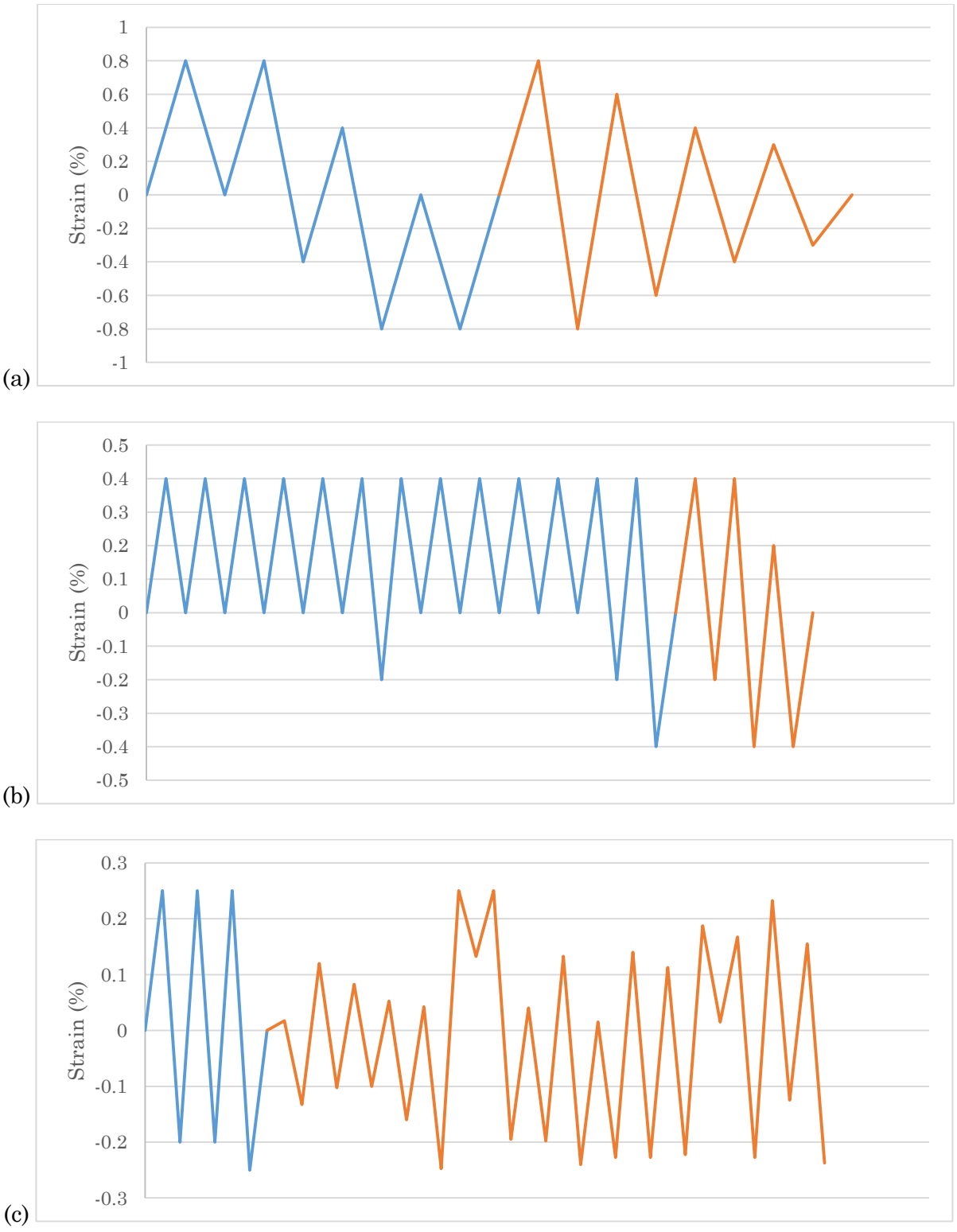

Figure 14 VAL test blocks at max strain amplitudes of (a) 0.8%, (b) 0.4%, and (c) 0.25%. The second block at 0.25% is random, the 5 other blocks were designed by hand. The different colours correspond to different blocks.

3.3 Characterization of monotonic properties

It is clear from the monotonic test results that AZ31B-H24 rolled sheet exhibits strong tensile-compressive yield asymmetry (Figure 15 and Table 2). The yield asymmetry is not present at the initiation of plastic strain, but arises subsequent to the initial yield. This is likely because a small amount of crystallographic slip activates first, and is followed immediately by deformation twinning [113]. Anisotropy also exists; it is greater in tension than in compression, and yield asymmetry is also smallest in rolling direction and greatest in transverse direction, which agrees with existing literature [114]. Anisotropy does not impact the stress-strain relation as significantly as yield asymmetry. It was decided for this project to focus on the tensile-compressive yield asymmetry due to its much greater influence than anisotropy on the mechanical response of AZ31B-H24.

The monotonic tensile stress-strain curves can be adequately represented using Hollomon's equation (Figure 16). This model fits particularly well in the rolling direction. In the transverse direction, the relation is slightly nonlinear. Model coefficients for Hollomon's equation are shown in Table 2.

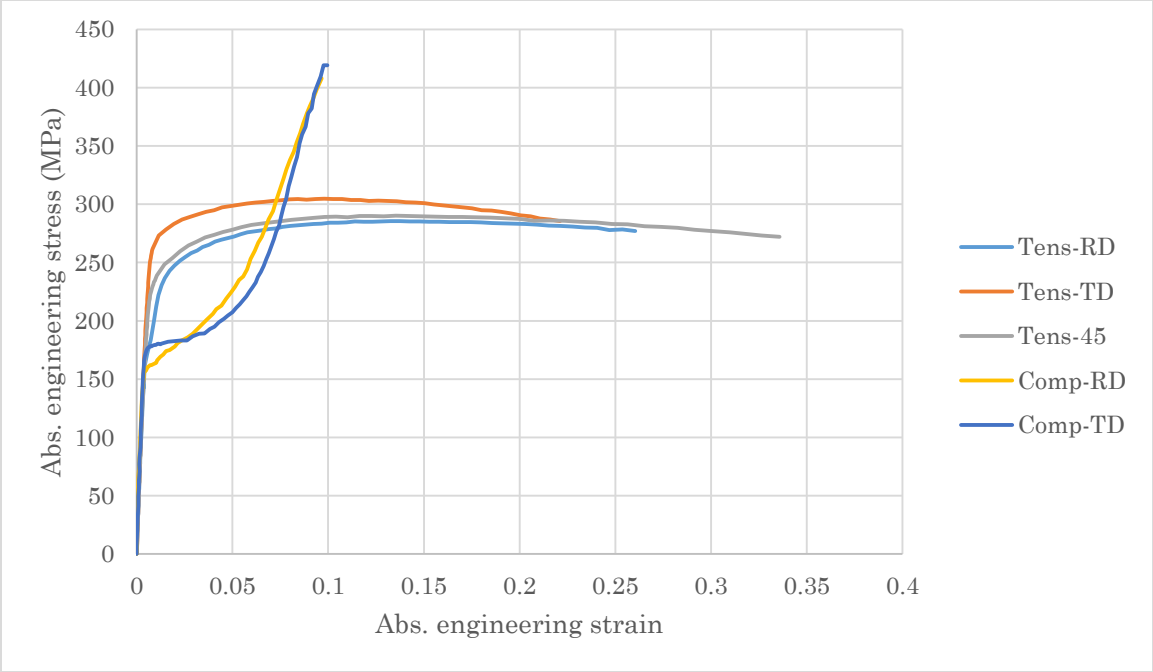

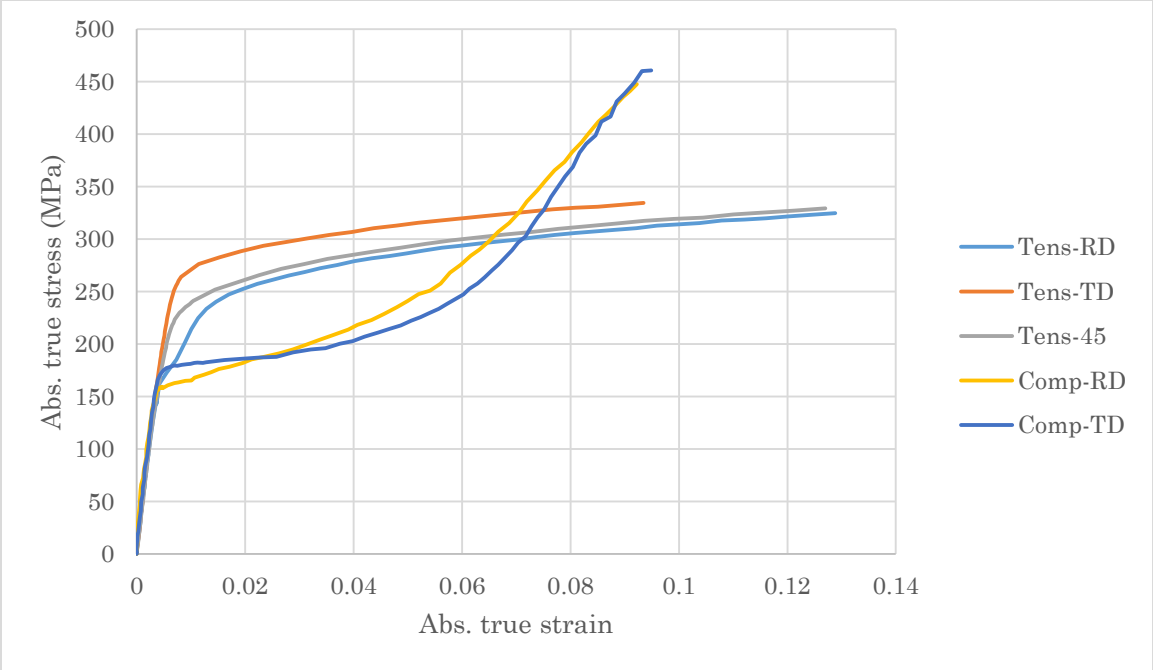

Figure 15 Experimentally obtained engineering and true stress-strain curves of AZ31B-H24 under monotonic tensile and compressive loading along various material orientations: rolling direction (RD), transverse direction (TD), and 45° direction (45).

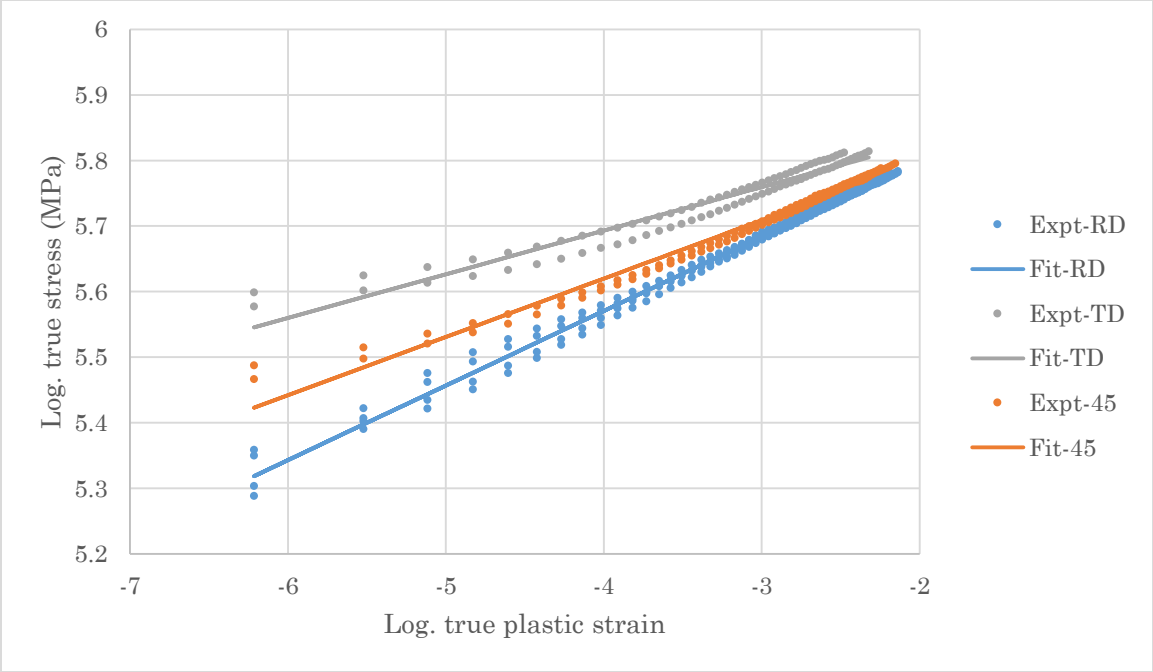

Figure 16 Fit of experimentally obtained logarithmic true stress and logarithmic true plastic strain to Hollomon's equation under monotonic tensile load along RD, TD, and 45° direction.

Table 2 Experimentally obtained monotonic material properties of AZ31B-H24 rolled sheet in each material direction.

	RD	TD	45°
Elastic modulus (GPa)	43.71	45.54	44.22
0.2% offset yield strength (YS) (MPa)	187	256	226
Ultimate tensile strength (UTS) (MPa)	287	303	290
Hollomon strain hardening exponent	0.1137	0.0665	0.0889
Hollomon strength coefficient (MPa)	414	387	394

3.4 Characterization of cyclic properties

Fatigue tests were performed on smooth tensile specimens in rolling direction. The tests consist of three types:

- Fully-reversed ($R_{\text{strain}} = -1$) constant-amplitude load (CAL) strain-controlled tests,
- Variable-amplitude load (VAL) strain-controlled tests,
- CAL stress-controlled tests with tensile mean stress and $R_{\text{stress}} = 0$.

Figure 17 shows that the tensile-compressive yield asymmetry becomes more noticeable with higher strain amplitudes. At low strain amplitudes, the tensile and compressive tips of the hysteresis loop are almost negatives of each other, similar to a yield-symmetric material. At high strain amplitudes, the upper reversal of the hysteresis loop takes on a distinct S-shape while the lower reversal bends and flattens after compressive yielding. For AZ31B-H24 rolled sheet, the asymmetry begins to occur between 0.7% and 0.8% strain amplitude (Figure 18). This non-Masing behaviour of which the hysteresis loop shape is dependent on plastic strain level was also observed by Matsuzuki and Horibe (2009) [115] in extruded AZ31.

Due to the tensile-compressive yield asymmetry, a nonzero mean stress is produced under fully-reversed strain-controlled loading. It can be seen that in the case of AZ31B-H24 rolled sheet, a tensile mean stress is produced, similar to observations by Hasegawa et al. (2007) [116] in AZ31 extruded bar. The main deformation mechanisms during cyclic loading are the formation of extension twins during compression and the de-twinning during subsequent tensile loading which was observed in extruded AZ31 by Huppmann et al. (2011) [117] via optical microscopy and electron backscatter diffraction (EBSD). They found that a major part of compressive plastic deformation is supported by the activation of extension twinning which saturates at around -8% strain. It is the main deformation mechanism affecting yield asymmetry in cyclic hysteresis loops.

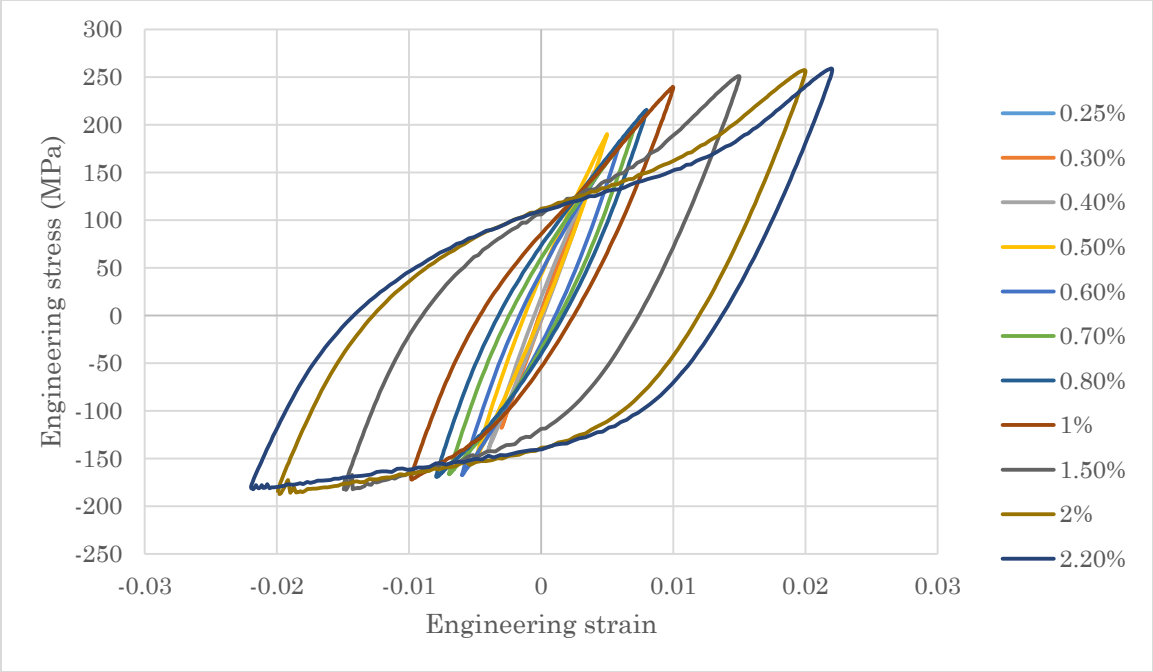

Figure 17 Stabilized cyclic stress-strain hysteresis loops at various strain amplitudes of AZ31B-H24 rolled sheet in rolling direction.

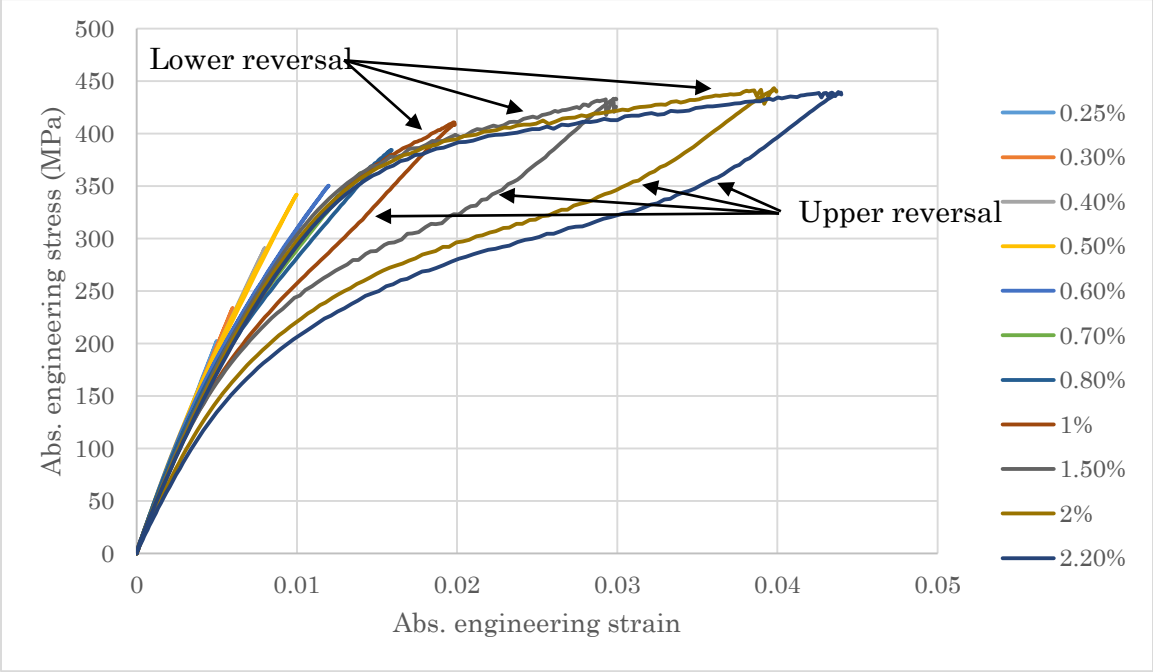

Figure 18 Upper and lower reversals of the stabilized hysteresis loops starting from origin at various strain amplitudes of AZ31B-H24 rolled sheet in rolling direction.

Tensile and compressive cyclic stress-strain curves were created separately by fitting the Ramberg-Osgood relation to tensile and compressive tips of stabilized hysteresis loops (Figure 19). When compared to quasi-static stress-strain curves, the cyclic curve exhibits significant higher strain hardening during tensile loading and negligible strain hardening during compressive loading.

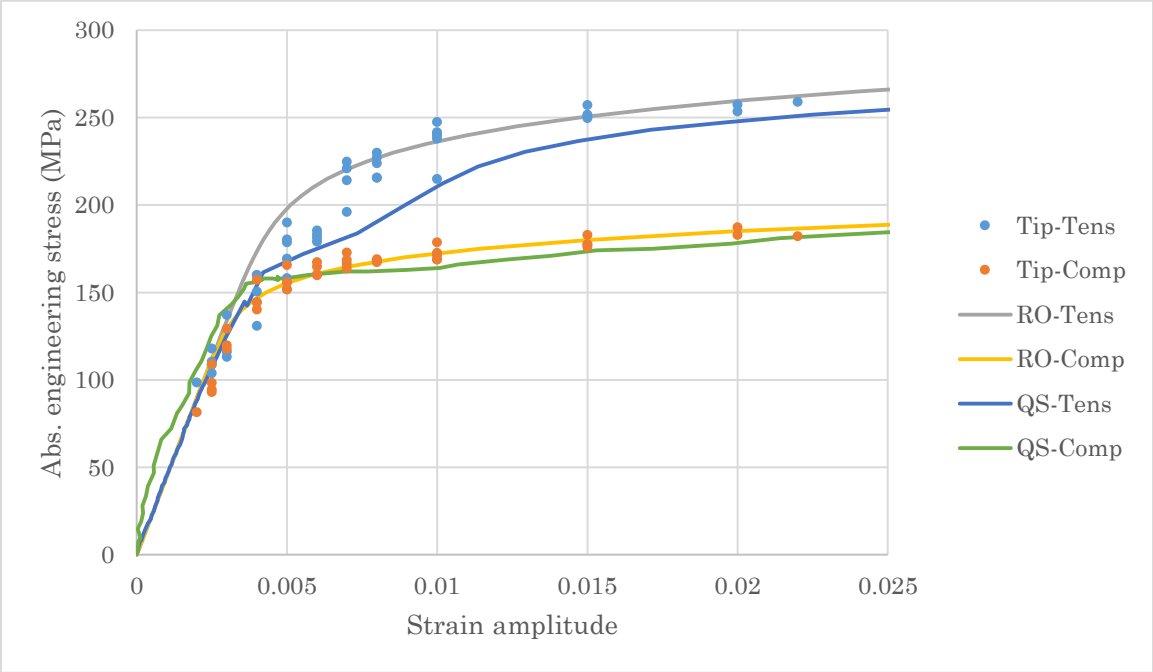

Figure 19 Hysteresis tip stress-strain values and Ramberg-Osgood cyclic stress-strain curves of AZ31B-H24 rolled sheet in rolling direction. Experimentally obtained quasi-static (QS) stress-strain curves are shown for comparison.

Table 3 Experimentally obtained cyclic material properties of AZ31B-H24 rolled sheet in rolling direction. Standard deviation is shown for cyclic elastic modulus.

Cyclic elastic modulus (GPa)	44.61 ± 1.99
Ramberg-Osgood cyclic strain hardening exponent - tensile	0.0848
Ramberg-Osgood cyclic strength coefficient (MPa) - tensile	372
Ramberg-Osgood cyclic strain hardening exponent - compressive	0.0746
Ramberg-Osgood cyclic strength coefficient (MPa) - compressive	252

Hysteresis loop evolution for the fully-reversed CAL strain-controlled tests varies by strain amplitude (Figure 20). In all cases, the half-life hysteresis loop encloses a smaller area than the second-cycle hysteresis loop. This effect is more significant at higher strain amplitudes.

Figure 21 shows the evolution of stress amplitude and mean stress over the life of a specimen at different strain levels. At high strain amplitudes (around 0.8%), cyclic hardening is observed until the sudden decrease in stress amplitude which corresponds with macroscopic cracking [115]. At low strain amplitudes (around 0.4%), cyclic softening is observed. For much higher or much lower strain amplitudes, there is no observable change in stress amplitude. For strain amplitudes between 0.8% and 0.4%, the behaviour gradually transitions from cyclic hardening to cyclic softening. These changes are more pronounced at the beginning of cyclic loading, but do not stabilize, instead continuing throughout the specimen's life (for example, 1% strain amplitude in Figure 21).

Cyclic strain hardening arises from interactions such as twinning and particles that impede the motion of dislocations, which can act as barriers to dislocation movement and cause hardening. In cyclic loading, dislocation pile-ups can cause back stress which impede the further movement of the dislocations and can also result in the strain hardening [88], [118], [119]. Cyclic strain softening is associated with dislocation annihilation and rearrangement [115]. Studies on single magnesium crystals found that secondary twinning produces a preferential alignment of the basal planes for slip, leading to softening, rapid unloading, high strains, and internal ductile failure [120], which suggests that this phenomenon may be the cause for cyclic strain softening in polycrystals. Additionally, it could explain the rapid unloading and then gradual recovery over several cycles visible most prominently in the mean stress evolution at 0.6% - 0.8% strain amplitudes (Figure 21). Cyclic strain hardening and softening are affected by factors such as grain size and crystal structure [118], [121].

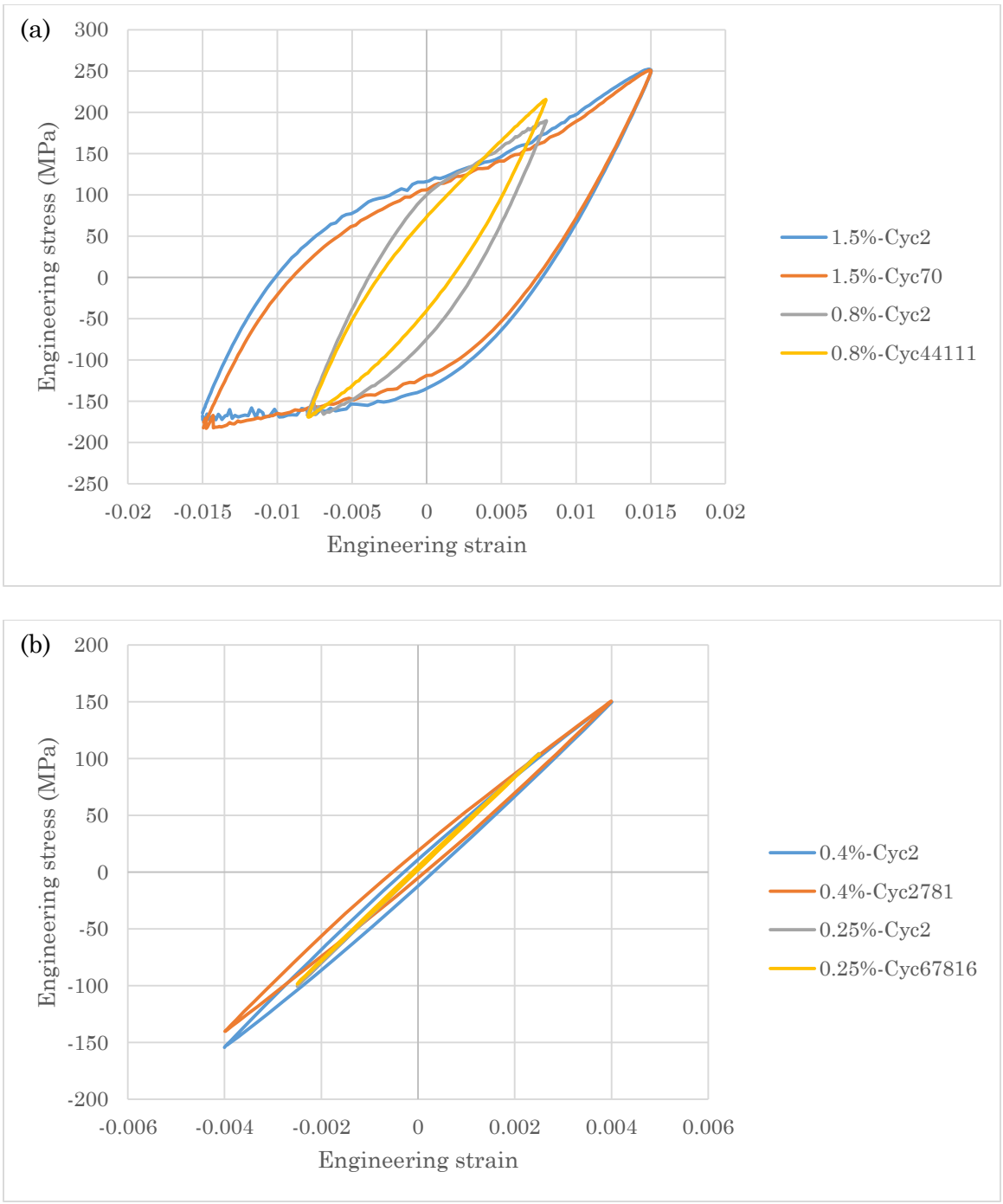

Figure 20 Hysteresis evolution from second-cycle to half-life at strain amplitudes of (a) 1.5%, 0.8%, (b) 0.4%, 0.25%.

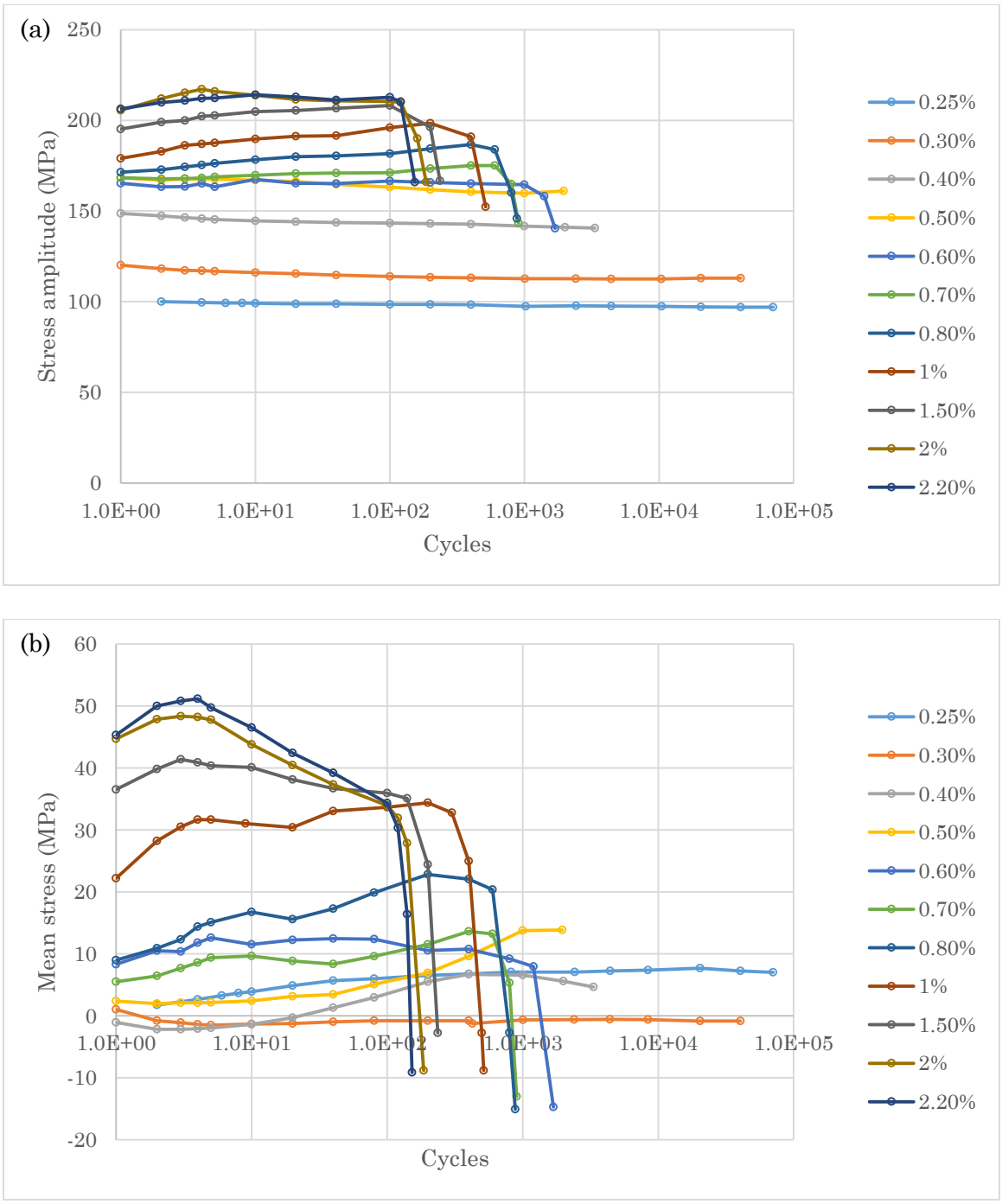

Figure 21 (a) Stress amplitude and (b) mean stress vs cycles for AZ31B-H24 rolled sheet under fully-reversed strain-controlled loading.

In all cases, the stress amplitude of the stabilized outer hysteresis loop matched with the CAL test with the corresponding strain amplitude (Figure 22). Some slight variance in mean stresses were also observed, such as at 0.4% strain amplitude.

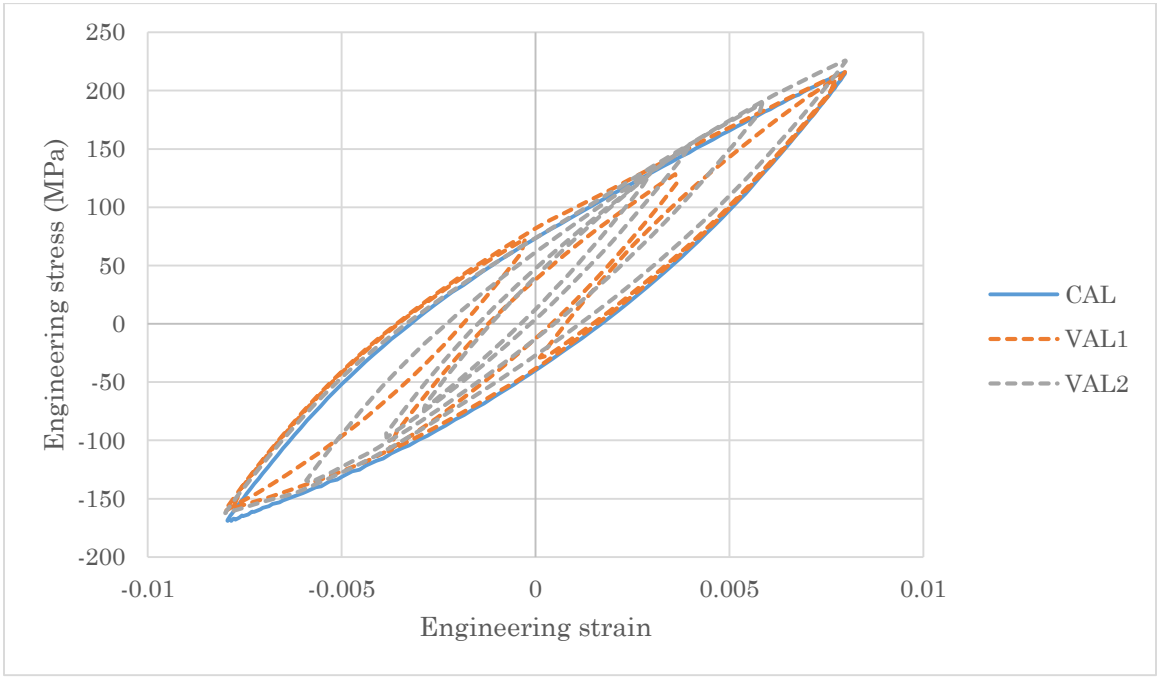

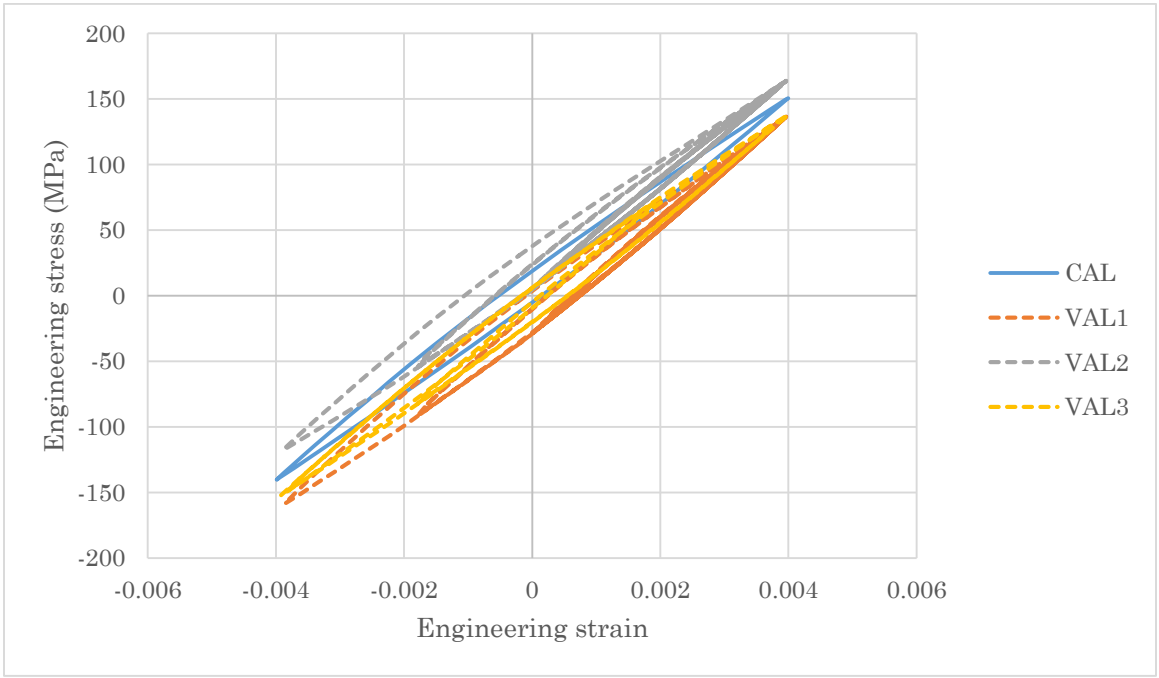

Figure 22 Hysteresis loops from CAL and VAL strain-controlled tests.

Under stress-controlled loading with tensile mean stress, cyclic creep / cyclic ratcheting [122] is observed, and the hysteresis loops do not stabilize. Figure 24 shows that increasing stress amplitude results in increased mean strain as well as increased change in mean strain per cycle. The asymmetric features of each hysteresis loop gradually disappear in the stress-controlled tests, contrary to strain-controlled tests in which hysteresis loop retain asymmetry until failure.

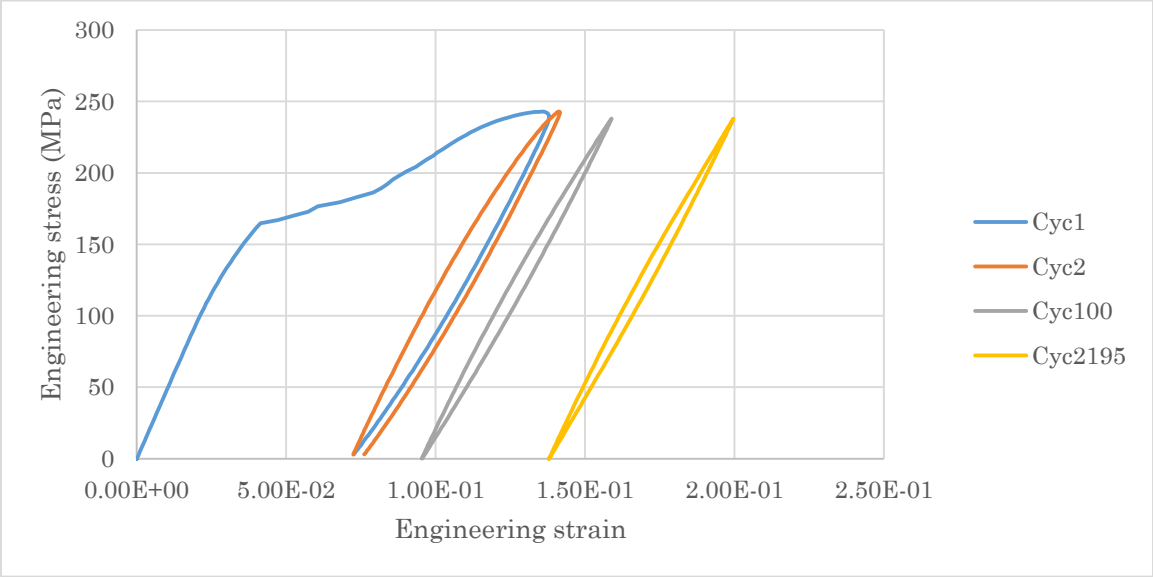

Figure 23 Cyclic response of AZ31B-H24 rolled sheet under stress-controlled loading with tensile mean stress.

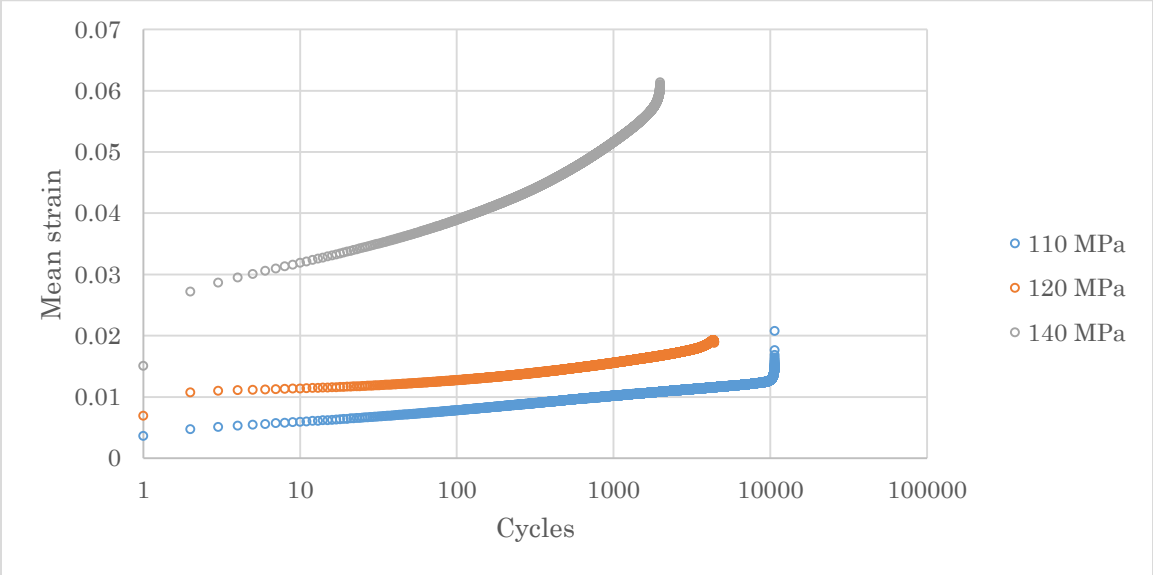

Figure 24 Evolution of mean strain over life of specimen under stress-controlled loading ($R = 0$) at stress amplitudes 110, 120, and 140 MPa.

3.5 Notch experiments

Uniaxial quasi-static and fatigue tests were performed on notched specimens in rolling direction. A quasi-static load-unload test was performed in order to compare with theoretical predictions of notch root strain. CAL and VAL fatigue tests were performed in order to compare with fatigue life model predictions. All images were taken at peak tensile load in the cycle or block.

3.5.1 Fatigue crack initiation

Two kinds of fatigue crack initiation were frequently observed in notched specimens: crack initiation at or very close to the notch root (Figure 25), and crack initiation away from the notch root (Figure 26).

Crack initiation at the notch root is intuitively expected behaviour, as it is the location of maximum stress concentration on the net cross-section plane of the specimen, which has the smallest area. Cracks which initiate here propagate transversely, reducing the effective cross-section area until sudden fracture occurs.

When a crack initiates at a significant distance from the notch root, it propagates up to a point and stops; then another crack, usually at the notch root, forms and propagates until final fracture occurs. Some possible explanations are discussed as follows:

- Phenomena associated with magnesium such as asymmetry and anisotropy might produce a condition in which the notch root, while experiencing maximum stress, has not exceeded the yield strength in that particular orientation and load case; meanwhile at another location, the stress has exceeded the corresponding local yield strength despite experiencing lower stress than the notch root.
- Denk et al. (2017) [93], [94] found bands of twinned grains (BTGs) at a similar distance offset from notch root in AM50 and AZ31B Mg alloy sheets undergoing uniaxial cyclic loading. Strain within the BTGs was significantly higher than surrounding areas and was also highly localized, and locations of the macroscopic initial cracks were found to be always located within the BTGs. This may explain the initial crack formation away from root.
- If the plane in which a crack propagates is not orthogonal to the loading axis, which could occur due to arrangements of grain size, shape, and orientation. Nano-scale

molecular dynamics simulations of fatigue crack growth in magnesium single crystals by Tang et al. (2010) [123] showed that fatigue crack propagation is strongly dependent on crystal orientation. It may be possible that the two surface cracks observed are actually one crack connected inside the specimen.

- Using scanning electron microscopy (SEM) on AM50 and AM60B, Wang et al. (2006) [124] found that a single fatigue crack formed at the notch root when notch is sharp with a small radius, and multiple small fatigue cracks formed at the notch root when notch is rounder with a larger radius. They suggested that the larger plastic field at the notch root resulted in the stresses and strains being approximately uniform over a larger area along the surface on which cracks may form, analogous to conditions at the surface of a smooth specimen.

All images were taken at peak tensile load in the cycle (under CAL) or VAL block.

(a) 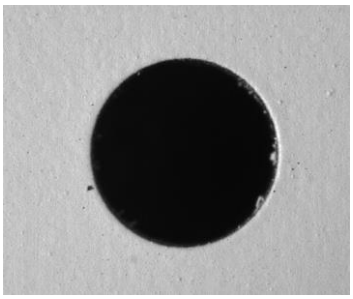 (b) 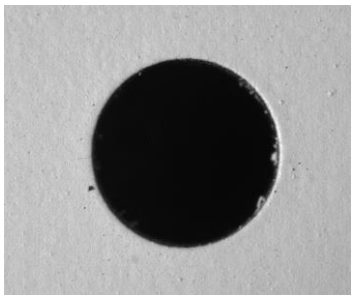 (c) 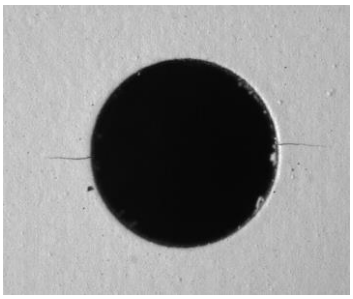

Figure 25 Crack initiation and propagation on a notched AZ31B-H24 specimen in which the cracks initiated at notch root. This test was CAL load-controlled at 50% CYS. Images were taken at (a) crack initiation (CI), (b) CI plus 2000 cycles, and (c) CI plus 4000 cycles.

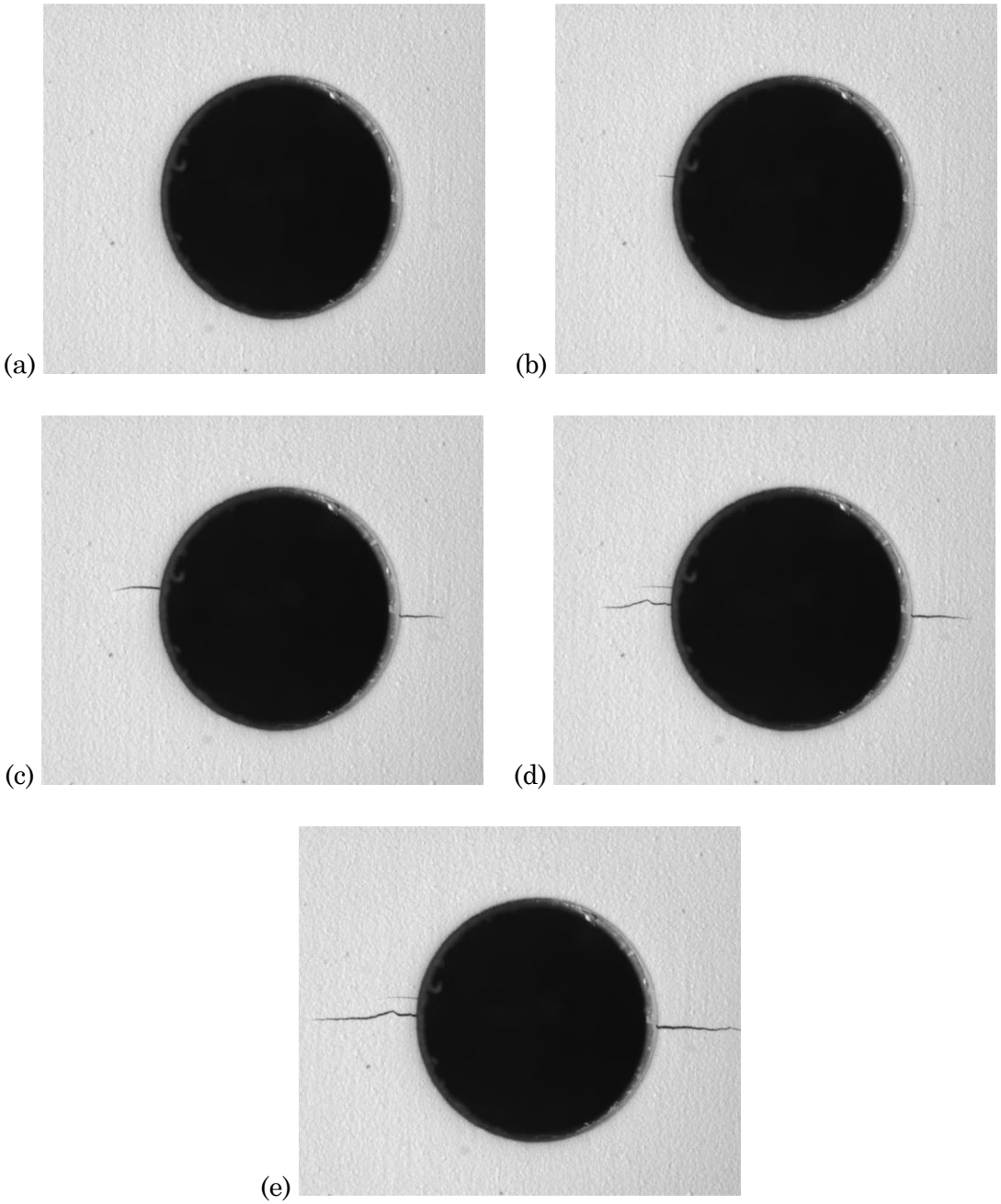

Figure 26 Crack initiation and propagation on a notched AZ31B-H24 specimen which shows multiple crack formation. This test was VAL load-controlled. Images were taken at (a) crack initiation (CI), (b) CI plus 150 blocks, which shows initiation of the first crack at about 10° from notch root, (c) CI plus 300 blocks, (d) CI plus 350 blocks, which shows initiation of another crack at notch root, and (e) CI plus 450 blocks, which shows propagation of the second crack while the off-centre crack remains arrested.

3.5.2 Notch root strain evolution

CAL load-controlled tests on notched specimens were performed. The gross nominal load levels were selected based on the equivalent net nominal stress at a percentage of the compressive yield strength (CYS). It is calculated via the following relation:

$$\sigma_n^{\text{gross}} = \sigma_n^{\text{net}} \frac{A^{\text{net}}}{A^{\text{gross}}}$$

Axial strain at the notch root was measured via DIC multiple times throughout the specimen's fatigue life, where each measurement consisted of 3 consecutive cycles. The evolution of maximum and minimum axial strains is shown in Figure 27. It can be observed that the mechanical response at the notch root is not strain-controlled, as both the max and min strains change over time. The rate of change in max and min strains also decreases, which is similar to the stress-controlled tests on smooth specimens.

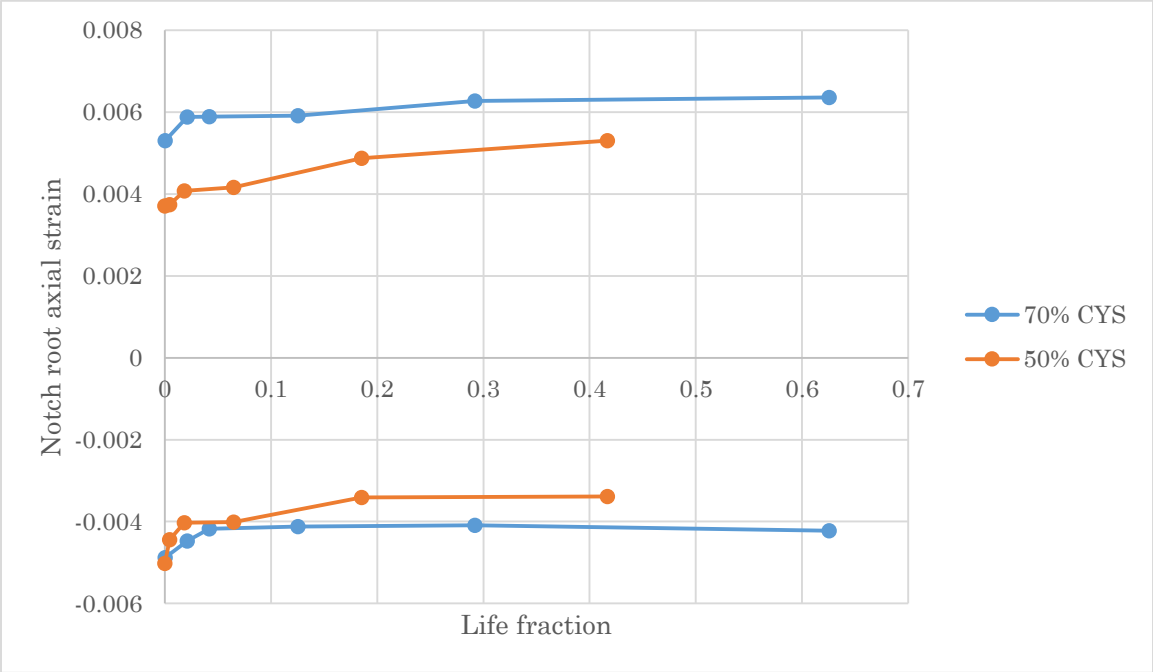

Figure 27 Maximum and minimum axial strains at notch root vs fraction of specimen fatigue life in CAL load-controlled tests.

Chapter 4: Numerical modelling of notch effect on deformation and plasticity

4.1 Capabilities and limitations of software

Abaqus and LS-DYNA were selected for this project. Two LS-DYNA material models type 124 and 233 were identified to be relevant. Table 4 compares capabilities of these software packages.

Table 4 Comparison of software built-in capabilities, i.e. without using user-defined materials or subroutines.

	Abaqus	**LS-DYNA MAT_124**	**LS-DYNA MAT_233**
3D solid elements	Yes	Yes	Yes, possible with MAGNESIUM option, otherwise only shell elements
Tensile-compressive yield asymmetry	No	Yes	Yes
Material anisotropy	Yes	No	Yes
Yield criterion	Mises, Hill, Drucker-Prager, Mohr-Coulomb, etc.	Modified Mises	Cazacu-Plunkett-Barlat 2006 [125]
Hardening rule	Isotropic, Johnson-Cook isotropic, kinematic, etc.	Isotropic	Isotropic; Distortional, possible with MAGNESIUM option

LS-DYNA MAT_124 models an isotropic elastic-plastic material implementing yield asymmetry by defining unique yield stress versus plastic strain curves for compression and tension [126]. It was found that MAT_124 uses a yield criterion based on the Mises yield criterion [127] with modifications to accommodate for the yield asymmetry. When the given tensile and compressive yield strengths are identical, the yield locus is equivalent to that of

Mises. When the given tensile and compressive yield strengths are different, the yield locus is made from 2 Mises yield loci and connecting curves. MAT_124 uses the mean stress or hydrostatic pressure, $\sigma_{\text{mean}} = (\sigma_x + \sigma_y + \sigma_z)/3$, along with tuning parameters PC and PT (both non-negative numbers, default zero) to determine whether to use the tensile or the compressive yield surface [128]:

$$\begin{cases} \sigma_{\text{mean}} > \text{PT} & \text{tensile yield surface} \\ -\text{PC} < \sigma_{\text{mean}} < \text{PT} & \text{interpolation between tensile and compressive yield surfaces} \\ \sigma_{\text{mean}} < -\text{PC} & \text{compressive yield surface} \end{cases}$$

The tuning parameters PC and PT can, therefore, be used to smoothen the transition from one yield surface to the other, as shown in Figure 28. When PC and PT are zero, a sharp transition is produced. MAT_124 also accommodates for the possibility of considering rate effects and failure, although these factors are not considered for this project.

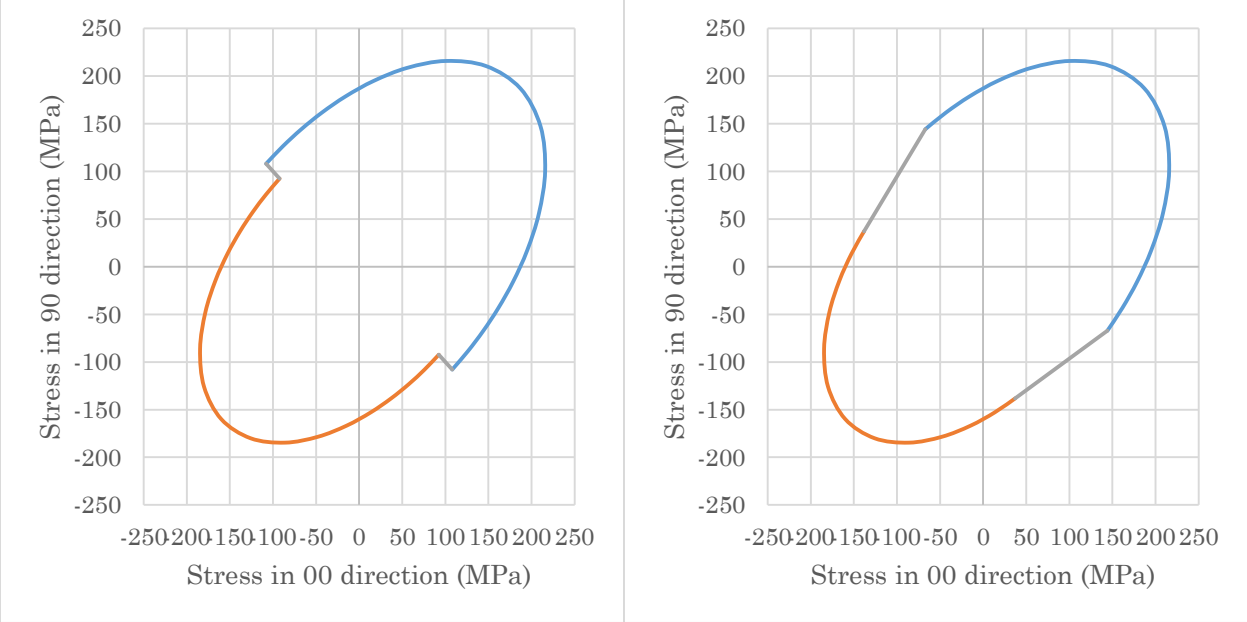

Figure 28 MAT_124 yield locus in principal stress space at zero plastic strain using tensile and compressive yield strengths of AZ31B-H24 rolled sheet in rolling direction. (a) PC = PT = 0, (b) PC = PT = 25 MPa.

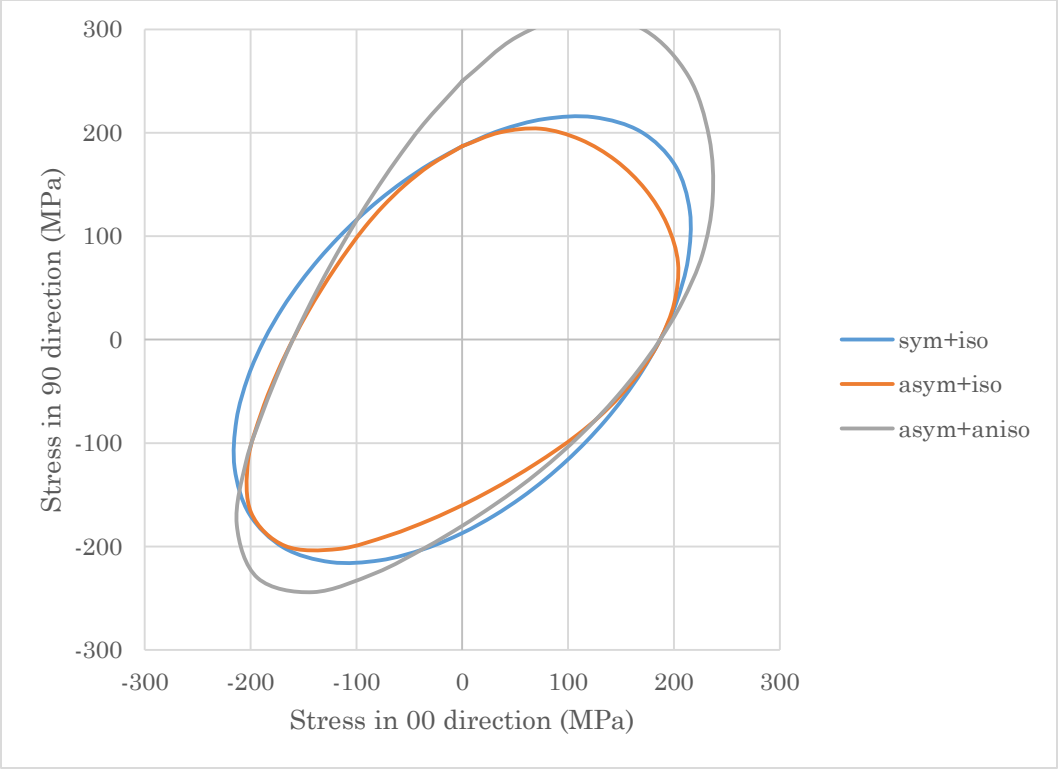

Figure 29 MAT_233 yield locus in principal stress space at zero plastic strain in three different configurations: symmetric and isotropic (equivalent to Mises), asymmetric and isotropic, and asymmetric and anisotropic.

LS-DYNA MAT_233 (Figure 29) is a model created specifically for hcp metals and is based on work by Cazacu, Plunkett, and Barlat (2006) [125]. Like MAT_124, it is capable of modelling yield asymmetry. Additional capabilities that are available but not used in this project are anisotropy, failure, and rate effects. The MAGNESIUM option invokes a material model developed specifically for magnesium alloys by U.S. Automotive Materials Partnership (USAMP) consortium [126]. The MAGNESIUM option was chosen to be used in this project. Features of the MAGNESIUM option include:

- The MAGNESIUM option allows for input of the hardening curves in terms of von Mises effective stress versus equivalent plastic strain, whereas without the option, the input curves must in the form of Cazacu-Barlat effective stress versus its energy conjugate plastic strain. Since von Mises stress is more widely used, this makes the material model simpler to work with.
- The MAGNESIUM option allows for distortional hardening when both tensile and compressive hardening curves are provided.

- The MAGNESIUM option allows MAT_233 to be used with 3D solid elements. Without activating this option, only shell elements can be used with this material model.

4.2 Finite element model setup

Notched specimen was modelled in Abaqus, LS-DYNA MAT_124, and LS-DYNA MAT_233 to solve for strain and stress fields for various scenarios:

- Quasi-static tension & unload
- Cyclic loading

4.2.1 Geometry

Model orientation is setup as follows:

- Rolling direction (RD) corresponds to y-axis
- Transverse direction (TD) corresponds to x-axis
- Normal direction (ND) corresponds to z-axis

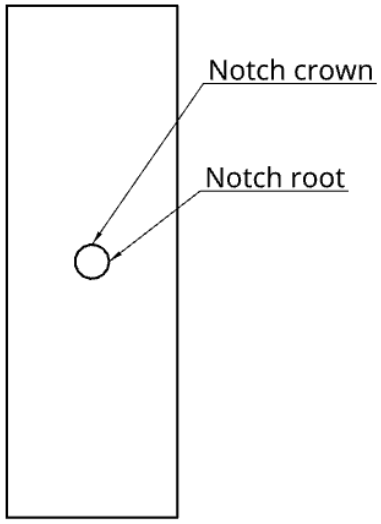

Figure 30 A notch root and notch crown are indicated for specimen with a circular notch loaded axially (vertically in this figure).

The finite element (FE) model is a 1/8-geometry model, as all responses are assumed to be symmetric for the simulated conditions (elastoplastic without modelling material failure). Symmetry boundary conditions are applied at cut faces (left, bottom, and rear). This greatly reduces computation time compared to a full-geometry model.

4.2.2 Mesh

The FE model is split into 3 partitions (Figure 31 and Table 5). To improve accuracy of results, the following considerations were implemented:

- Surface elements are generally smaller than those within the volume of the specimen.
- Elements in the notch region have low aspect ratio and roughly right angles (similar to cubes).
- The size of elements near the notch is small and selected based on a mesh convergence study (Table 6); It was decided that having 20 elements along notch edge was a suitable level of mesh refinement with a reasonable computation time while having a low error of < 1% from the converged solution.
- All elements are 3D solid brick quadratic (second order) elements; in Abaqus, C3D20 elements were used while in LS-DYNA, element formulation 2 (ELFORM=2) was used.

Figure 31 Partitions of the finite element model.

Table 5 Setup of partitions in finite element model.

Partition	Mesh	Approximate element size
Notch region which encloses volume within 2 radii from notch edge	Structured hexahedral	0.2 x 0.2 x 0.2 mm at surface
Region between notch and remote region	Unstructured hexahedral	Between 0.7 x 0.7 mm to 3 x 3 mm
Remote region	Structured hexahedral	3 x 3 mm

Table 6 Results of mesh convergence study by varying parameters in the notch region. The result parameter used is axial stress at specimen centre at notch root while the applied load was 10 MPa. The percentage difference is calculated by comparing each result to the result with the finest mesh — 80 elements along notch edge.

Nbr of elements along notch edge	Nbr of elements radially	Nbr of elements thru thickness	Total nbr of elements in entire model	Result parameter	% difference
3	2	1	74	33.8893	1.763
5	4	2	188	34.0005	2.097
5	4	8	752	34.0721	2.312
10	7	8	984	33.7393	1.312
20	14	8	3200	33.4083	0.3183
40	28	8	10672	33.3355	0.09969
80	56	8	38384	33.3023	

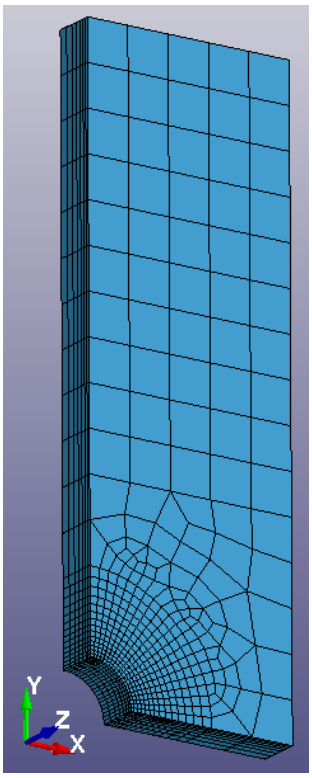

Figure 32 Finite element model of the notched specimen with coordinate axes and mesh shown.

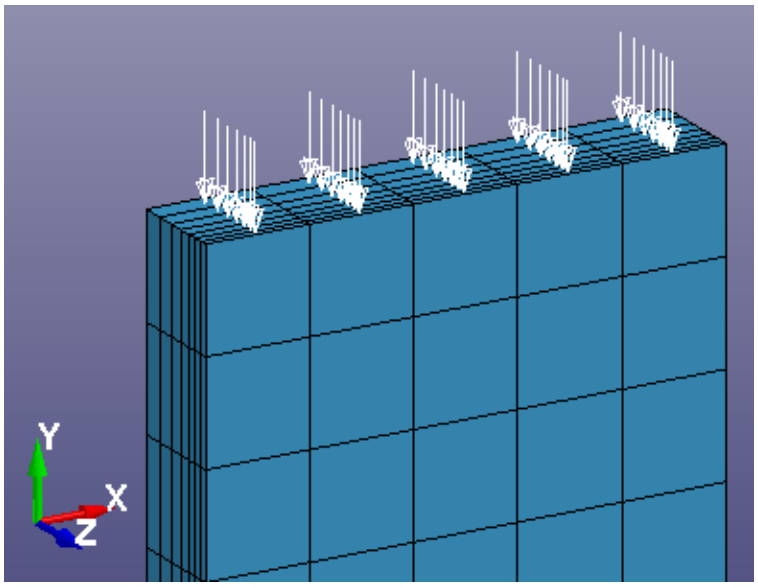

Figure 33 Load is applied as pressure to the top surface of the FE model.

4.3 Evaluation of residual stresses & strains around notch

After a notched member undergoes elastoplastic loading, a localized region at the notch has deformed plastically, so this region is expected to contain residual stresses and strains after

the load is removed. Therefore it is necessary to set the maximum load to both ensure that local yielding occurs at the notch and to prevent general yielding of the entire specimen. It was selected to be a load such that the net nominal stress (calculated at the net cross-section) equals to 80% of material yield strength in the corresponding loading mode. This is equivalent to gross nominal stress of 146 MPa for tension and 101 MPa for compression.

An experiment was performed on a notched AZ31B-H24 rolled sheet specimen. The specimen was quasi-statically loaded in tension up to 146 MPa and then unloaded. The same scenario was simulated in Abaqus using only tensile properties as input and LS-DYNA MAT_124 and MAT_233 with yield asymmetry.

All three FE simulations (Abaqus, MAT_124, and MAT_233) produced nearly identical surface strain distributions. At maximum load (Figure 34), the surface axial strain as measured by DIC and predicted by FEA are mostly consistent with each other across the entire notch region. However, Figure 35 shows that the measured residual surface axial strain after unloading has two residual strain hotspots at around 20° above and below the notch root and a low residual strain at notch root, whereas simulations predict a single hotspot at the notch root. This could possibly be due to material anisotropy which was not taken into account in the simulations.

A numerical comparison of the results is shown by Table 7. All three FE simulations slightly over-predicted strain at max load and greatly over-predicted residual strain. One reason for this could be due to the discrepancy between actual material behaviour and the hardening rules used by the material models. The isotropic hardening rule used by Abaqus and MAT_124 enlarges the yield surface without a change in shape or position in the stress space [11], resulting in a higher yield stress required to reverse yield. In magnesium alloys and particularly AZ31B-H24, the Bauschinger effect is expressed strongly at high plastic strain levels [118]; the yield surface shrinks and both the shape and position changes, resulting in much sooner reverse yielding and thus more strain reversal during unload. MAT_233 was setup such that distortional hardening was activated (MAGNESIUM option with both tensile and compressive input curves), which could explain the lower residual strain prediction than the other two models. MAT_233 seems to perform the best out of the three material models for predicting quasi-static loading in AZ31B-H24.

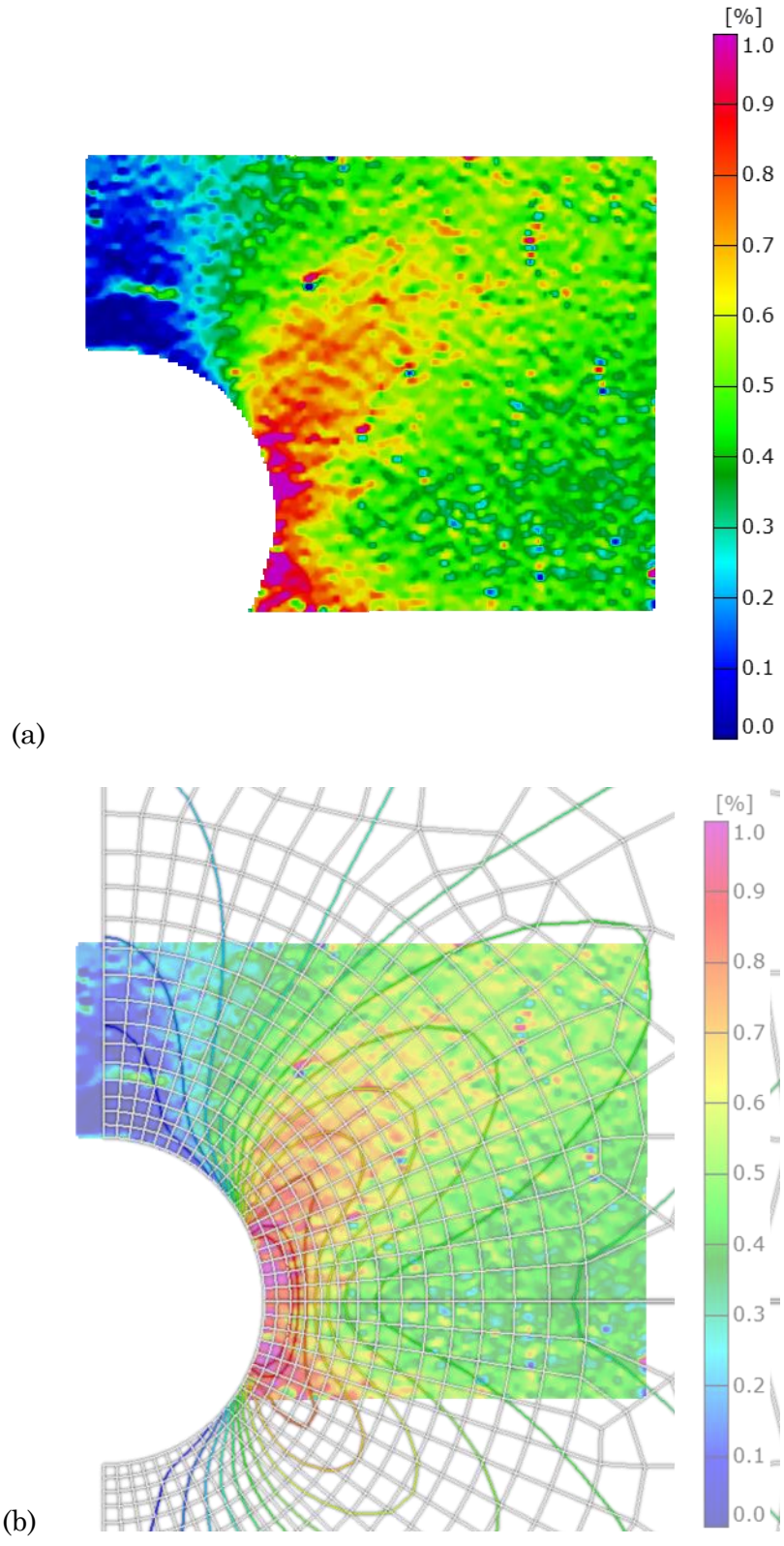

Figure 34 Surface axial strain at max tensile load (a) as measured by DIC, and (b) overlaid with surface axial strain isolines as predicted by Abaqus.

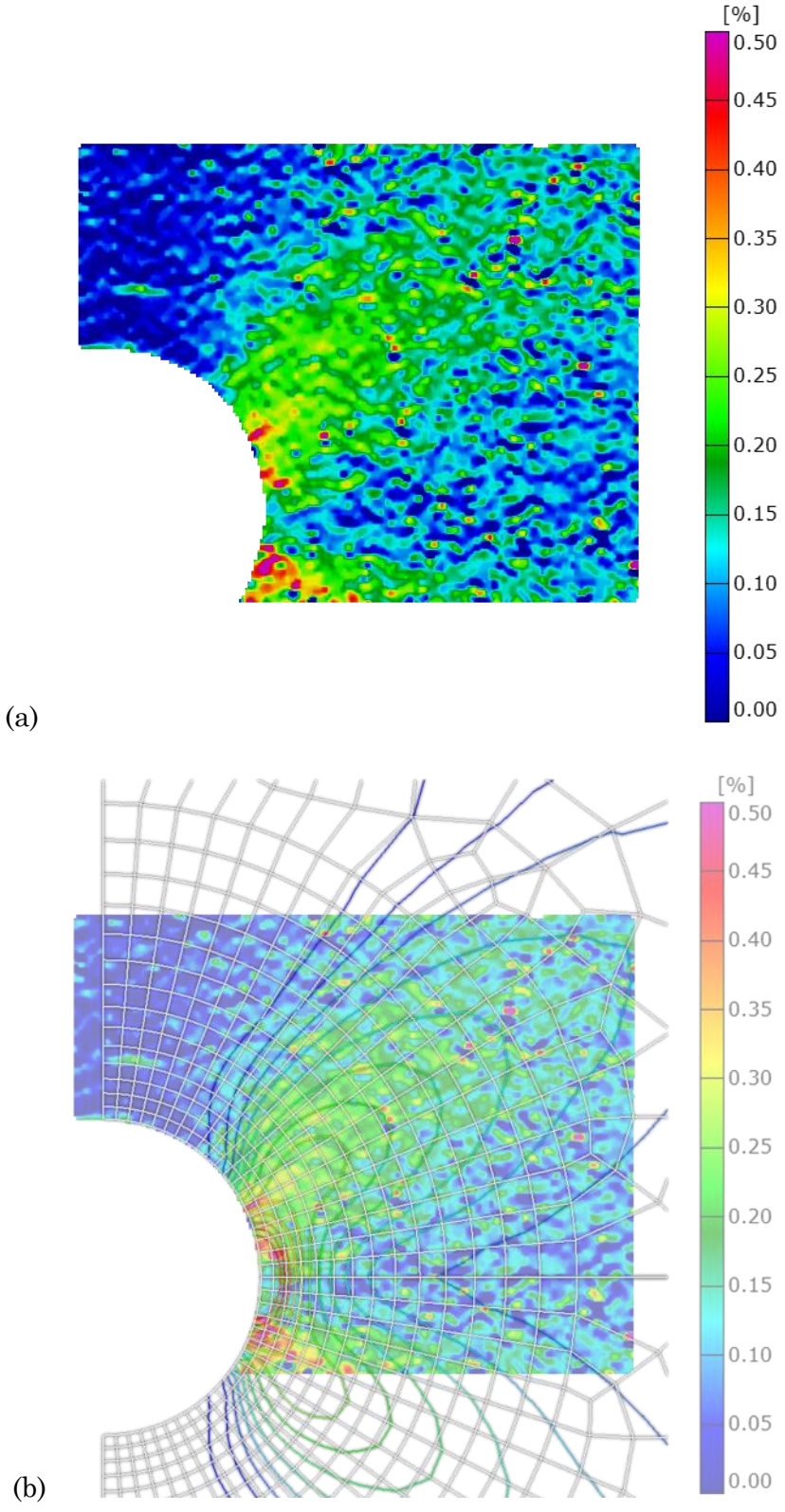

Figure 35 Residual surface axial strain after unload (a) as measured by DIC, and (b) overlaid with surface axial strain isolines predicted by FE simulation in Abaqus. The simulation results have been mirrored.

Table 7 Notch root axial strain measured by DIC and predicted using FE simulations. Prediction error is the difference between predicted and experimental values.

	DIC	Abaqus	MAT_124	MAT_233
At max load	0.01012	0.0158624	0.01480	0.01370
Prediction error		0.0057424	0.00468	0.00358
Residual	0.00147	0.00656251	0.00638	0.00494
Prediction error		0.00509251	0.00491	0.00347

4.4 Evaluation of cyclic stresses & strains at notch root

Experiments were performed on notched AZ31B-H24 rolled sheet specimens. Each specimen was subjected to constant amplitude fully-reversed nominal-load-controlled tests at multiple load levels. The gross nominal load, which was controlled, were selected based on an equivalent net nominal stress at a percentage of the compressive yield strength (CYS).

Axial strain at the notch root was measured using DIC and simulated via FEA with LS-DYNA MAT_233 using the cyclic stress-strain curves as input. MAT_233 was selected based on results from the residual stress & strain analysis, which found it to predict most closely to experimental results, out of the three material models examined. The simulation was performed by first initializing the FE model with zero initial stresses and strains and applying a compressive load, with the end state corresponding to the compressive tip of the stabilized hysteresis. Next the load was reversed to tensile loading. The final stress-strain state corresponded to the tensile tip of the stabilized hysteresis.

The predicted notch root axial strains are a good match with experimental measurements for the tested load cases which are from 50%-CYS to 70%-CYS (gross nominal stress of 63 MPa and 89 MPa, respectively) fully-reversed. The maximum prediction error was no more than 0.06% strain. Prediction errors for the tensile tip of the hysteresis were low, possibly due to over-prediction of change in strain in the tensile branches of the simulated stress-strain path, which resulted in a compensation of error in the initial compressive branch.

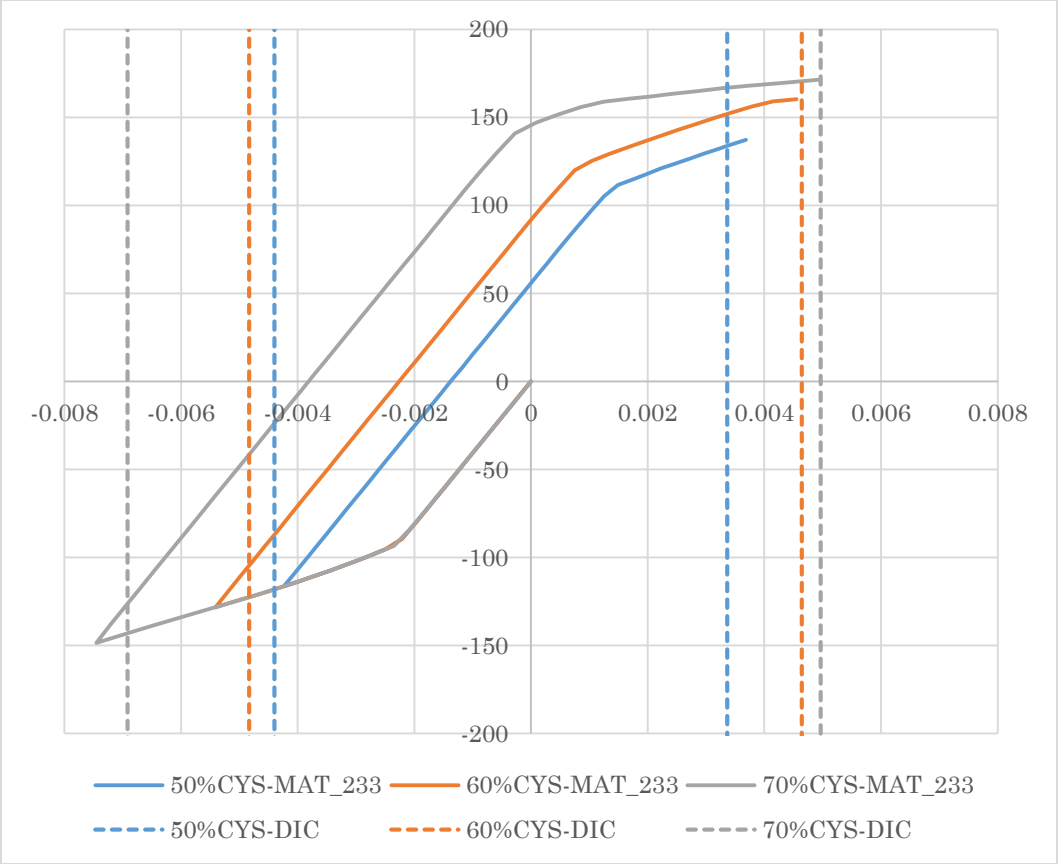

Figure 36 Experimental and predicted notch root axial strain under cyclic loading.

Table 8 Experimental and predicted notch root axial strain at cyclic stabilized hysteresis tips. The mean prediction error for the compressive tip is -0.0003160, and for tensile tip 0.00006865.

Load scenario	Hysteresis tip	DIC	MAT_233	Prediction error
50% CYS	Compressive	-0.00440	-0.004235	0.0001651
	Tensile	0.00337	0.003683	0.0003162
60% CYS	Compressive	-0.00483	-0.005411	-0.0005809
	Tensile	0.00464	0.004553	-0.00008675
70% CYS	Compressive	-0.00692	-0.007449	-0.0005321
	Tensile	0.00497	0.004943	-0.00002351

Chapter 5: Fatigue characterization and modelling

Two fatigue-life models were used in this project, the Smith-Watson-Topper (SWT) and Jahed-Varvani (JV) models. SWT is a popular model that is widely used, and JV is a newer energy-based model which is suitable for a wide variety of materials and loading conditions. Hasegawa et al. (2007) [116] found that Morrow's [129] and Lorenzo's [130] models were insufficient at predicting fatigue life of extruded AZ31, as they both tended to over-predict excessively the fatigue life as mean stress increased, while SWT showed promising results.

Fatigue model parameters were first obtained experimentally. Then, the fatigue models were applied to predict fatigue life of specimens under other loading scenarios. Finally, the predictions were compared with experimental results.

5.1 Characterization of fatigue parameters

The SWT and JV fatigue model parameters for AZ31B-H24 rolled sheet in rolling direction were obtained by fitting to experimental test data of fully-reversed strain-controlled CAL tests on smooth specimens. In calculating the plastic part of the Coffin-Manson parameters, only tests with plastic strain amplitude > 0.0002 were counted.

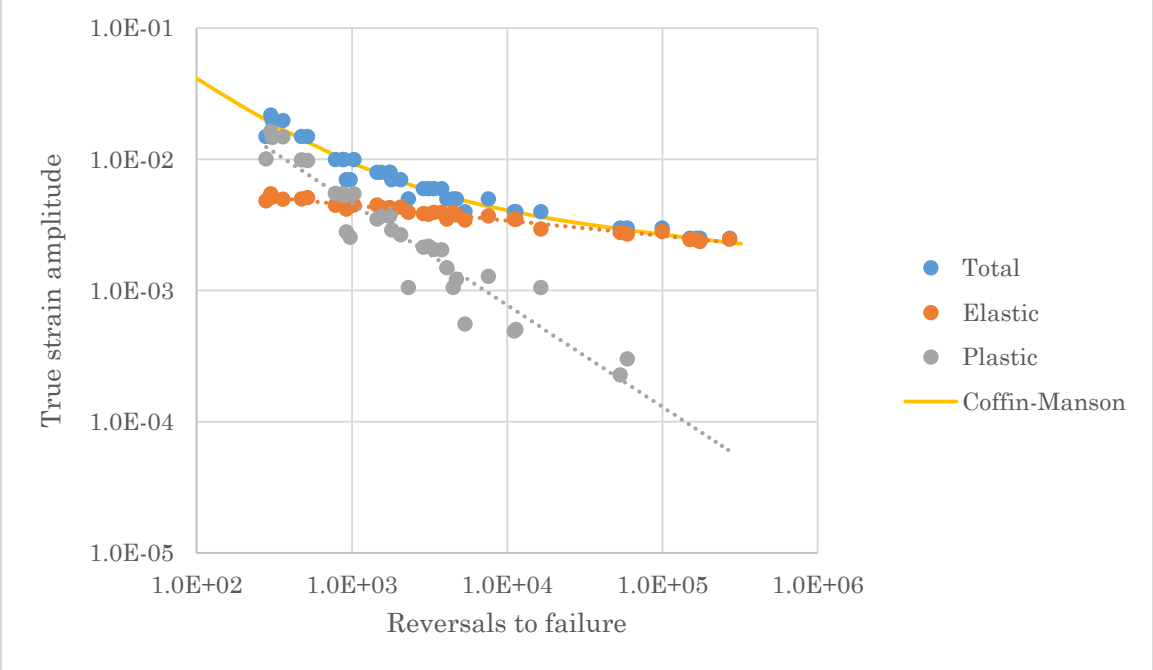

Figure 37 True strain amplitude vs reversals to failure decomposed into elastic and plastic components with Coffin-Manson curve fitted to experimental data.

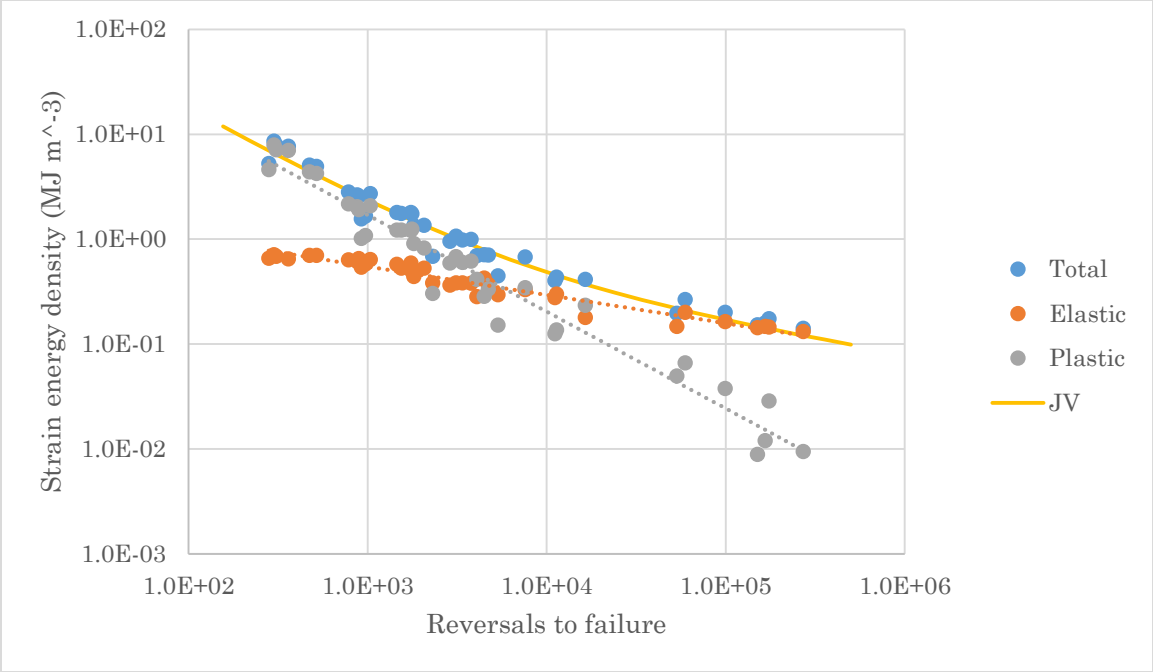

Figure 38 Strain energy density vs reversals to failure decomposed into elastic and plastic components with Jahed-Varvani curve fitted to experimental data.

Table 9 Experimentally obtained cyclic properties and Coffin-Manson and Jahed-Varvani model parameters.

Cyclic elastic modulus (GPa)	44.61
CM fatigue strength coefficient σ_f' (MPa)	460.771
CM fatigue strength exponent b	-0.121
CM fatigue ductility coefficient ϵ_f'	1.864
CM fatigue ductility exponent c	-0.859
JV fatigue strength coefficient E_e' (MJ m^{-3})	4.063
JV fatigue strength exponent B	-0.287
JV fatigue toughness coefficient E_f' (MJ m^{-3})	1419.112
JV fatigue toughness exponent C	-0.965

Rolled and extruded AZ31 series magnesium alloys seem to exhibit an endurance limit, possibly related to the existence of non-propagating cracks [131], [132]. For AZ31B-H24 rolled sheet, the fatigue endurance limit was estimated to be about 80 MPa, based on fitting

cyclic half-life hysteresis max stress vs cycles to failure of fully-reversed tests data (Figure 39) to a 4-point Weibull function as described by Chamos et al. (2008, 2010) [133], [134]:

$$\sigma_{\max} = P_1 + \frac{P_2 - P_1}{\exp\left(\left(\frac{\ln N_f}{P_3}\right)^{P_4}\right)}$$

P1 is the fatigue endurance limit, P2 is ultimate tensile strength, and P3 and P4 are regression analysis coefficients to be fitted. The numerical values of the coefficients are listed in Table 10. Data from both strain-controlled and stress-controlled tests were used, but limited to those with low plastic strain amplitude and negligible mean stress (no yield asymmetry).

The smooth transition from low to high cycle fatigue regions and high sensitivity to change in max stress in high cycle fatigue as shown by S-N data is in agreement with other magnesium alloys [135].

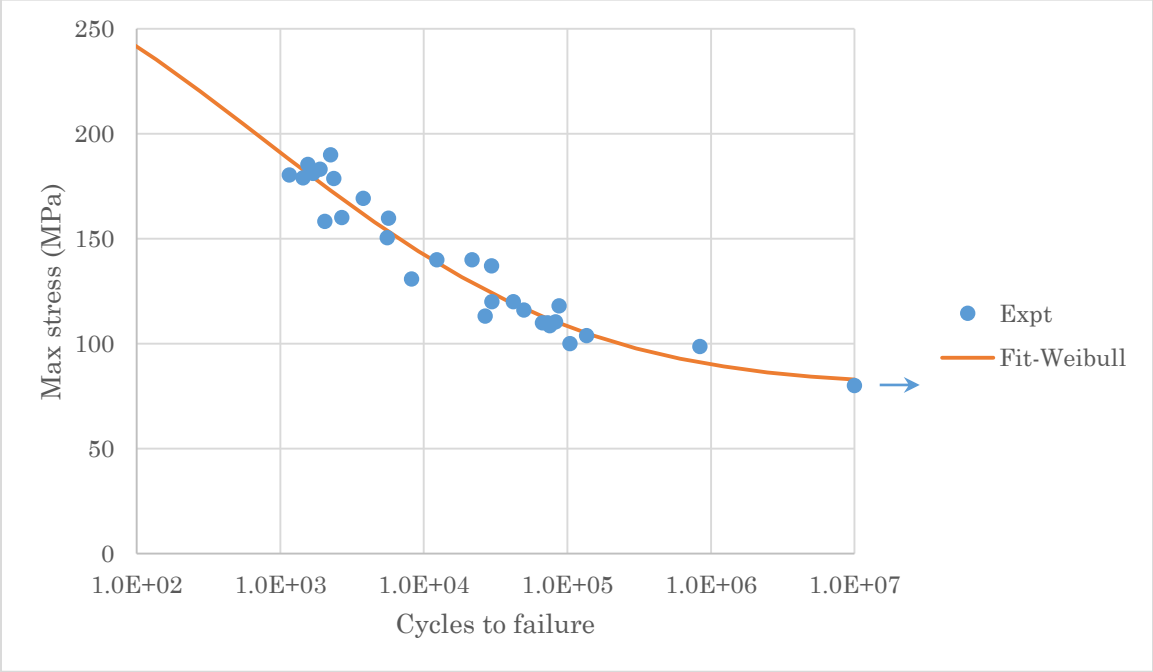

Figure 39 Max stress vs cycles to failure and fitted 4-point Weibull function for calculation of endurance limit.

Table 10 Weibull regression coefficients.

P_1 (MPa)	80.07
P_2 (MPa)	287
P_3	8.504
P_4	2.280

5.2 Proposed direct-fit models for SWT and JV

A new method of applying the SWT and JV fatigue models is proposed. For clarity, the original models are referred to as SWT or classic SWT and the proposed models are referred to as SWT-direct-fit or SWT-df, and similarly for JV.

Equations for SWT and JV are similar in form. They both have an elastic term and a plastic term derived from the respective parts of a material's cyclic stress-strain behaviour. In classic SWT, Coffin-Manson parameters are used which are derived from linear fits of logarithmic values of elastic and plastic strain amplitudes vs reversals to failure. In classic JV, the elastic part (positive elastic strain energy density) relates to the tensile peak of the hysteresis loop and the plastic part (plastic strain energy density) relate to the area enclosed by the hysteresis loop.

The proposed method fits a 4-term equation in the same form as the classic versions of these fatigue models directly to the model parameters vs logarithmic values of fatigue life.

SWT:

$$\sigma_{\max}\epsilon_a = \frac{\sigma_f'}{E}\left(2N_f\right)^b + \epsilon_f'\left(2N_f\right)^c$$

JV:

$$\Delta E = E_e'(2N_A)^B + E_f'(2N_A)^C$$

SWT-direct-fit:

$$\sigma_{\max}\epsilon_a = A_1\left(2N_f\right)^{b_1} + A_2\left(2N_f\right)^{b_2}$$

JV-direct-fit:

$$\Delta E = C_1\left(2N_f\right)^{d_1} + C_1\left(2N_f\right)^{d_2}$$

Whereas the classic models separate the elastic and plastic parts to compute model coefficients and then put back together, the direct-fit models compute all coefficients simultaneously through fitting. This provides an advantages in the reduced steps in computation as only the main model parameter must be computed. Additionally, this procedure can be applied to other fatigue models quite simply.

Figure 40 and Figure 41 show the difference in life prediction between the classic methods and the direct-fit method on the fully-reversed strain-controlled CAL tests on smooth AZ31B-H24 rolled sheet specimens. Table 11 and Table 12 compare the classic model and direct-fit parameters numerically. The direct-fit methods provide improved predictions, particularly at low- and high-ends of experimental data, on the fully-reversed strain-controlled tests on smooth specimens, as shown in Figure 41. A statistical analysis was performed on the model prediction error for this dataset, defined as the difference in logarithmic (base 10) life between model prediction and experimental fatigue life, the same criteria used by Ince and Glinka (2011) [136]:

$$\text{error} = \log_{10}\left(N_f^{\text{predicted}}\right) - \log_{10}\left(N_f^{\text{experimental}}\right)$$

A positive error indicates that the predictions are generally non-conservative (over-predicting) and a negative error indicates that the predictions are generally conservative (under-predicting). The mean and standard deviation are good indicators of central tendency and spread of the prediction errors [136] and they are listed in Table 13. All models are conservative, with the direct-fit versions of both SWT and JV being less conservative as well as significantly more centered. Additionally, the spread for direct-fit model predictions are equal, if not better, than the classic SWT and JV models. Between SWT, and JV, JV seems to be the better model, which agrees with findings by Park et al. (2010) [137] that energy-based fatigue-life models work well for rolled AZ31 Mg alloys.

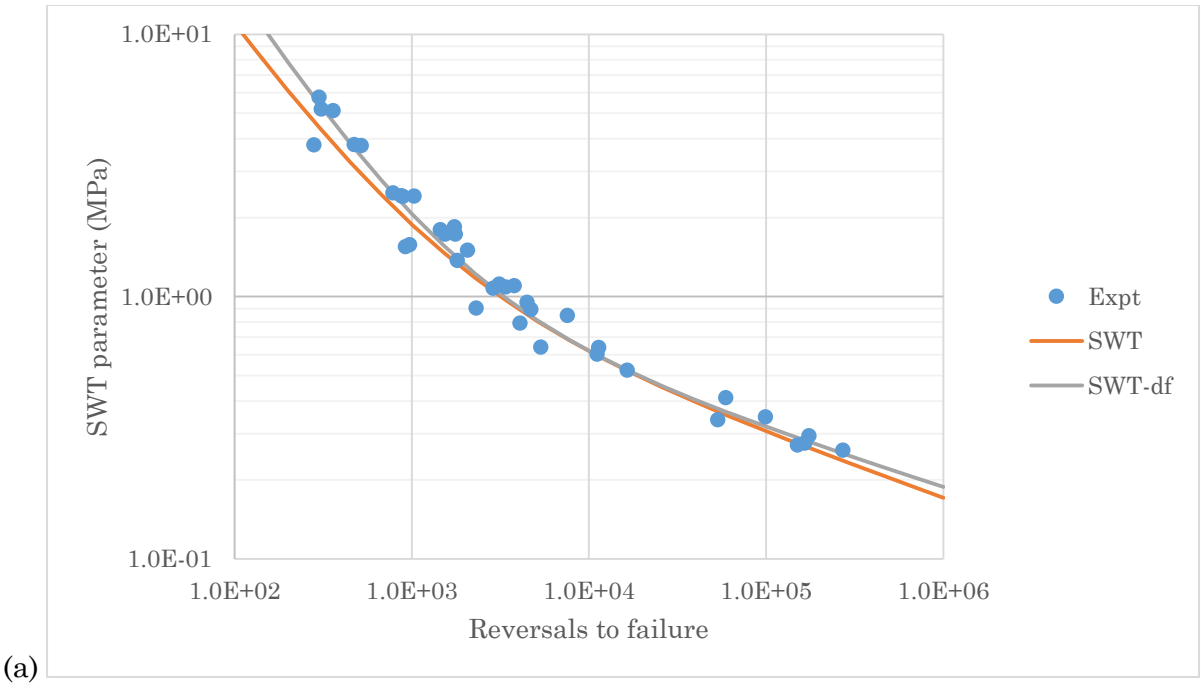

(a)

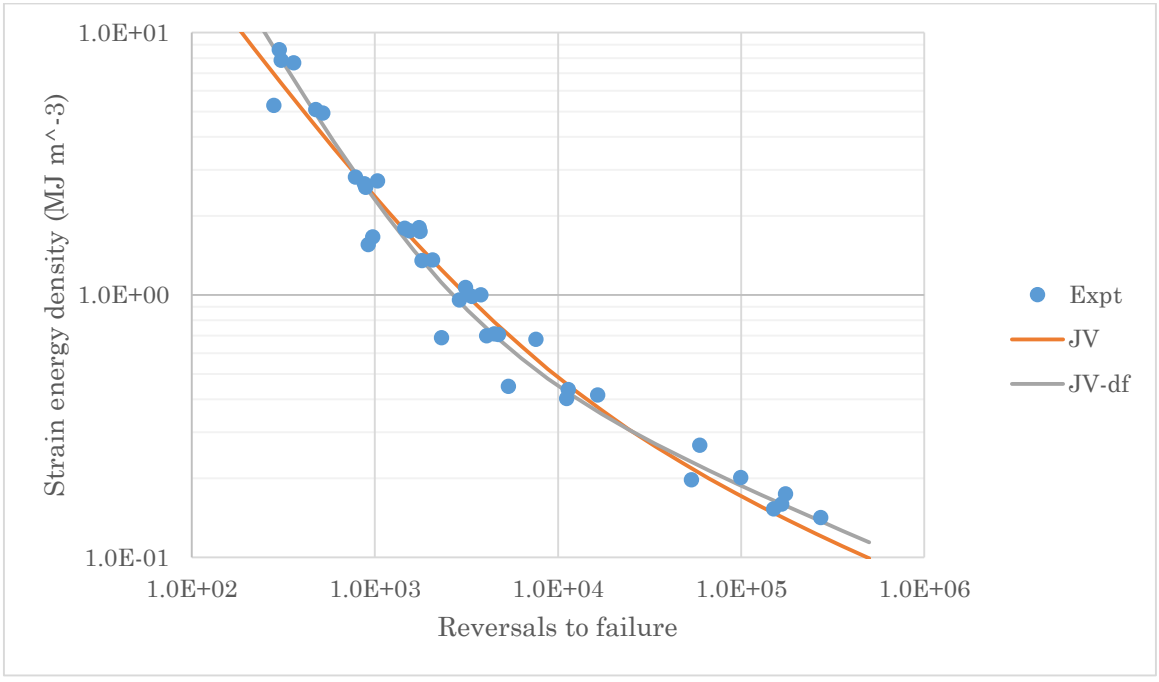

(b)

Figure 40 Comparing (a) SWT with SWT-df and (b) JV with JV-df predictions through fully-reversed strain-controlled CAL test data.

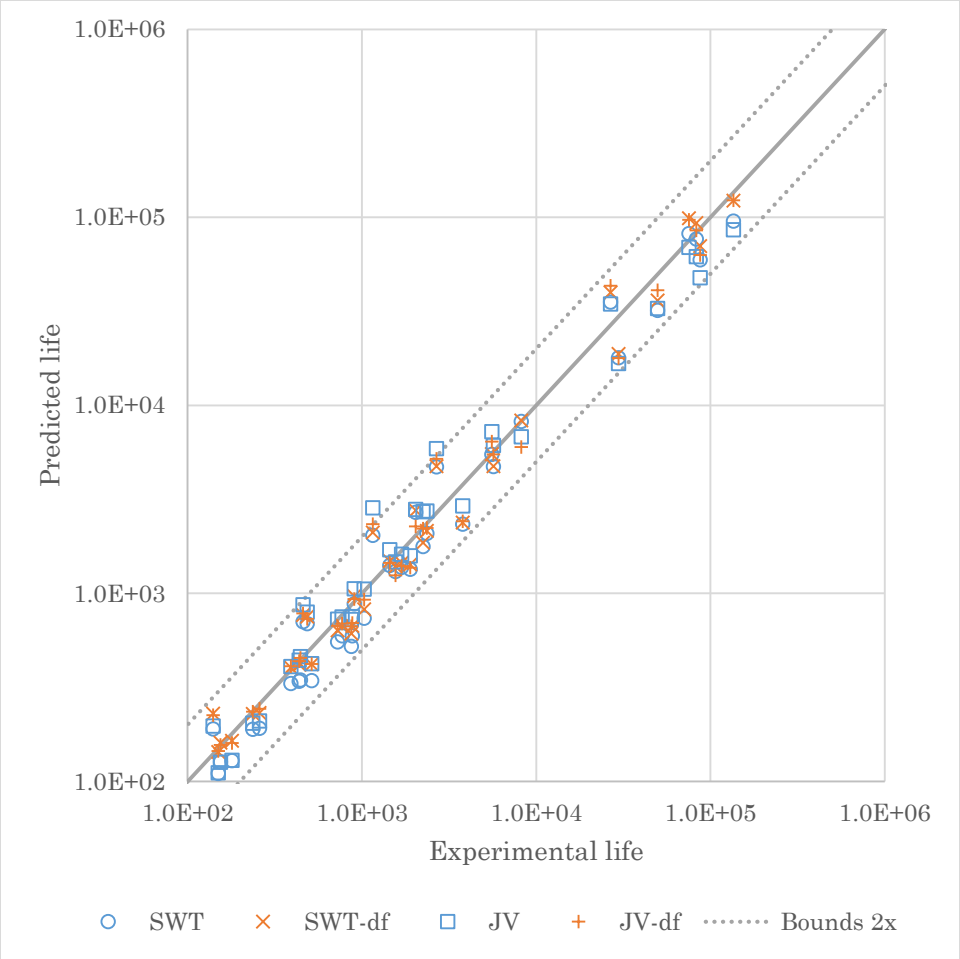

Figure 41 Predicted vs experimental fatigue life using SWT, SWT-df, JV, and JV-df for fully-reversed strain-controlled tests.

Table 11 Numerical comparison of corresponding coefficients between SWT and SWT-direct-fit for AZ31B-H24 rolled sheet.

	SWT	**SWT-direct-fit**
Elastic part	$(\sigma_f')^2/E = 4759.420$	$A_1 = 1742.959$
	$2b = -0.241$	$b_1 = -1.052$
Plastic part	$\sigma_f'\epsilon_f' = 858.794$	$A_2 = 3.846$
	$b + c = -0.980$	$b_2 = -0.219$

Table 12 Numerical comparison of corresponding coefficients between JV and JV-direct-fit for AZ31B-H24 rolled sheet.

	JV	**JV-direct-fit**
Elastic part	$E'_e = 4.063$	$C_1 = 5.523$
	$B = -0.287$	$d_1 = -0.296$
Plastic part	$E'_f = 1419.112$	$C_2 = 8778.477$
	$C = -0.965$	$d_2 = -1.248$

Table 13 Statistical analysis of model prediction errors of classic and direct-fit SWT & JV models on fully-reversed strain-controlled tests on smooth AZ31B-H24 rolled sheet specimens

	SWT	**SWT-df**	**JV**	**JV-df**
Mean	-0.05596	-0.004301	-0.0006314	-0.0001915
Standard deviation	0.1278	0.1206	0.1475	0.1250

5.3 Mean stress effect on fatigue life

For a given stress amplitude, the fatigue life of specimens which underwent stress-controlled tests with tensile mean stress were lower than those which underwent fully-reversed (zero mean stress) tests. For the stress amplitudes tested which were from 100 to 140 MPa, the fatigue life of the fully-reversed tests were 6 to 12 times higher than the mean stress R = 0 tests at the same stress amplitude, which demonstrates that tensile mean stresses are detrimental to fatigue life (Figure 42). At long lives, the mean stress effect can be expected to be less pronounced for a higher strength Mg alloy, or if the type of loading is not axial, such as bending [138], [139]. Our tests agree with recorded tests in literature at several difference stress ratios on axially loaded specimens which showed that increasing the stress ratio yielded decreased fatigue strength at both long and short lives for both smooth and notched specimens [138], [140]–[142].

The SWT and JV models with parameters obtained from fully-reversed strain-controlled tests were applied to predict fatigue life of the stress-controlled tests. The prediction results are compared with the experimental results in Figure 43 and Figure 44. Statistical analysis of the model predictions are shown in Table 14. Some observations on the results:

- SWT and SWT-direct-fit models seem to be better predictors of fatigue life than JV and JV-direct-fit in both the fully-reversed case and the tensile mean stress case.
- The classic SWT and JV models tend to be conservative while the direct-fit models tend to be non-conservative for the fully-reversed load case. However, all models tend to be conservative in the tensile mean stress case.
- The direct-fit models seem to produce slightly larger variance in results than the classic models, which is undesirable.

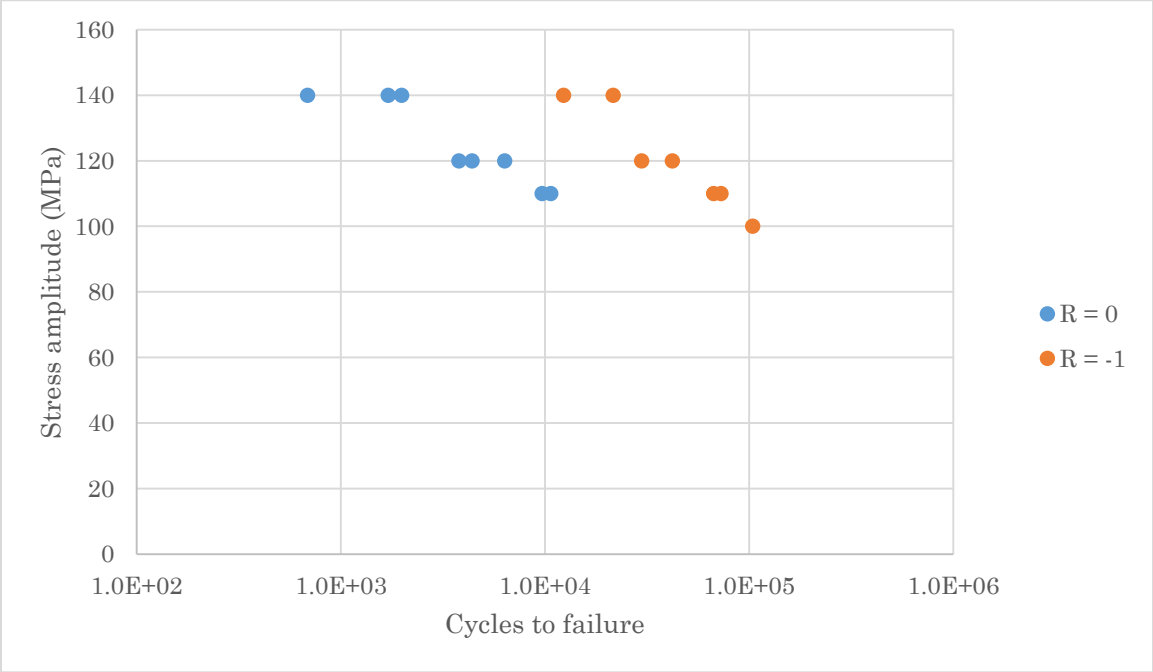

Figure 42 Stress amplitude vs cycles to failure for stress-controlled tests

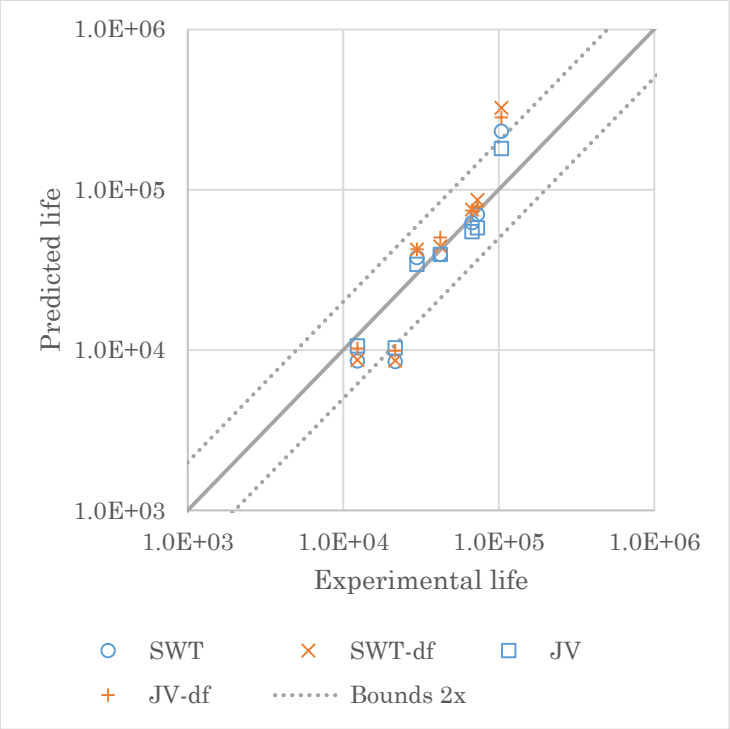

Figure 43 Predicted vs experimental fatigue life using SWT, SWT-df, JV, and JV-df for fully-reversed stress-controlled tests, R = -1.

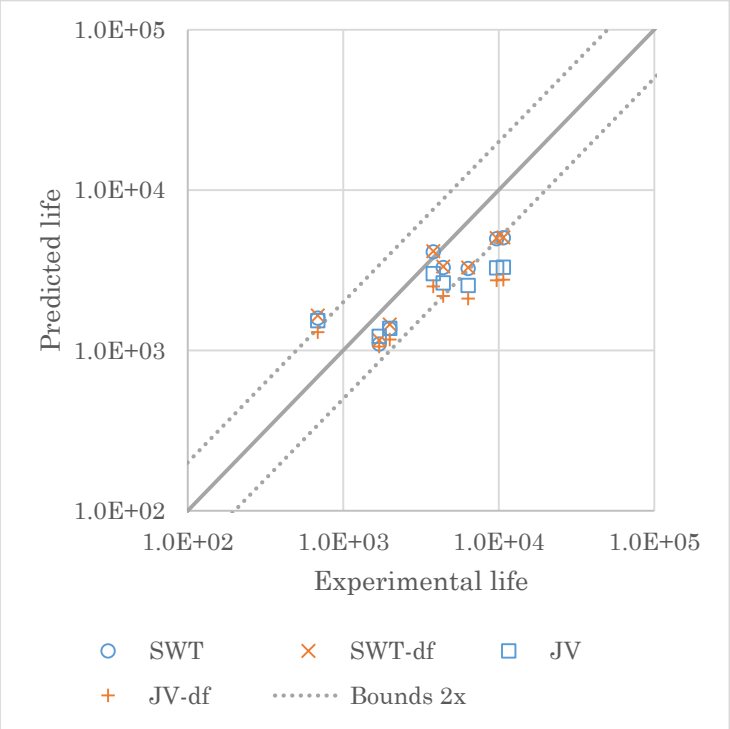

Figure 44 Predicted vs experimental fatigue life using SWT, SWT-df, JV, and JV-df for stress-controlled tests with mean stress, R = 0.

Table 14 Statistical analysis of model prediction errors of classic and direct-fit SWT & JV models on stress-controlled tests on smooth AZ31B-H24 rolled sheet specimens.

		SWT	SWT-df	JV	JV-df
R = -1	Mean	-0.02696	0.03403	-0.04320	0.04642
	Standard deviation	0.2306	0.2741	0.1699	0.2332
R = 0	Mean	-0.1232	-0.1126	-0.2070	-0.2825
	Standard deviation	0.2289	0.2312	0.2739	0.2768
All	Mean	-0.07830	-0.04418	-0.1305	-0.1290
	Standard deviation	0.2268	0.2543	0.2388	0.3008

5.4 Evaluation of Miner's rule

The Palmgren-Miner cumulative damage law [106] derives from empirical observations. It states that fatigue failure occurs due to accumulation of permanent damage induced by loading of the material, and that the fatigue life of a specimen that undergoes variable-amplitude loading can be predicted from the fatigue life of constant-amplitude loading tests corresponding to each hysteresis loop and the number of repetitions of each loop per VAL block.

We are interested in evaluating whether Miner's rule could be suitable for use with AZ31B-H24 rolled sheet under strain-controlled VAL for smooth and load-controlled VAL for notched specimens. Smooth specimens are covered in this section and notched specimens are covered in the next section, 5.5 Life prediction for notched specimens.

Variable-amplitude load strain-controlled tests were performed on smooth specimens. Comparisons of SWT and SWT-direct-fit models predictions with experimental tests are shown in Figure 45 with statistical analysis shown in Table 15. The following observations can be made:

- SWT seems to perform better than SWT-direct-fit, with a lower overall error.
- Both models predictions are non-conservative, with the direct-fit model predicting consistently higher life than classic SWT.

While prediction errors are higher than those of the fully-reversed strain-controlled tests, they are reasonably low such that most datapoints are within 2x (double-half) bounds. Thus we conclude that Miner's rule is applicable to AZ31B-H24 rolled sheet, which agrees with findings by Lin et al. (2013) [143] in which smooth AZ31B rolled sheet specimens were tested under stress-controlled loading. They used a stress-based fatigue-life model developed by Liu et al. (2010) [144] with several damage models including Miner's rule and found that Miner's rule worked well for predicting fatigue life.

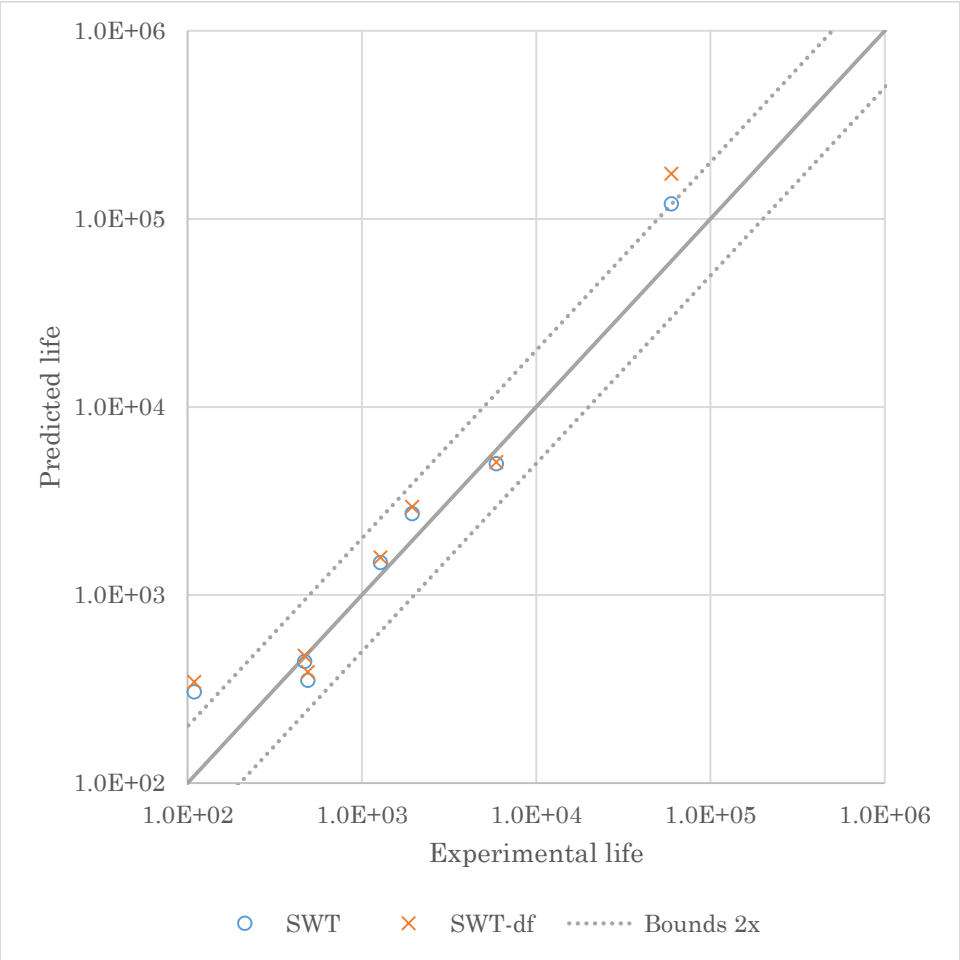

Figure 45 Predicted vs experimental fatigue life using SWT-df for strain-controlled VAL tests on smooth AZ31B-H24 rolled sheet specimens.

Table 15 Statistical analysis of model prediction errors of classic and direct-fit SWT models on VAL strain-controlled tests on smooth AZ31B-H24 rolled sheet specimens

	SWT	**SWT-df**
Mean	0.1021	0.1536
Standard deviation	0.2126	0.2437

5.5 Life prediction for notched specimens

Experiments were performed on notched AZ31B-H24 rolled sheet specimens, which consisted of fully-reversed constant-amplitude load tests and variable-amplitude load tests. Nominal load was controlled.

The dimensions of the specimen geometry do not satisfy clearly the conditions for either plane stress or plane strain, so calculations were done for both cases. Neuber and Glinka methods were selected for notch analysis. Dallmeier's phenomenological model [145] was used to generate stress-strain values of each reversal.

Additionally, another method of life prediction using FEA was to first obtain stress-strain values at hysteresis tips generated using LS-DYNA MAT_233, then to use with SWT and SWT-direct-fit models to predict fatigue life. This method uses neither plane stress nor plane strain, as the FE model was composed of multiple layers of solid elements in the through-thickness direction, allowing for accurate calculation of stresses and strains at the cost of computation time.

Figure 46 compares the predicted and experimental fatigue life from tests on notched specimens, and Table 16 shows the statistical analysis of predictions errors.

- All models predicted conservatively, under-predicting the fatigue life. This suggests that a different cumulative damage model may be more suitable than Miner's rule which is used here.
- The two best performing model combinations are: plane strain equations, Glinka's method for notch analysis, and SWT-direct-fit for fatigue-life estimation; FEA with MAT_233 and SWT-direct-fit.

- Glinka's method also consistently outperforms Neuber's method in both plane stress and plane strain, suggesting that notch fatigue may be strongly affected by strain energy density at the notch root.
- Model predictions for CAL tests are closer to experimental results across the board
- Life predictions using stress-strain values obtained through FEA are conservative and have the lowest error variance, making it an excellent method for engineering applications in which complex geometry is common.

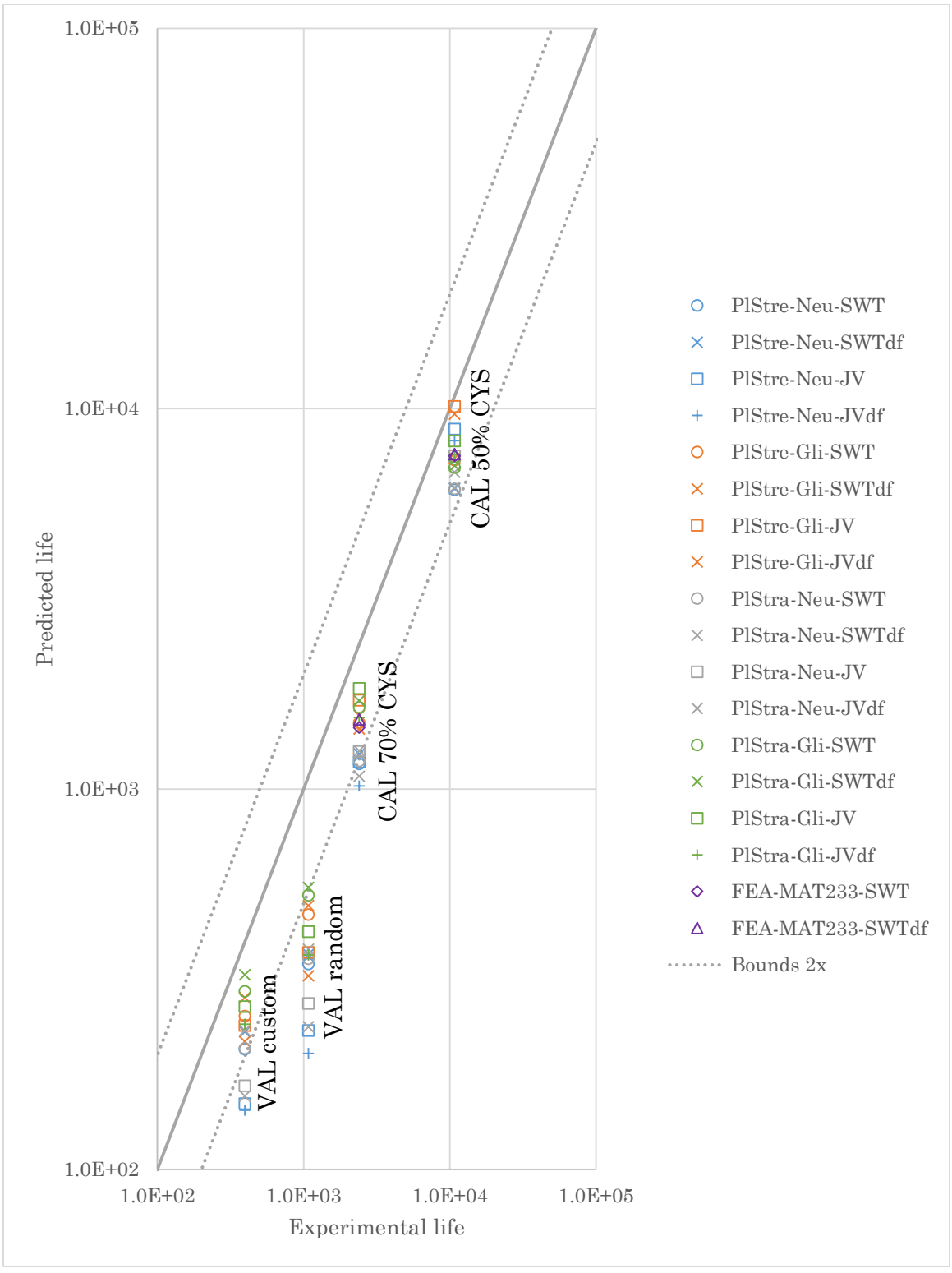

Figure 46 Predicted vs experimental fatigue life for constant- and variable-amplitude load tests on notched AZ31B-H24 rolled sheet specimens. Unit of life is in number of cycles for CAL tests and in number of blocks for VAL tests.

Table 16 Statistical analysis of prediction errors for tests on notched specimens.

			Mean	**Standard deviation**
Plane stress	Neuber	SWT	-0.3340	0.1095
		SWT-df	-0.3088	0.1083
		JV	-0.3722	0.2418
		JV-df	-0.4152	0.2509
	Glinka	SWT	-0.2332	0.08804
		SWT-df	-0.2092	0.08864
		JV	-0.2142	0.1836
		JV-df	-0.2638	0.1969
Plane strain	Neuber	SWT	-0.3273	0.1046
		SWT-df	-0.3019	0.1040
		JV	-0.3535	0.1858
		JV-df	-0.4026	0.1911
	Glinka	SWT	-0.1990	0.07992
		SWT-df	-0.1775	0.08652
		JV	-0.2028	0.1391
		JV-df	-0.2581	0.1435
FEA	MAT_233	SWT	-0.1883	0.04276
		SWT-df	-0.1753	0.03135

Chapter 6: Conclusions & future work

6.1 Conclusions

In this project, 6.2 mm thick AZ31B-H24 rolled sheet was studied. Its monotonic and cyclic properties were characterized and then used to fit various model coefficients. The material was then simulated and tested in new load cases and the results were analyzed. The following conclusions can be drawn:

- Tensile-compressive yield asymmetry in AZ31B-H24 rolled sheet is more significant compared to anisotropy.
- The yield asymmetry begins to occur at strain amplitudes of about 0.7% in the rolling direction; the material behaves symmetrically at and below that level.
- Under fully-reversed strain-controlled loading, cyclic hardening occurs at about 0.8% strain amplitude and cyclic softening occurs at about 0.4% strain amplitude.
- Under stress-controlled with tensile mean stress (R=0) tests, ratcheting causes tensile strain to develop over time until sudden fracture of the specimen.
- LS-DYNA MAT_233 is a good choice of material model to use for predicting residual stress and strain due to quasi-static loading up to 1% strain at notch root and cyclic stresses and strains up to 0.7% strain at notch root, outperforming MAT_124 and Abaqus with the built-in material models (without UMAT).
- SWT and JV are both suitable fatigue-life models for AZ31B-H24 for strain-controlled tests. The proposed direct-fit models improves predictions over classic SWT and JV models for strain-controlled tests.
- Overall, SWT and SWT-direct-fit are suitable for all tested load cases, which include strain- and stress-controlled, CAL and VAL tests on smooth specimens and load-controlled CAL and VAL tests on notched specimens, outperforming JV and JV-direct-fit in most cases.
- Miner's rule is a useful cumulative damage law for AZ31B-H24 in that it predicts well for smooth specimens and tends to be conservative for notched specimens.
- Glinka's method outperforms Neuber's rule and FEA with MAT_233 for notch analysis and fatigue life estimation of AZ31B-H24 notched specimens.

6.2 Recommended future work

The following topics are recommended for future work:

- Implement anisotropy, in addition to material yield asymmetry, into a numerical material model such as LS-DYNA MAT_233 for use in finite element simulations.
- Fatigue behaviour of magnesium alloys under multiaxial loading. This project focused on fatigue under axial loading, which can be built upon for multiaxial cases.
- Include considerations for strain rate effects and material failure, which would be useful for applications such as vehicle passenger safety and crashworthiness and pave the way for magnesium alloys to be used as structural members.

References

[1] N. Stern, "Stern Review: The Economics of Climate Change," Cambridge University Press, 2007.

[2] J. T. Houghton *et al.*, *Climate Change 2001: The Scientific Basis*. Cambridge University Press, 2001.

[3] D. L. Greene, "Reducing Greenhouse Gas Emissions From Transportation," presented at the Legislative Commission on Global Climate Change, 2006.

[4] "CO2 Emissions from Fuel Combustion 2017," International Energy Agency, 2017.

[5] US Department of Transportation, "Corporate Average Fuel Economy (CAFE) Standards," 11-Aug-2014. [Online]. Available: https://www.transportation.gov/mission/sustainability/corporate-average-fuel-economy-cafe-standards.

[6] W. J. Joost, "Reducing Vehicle Weight and Improving U.S. Energy Efficiency Using Integrated Computational Materials Engineering," *JOM*, vol. 64, no. 9, pp. 1032–1038, Sep. 2012.

[7] M. K. Kulekci, "Magnesium and its alloys applications in automotive industry," *Int. J. Adv. Manuf. Technol.*, vol. 39, no. 9–10, pp. 851–865, Nov. 2008.

[8] G. Davies, *Materials for automobile bodies*, 2nd ed. Amsterdam: Elsevier/Butterworth-Heinemann, 2012.

[9] H. Friedrich and S. Schumann, "Research for a 'new age of magnesium' in the automotive industry," *J. Mater. Process. Technol.*, vol. 117, no. 3, pp. 276–281, Nov. 2001.

[10] J. S. Balzer *et al.*, "Structural Magnesium Front End Support Assembly," presented at the SAE 2003 World Congress & Exhibition, 2003.

[11] R. I. Stephens, A. Fatemi, R. R. Stephens, and H. O. Fuchs, *Metal Fatigue in Engineering*. John Wiley & Sons, Inc., 1980.

[12] J. A. Bannantine, J. J. Comer, and J. L. Handrock, *Fundamentals of metal fatigue analysis*, 1st ed. Prentice Hall, 1989.

[13] C. H. Cáceres and A. H. Blake, "On the strain hardening behaviour of magnesium at room temperature," *Mater. Sci. Eng. A*, vol. 462, no. 1–2, pp. 193–196, Jul. 2007.

[14] Z. Basinski, "The Influence of Temperature and Strain Rate on the Flow Stress of Magnesium Single Crystals," *Aust. J. Phys.*, vol. 13, no. 2, pp. 284–298, Jun. 1960.

[15] F. F. Lavrentev and Y. A. Pokhil, "Relation of dislocation density in different slip systems to work hardening parameters for magnesium crystals," *Mater. Sci. Eng.*, vol. 18, no. 2, pp. 261–270, Apr. 1975.

[16] F. F. Lavrentev, "The type of dislocation interaction as the factor determining work hardening," *Mater. Sci. Eng.*, vol. 46, no. 2, pp. 191–208, Dec. 1980.

[17] P. Lukáč and Z. Trojanová, "Hardening and softening in selected magnesium alloys," *Mater. Sci. Eng. A*, vol. 462, no. 1–2, pp. 23–28, Jul. 2007.

[18] G. B. Bülfinger, *Comment. Acad. Sci. Imp. Petropolitanae*, 1735.

[19] J. H. Hollomon, *Trans. Metall. Soc. AIME*, 1945.

[20] W. Ramberg and W. R. Osgood, "Description of stress-strain curves by three parameters." 1943.

[21] "ASTM E527-16 Standard Practice for Numbering Metals and Alloys in the Unified Numbering System (UNS)." ASTM International, 2016.

[22] "ASTM B107/B107M-13 Standard Specification for Magnesium-Alloy Extruded Bars, Rods, Profiles, Tubes, and Wire." ASTM International, 2013.

[23] "ASTM B296-03(2014) Standard Practice for Temper Designations of Magnesium Alloys, Cast and Wrought." ASTM International, 2014.
[24] M. Gupta and N. M. L. Sharon, *Magnesium, Magnesium Alloys, and Magnesium Composites*. Hoboken, NJ, USA: John Wiley & Sons, Inc., 2010.
[25] M. M. Avedesian and H. Baker, *ASM specialty handbook: magnesium and magnesium alloys*. ASM International, 1999.
[26] J. Casey and H. Jahedmotlagh, "The strength-differential effect in plasticity," *Int. J. Solids Struct.*, vol. 20, no. 4, pp. 377–393, 1984.
[27] E. A. Ball and P. B. Prangnell, "Tensile-compressive yield asymmetries in high strength wrought magnesium alloys," *Scr. Metall. Mater.*, vol. 31, no. 2, pp. 111–116, Mar. 1994.
[28] C. S. Roberts, *Magnesium and its alloys*. Wiley, 1960.
[29] A. A. Roostaei and H. Jahed, "Role of loading direction on cyclic behaviour characteristics of AM30 extrusion and its fatigue damage modelling," *Mater. Sci. Eng. A*, vol. 670, pp. 26–40, Jul. 2016.
[30] A. Gryguc *et al.*, "Monotonic and cyclic behaviour of cast and cast-forged AZ80 Mg," *Int. J. Fatigue*, vol. 104, pp. 136–149, Nov. 2017.
[31] A. A. Roostaei and H. Jahed, "Multiaxial cyclic behaviour and fatigue modelling of AM30Mg alloy extrusion," *Int. J. Fatigue*, vol. 97, pp. 150–161, Apr. 2017.
[32] A. Gryguc *et al.*, "Low-cycle fatigue characterization and texture induced ratcheting behaviour of forged AZ80 Mg alloys," *Int. J. Fatigue*, vol. 116, pp. 429–438, Nov. 2018.
[33] S. M. H. Karparvarfard, S. K. Shaha, S. B. Behravesh, H. Jahed, and B. W. Williams, "Microstructure, texture and mechanical behavior characterization of hot forged cast ZK60 magnesium alloy," *J. Mater. Sci. Technol.*, vol. 33, no. 9, pp. 907–918, Sep. 2017.
[34] R. Jahadi, M. Sedighi, and H. Jahed, "ECAP effect on the micro-structure and mechanical properties of AM30 magnesium alloy," *Mater. Sci. Eng. A*, vol. 593, pp. 178–184, Jan. 2014.
[35] G. Shayegan *et al.*, "Residual stress induced by cold spray coating of magnesium AZ31B extrusion," *Mater. Des.*, vol. 60, pp. 72–84, Aug. 2014.
[36] E. Kalatehmollaei, H. Mahmoudi-Asl, and H. Jahed, "An asymmetric elastic–plastic analysis of the load-controlled rotating bending test and its application in the fatigue life estimation of wrought magnesium AZ31B," *Int. J. Fatigue*, vol. 64, pp. 33–41, Jul. 2014.
[37] M. Diab, X. Pang, and H. Jahed, "The effect of pure aluminum cold spray coating on corrosion and corrosion fatigue of magnesium (3% Al-1% Zn) extrusion," *Surf. Coat. Technol.*, vol. 309, pp. 423–435, Jan. 2017.
[38] A. Hadadzadeh, M. A. Wells, S. K. Shaha, H. Jahed, and B. W. Williams, "Role of compression direction on recrystallization behavior and texture evolution during hot deformation of extruded ZK60 magnesium alloy," *J. Alloys Compd.*, vol. 702, pp. 274–289, Apr. 2017.
[39] A. Gryguc, S. K. Shaha, H. Jahed, M. Wells, B. Williams, and J. McKinley, "Tensile and fatigue behaviour of as-forged AZ31B extrusion," *Frat. Ed Integrità Strutt.*, no. 38, Oct. 2016.
[40] S. M. H. Karparvarfard, S. K. Shaha, S. B. Behravesh, H. Jahed, and B. W. Williams, "Fatigue characteristics and modeling of cast and cast-forged ZK60 magnesium alloy," *Int. J. Fatigue*, Mar. 2018.

[41] S. B. Dayani, S. K. Shaha, R. Ghelichi, J. F. Wang, and H. Jahed, "The impact of AA7075 cold spray coating on the fatigue life of AZ31B cast alloy," *Surf. Coat. Technol.*, vol. 337, pp. 150–158, Mar. 2018.
[42] H. Jahed and J. Albinmousa, "Multiaxial behaviour of wrought magnesium alloys – A review and suitability of energy-based fatigue life model," *Theor. Appl. Fract. Mech.*, vol. 73, pp. 97–108, Oct. 2014.
[43] J. Albinmousa, H. Jahed, and S. Lambert, "Cyclic behaviour of wrought magnesium alloy under multiaxial load," *Int. J. Fatigue*, vol. 33, no. 8, pp. 1127–1139, Aug. 2011.
[44] J. Albinmousa, H. Jahed, and S. Lambert, "Cyclic axial and cyclic torsional behaviour of extruded AZ31B magnesium alloy," *Int. J. Fatigue*, vol. 33, no. 11, pp. 1403–1416, Nov. 2011.
[45] J. Albinmousa and H. Jahed, "Multiaxial effects on LCF behaviour and fatigue failure of AZ31B magnesium extrusion," *Int. J. Fatigue*, vol. 67, pp. 103–116, Oct. 2014.
[46] L. Wu *et al.*, "The effects of texture and extension twinning on the low-cycle fatigue behavior of a rolled magnesium alloy, AZ31B," *Mater. Sci. Eng. A*, vol. 527, no. 26, pp. 7057–7067, Oct. 2010.
[47] S. B. Behravesh, "Fatigue Characterization and Cyclic Plasticity Modeling of Magnesium Spot-Welds," PhD thesis, University of Waterloo, 2013.
[48] S. B. Behravesh, H. Jahed, and S. Lambert, "Characterization of magnesium spot welds under tensile and cyclic loadings," *Mater. Des.*, vol. 32, no. 10, pp. 4890–4900, Dec. 2011.
[49] S. B. Behravesh, H. Jahed, and S. Lambert, "Fatigue characterization and modeling of AZ31B magnesium alloy spot-welds," *Int. J. Fatigue*, vol. 64, pp. 1–13, Jul. 2014.
[50] M. Sun, S. B. Behravesh, L. Wu, Y. Zhou, and H. Jahed, "Fatigue behaviour of dissimilar Al 5052 and Mg AZ31 resistance spot welds with Sn-coated steel interlayer: Fatigue Behaviour of Dissimilar Al 5052 and Mg AZ31 Resistance Spot Welds," *Fatigue Fract. Eng. Mater. Struct.*, vol. 40, no. 7, pp. 1048–1058, Jul. 2017.
[51] B. Behravesh, L. Liu, H. Jahed, S. Lambert, G. Glinka, and N. Zhou, "Effect of Nugget Size on Tensile and Fatigue Strength of Spot Welded AZ31 Magnesium Alloy," presented at the SAE 2010 World Congress & Exhibition, 2010.
[52] S. B. Behravesh, H. Jahed, S. B. Lambert, and M. Chengji, "Constitutive Modeling for Cyclic Behavior of AZ31B Magnesium Alloy and its Application," *Adv. Mater. Res.*, vol. 891–892, pp. 809–814, Mar. 2014.
[53] D. Toscano, S. K. Shaha, B. Behravesh, H. Jahed, and B. Williams, "Effect of forging on the low cycle fatigue behavior of cast AZ31B alloy," *Mater. Sci. Eng. A*, vol. 706, pp. 342–356, Oct. 2017.
[54] D. Toscano, S. K. Shaha, B. Behravesh, H. Jahed, and B. Williams, "Effect of Forging on Microstructure, Texture, and Uniaxial Properties of Cast AZ31B Alloy," *J. Mater. Eng. Perform.*, vol. 26, no. 7, pp. 3090–3103, Jul. 2017.
[55] D. Toscano, S. K. Shaha, B. Behravesh, H. Jahed, B. Williams, and X. Su, "Influence of Low Temperature Forging on Microstructure and Low Cycle Fatigue Behavior of Cast AZ31B Mg Alloy," in *Magnesium Technology 2018*, 2018, pp. 267–273.
[56] D. Toscano *et al.*, "Effect of Forging on Microstructure, Texture and Compression Behavior of Extruded AZ31B," in *Proceedings of the 3rd Pan American Materials Congress*, 2017, pp. 347–354.
[57] A. Gryguc, H. Jahed, B. Williams, and J. McKinley, "MagForge – Mechanical Behaviour of Forged AZ31B Extruded Magnesium in Monotonic Compression," *Mater. Sci. Forum*, vol. 828–829, pp. 291–297, Aug. 2015.

[58] M. Noban, J. Albinmousa, H. Jahed, and S. Lambert, “A Continuum-Based Cyclic Plasticity Model for AZ31B Magnesium Alloy under Proportional loading,” *Procedia Eng.*, vol. 10, pp. 1366–1371, 2011.
[59] A. A. Roostaei and H. Jahed, “A cyclic small-strain plasticity model for wrought Mg alloys under multiaxial loading: Numerical implementation and validation,” *Int. J. Mech. Sci.*, vol. 145, pp. 318–329, Sep. 2018.
[60] P. J. Armstrong and C. O. Frederick, “A Mathematical Representation of the Multiaxial Bauschinger Effect,” p. 24, 1966.
[61] R. T. Shield and H. Ziegler, “On Prager’s hardening rule,” *ZAMP Z. Für Angew. Math. Phys.*, vol. 9, no. 3, pp. 260–276, Sep. 1958.
[62] H. Ziegler, “A modification of Prager’s hardening rule,” *Q. Appl. Math.*, vol. 17, no. 1, pp. 55–65, Apr. 1959.
[63] B. Kondori, Y. Madi, J. Besson, and A. A. Benzerga, “Evolution of the 3D plastic anisotropy of HCP metals: Experiments and modeling,” *Int. J. Plast.*, Feb. 2018.
[64] B. M. Darras, M. K. Khraisheh, F. K. Abu-Farha, and M. A. Omar, “Friction stir processing of commercial AZ31 magnesium alloy,” *J. Mater. Process. Technol.*, vol. 191, no. 1–3, pp. 77–81, Aug. 2007.
[65] W. B. Lee, Y. M. Yeon, and S. B. Jung, “Joint properties of friction stir welded AZ31B– H24 magnesium alloy,” *Mater. Sci. Technol.*, vol. 19, no. 6, pp. 785–790, Jun. 2003.
[66] M. Pareek, A. Polar, F. Rumiche, and J. E. Indacochea, “Metallurgical Evaluation of AZ31B-H24 Magnesium Alloy Friction Stir Welds,” *J. Mater. Eng. Perform.*, vol. 16, no. 5, pp. 655–662, Sep. 2007.
[67] N. Afrin, D. L. Chen, X. Cao, and M. Jahazi, “Microstructure and tensile properties of friction stir welded AZ31B magnesium alloy,” *Mater. Sci. Eng. A*, vol. 472, no. 1–2, pp. 179–186, Jan. 2008.
[68] X. Cao and M. Jahazi, “Effect of welding speed on the quality of friction stir welded butt joints of a magnesium alloy,” *Mater. Des.*, vol. 30, no. 6, pp. 2033–2042, Jun. 2009.
[69] S. M. Chowdhury, D. L. Chen, S. D. Bhole, and X. Cao, “Effect of pin tool thread orientation on fatigue strength of friction stir welded AZ31B-H24 Mg butt joints,” *Procedia Eng.*, vol. 2, no. 1, pp. 825–833, Apr. 2010.
[70] B. S. Naik, D. L. Chen, X. Cao, and P. Wanjara, “Microstructure and Fatigue Properties of a Friction Stir Lap Welded Magnesium Alloy,” *Metall. Mater. Trans. A*, vol. 44, no. 8, pp. 3732–3746, Aug. 2013.
[71] G. Padmanaban and V. Balasubramanian, “An experimental investigation on friction stir welding of AZ31B magnesium alloy,” *Int. J. Adv. Manuf. Technol.*, vol. 49, no. 1–4, pp. 111–121, Jul. 2010.
[72] A. . Somasekharan and L. . Murr, “Microstructures in friction-stir welded dissimilar magnesium alloys and magnesium alloys to 6061-T6 aluminum alloy,” *Mater. Charact.*, vol. 52, no. 1, pp. 49–64, Mar. 2004.
[73] S. H. Chowdhury, D. L. Chen, S. D. Bhole, X. Cao, and P. Wanjara, “Lap shear strength and fatigue life of friction stir spot welded AZ31 magnesium and 5754 aluminum alloys,” *Mater. Sci. Eng. A*, vol. 556, pp. 500–509, Oct. 2012.
[74] S. H. Chowdhury, D. L. Chen, S. D. Bhole, X. Cao, and P. Wanjara, “Lap shear strength and fatigue behavior of friction stir spot welded dissimilar magnesium-to-aluminum joints with adhesive,” *Mater. Sci. Eng. A*, vol. 562, pp. 53–60, Feb. 2013.
[75] F. Khodabakhshi, B. Marzbanrad, L. H. Shah, H. Jahed, and A. P. Gerlich, “Friction-stir processing of a cold sprayed AA7075 coating layer on the AZ31B substrate:

Structural homogeneity, microstructures and hardness," *Surf. Coat. Technol.*, vol. 331, pp. 116–128, Dec. 2017.
[76] B. Marzbanrad, H. Jahed, and E. Toyserkani, "On the evolution of substrate's residual stress during cold spray process: A parametric study," *Mater. Des.*, vol. 138, pp. 90–102, Jan. 2018.
[77] G. Padmanaban and V. Balasubramanian, "Fatigue performance of pulsed current gas tungsten arc, friction stir and laser beam welded AZ31B magnesium alloy joints," *Mater. Des.*, vol. 31, no. 8, pp. 3724–3732, Sep. 2010.
[78] W. Wu, S. Y. Lee, A. M. Paradowska, Y. Gao, and P. K. Liaw, "Twinning–detwinning behavior during fatigue-crack propagation in a wrought magnesium alloy AZ31B," *Mater. Sci. Eng. A*, vol. 556, pp. 278–286, Oct. 2012.
[79] L. Wu *et al.*, "Fatigue-Property Enhancement of Magnesium Alloy, AZ31B, through Equal-Channel-Angular Pressing," *Metall. Mater. Trans. A*, vol. 38, no. 13, pp. 2283–2289, Sep. 2007.
[80] Y. Durandet, R. Deam, A. Beer, W. Song, and S. Blacket, "Laser assisted self-pierce riveting of AZ31 magnesium alloy strips," *Mater. Des.*, vol. 31, pp. S13–S16, Jun. 2010.
[81] T. J. Franklin, J. Pan, M. Santella, and T.-Y. Pan, "Fatigue Behavior of Dissimilar Ultrasonic Spot Welds in Lap-Shear Specimens of Magnesium and Steel Sheets," *SAE Int. J. Mater. Manuf.*, vol. 4, no. 1, pp. 581–588, Apr. 2011.
[82] V. K. Patel, S. D. Bhole, and D. L. Chen, "Fatigue life estimation of ultrasonic spot welded Mg alloy joints," *Mater. Des. 1980-2015*, vol. 62, pp. 124–132, Oct. 2014.
[83] S. M. Chowdhury, D. L. Chen, S. D. Bhole, E. Powidajko, D. C. Weckman, and Y. Zhou, "Microstructure and Mechanical Properties of Fiber-Laser-Welded and Diode-Laser-Welded AZ31 Magnesium Alloy," *Metall. Mater. Trans. A*, vol. 42, no. 7, pp. 1974–1989, Jul. 2011.
[84] W. Xu, L. Liu, Y. Zhou, H. Mori, and D. L. Chen, "Tensile and fatigue properties of weld-bonded and adhesive-bonded magnesium alloy joints," *Mater. Sci. Eng. A*, vol. 563, pp. 125–132, Feb. 2013.
[85] R. Alderliesten, C. Rans, and R. Benedictus, "The applicability of magnesium based Fibre Metal Laminates in aerospace structures," *Compos. Sci. Technol.*, vol. 68, no. 14, pp. 2983–2993, Nov. 2008.
[86] T. Pärnänen, R. Alderliesten, C. Rans, T. Brander, and O. Saarela, "Applicability of AZ31B-H24 magnesium in Fibre Metal Laminates – An experimental impact research," *Compos. Part Appl. Sci. Manuf.*, vol. 43, no. 9, pp. 1578–1586, Sep. 2012.
[87] M. Sadighi, T. Pärnänen, R. C. Alderliesten, M. Sayeaftabi, and R. Benedictus, "Experimental and Numerical Investigation of Metal Type and Thickness Effects on the Impact Resistance of Fiber Metal Laminates," *Appl. Compos. Mater.*, vol. 19, no. 3–4, pp. 545–559, Jun. 2012.
[88] G. E. Dieter, *Mechanical metallurgy*. McGraw-Hill, 1961.
[89] R. W. Hertzberg, R. P. Vinci, and J. L. Hertzberg, *Deformation and Fracture Mechanics of Engineering Materials*, 5th ed. Wiley, 2012.
[90] H. Neuber, "Theory of Stress Concentration for Shear-Strained Prismatical Bodies With Arbitrary Nonlinear Stress-Strain Law," *J. Appl. Mech.*, vol. 28, no. 4, pp. 544–550, Dec. 1961.
[91] K. Molski and G. Glinka, "A method of elastic-plastic stress and strain calculation at a notch root," *Mater. Sci. Eng.*, vol. 50, no. 1, pp. 93–100, Sep. 1981.

[92] T. H. Topper, R. M. Wetzel, and J. Morrow, "Neuber's rule applied to fatigue of notched specimens," Defense Technical Information Center, Fort Belvoir, VA, Jun. 1967.
[93] J. Denk, J. Dallmeier, O. Huber, and H. Saage, "The fatigue life of notched magnesium sheet metals with emphasis on the effect of bands of twinned grains," *Int. J. Fatigue*, vol. 98, pp. 212–222, May 2017.
[94] J. Denk, L. Whitmore, O. Huber, O. Diwald, and H. Saage, "Concept of the highly strained volume for fatigue modeling of wrought magnesium alloys," *Int. J. Fatigue*, vol. 117, pp. 283–291, Dec. 2018.
[95] Ö. Karakas, "Consideration of mean-stress effects on fatigue life of welded magnesium joints by the application of the Smith–Watson–Topper and reference radius concepts," *Int. J. Fatigue*, vol. 49, pp. 1–17, Apr. 2013.
[96] C. M. Sonsino, W. Fricke, F. de Bruyne, A. Hoppe, A. Ahmadi, and G. Zhang, "Notch stress concepts for the fatigue assessment of welded joints – Background and applications," *Int. J. Fatigue*, vol. 34, no. 1, pp. 2–16, Jan. 2012.
[97] D. Radaj, C. Sonsino, and W. Fricke, *Fatigue Assessment of Welded Joints By Local Approaches*, 2nd ed. Woodhead Publishing and CRC Press, 2006.
[98] B. Kondori, T. F. Morgeneyer, L. Helfen, and A. A. Benzerga, "Void growth and coalescence in a magnesium alloy studied by synchrotron radiation laminography," *Acta Mater.*, vol. 155, pp. 80–94, Aug. 2018.
[99] J. Dallmeier and O. Huber, "Comparison of Numerical Fatigue Analysis with Experimental Results on AZ31 Magnesium Alloy Sheet Metal Structures," 2012.
[100] K. N. Smith, P. Watson, and T. H. Topper, "A stress-strain function for the fatigue of metals," *J. Mater.*, 1970.
[101] L. F. J. Coffin, "A study of the effects of cyclic thermal stresses on a ductile metal," *Trans. ASME*, 1954.
[102] S. S. Manson, "Behavior of materials under conditions of thermal stress," National Advisory Committee for Aeronautics, NACA TN-2933, 1953.
[103] H. Jahed and A. Varvani-Farahani, "Upper and lower fatigue life limits model using energy-based fatigue properties," *Int. J. Fatigue*, vol. 28, no. 5–6, pp. 467–473, May 2006.
[104] H. Jahed, A. Varvani-Farahani, M. Noban, and I. Khalaji, "An energy-based fatigue life assessment model for various metallic materials under proportional and non-proportional loading conditions," *Int. J. Fatigue*, vol. 29, no. 4, pp. 647–655, Apr. 2007.
[105] M. Matsuishi and T. Endo, "Fatigue of metals subjected to varying stress," *Jpn. Soc. Mech. Eng.*, 1968.
[106] M. A. Miner, "Cumulative damage in fatigue," *J. Appl. Mech.*, 1945.
[107] K. Walker, "The Effect of Stress Ratio During Crack Propagation and Fatigue for 2024-T3 and 7075-T6 Aluminum," in *Effects of Environment and Complex Load History on Fatigue Life*, M. Rosenfeld, Ed. 100 Barr Harbor Drive, PO Box C700, West Conshohocken, PA 19428-2959: ASTM International, 1970, pp. 1-1–14.
[108] S.-H. Kim, B.-S. You, C. Dong Yim, and Y.-M. Seo, "Texture and microstructure changes in asymmetrically hot rolled AZ31 magnesium alloy sheets," *Mater. Lett.*, vol. 59, no. 29–30, pp. 3876–3880, Dec. 2005.
[109] O. Duygulu and S. R. Agnew, "The Effect of Temperature and Strain Rate on the Tensile Properties of Textured Magnesium Alloy AZ31B Sheet," p. 6, 2003.
[110] S. R. Agnew and Ö. Duygulu, "Plastic anisotropy and the role of non-basal slip in magnesium alloy AZ31B," *Int. J. Plast.*, vol. 21, no. 6, pp. 1161–1193, Jun. 2005.

[111] H. Wang, P. D. Wu, and M. A. Gharghouri, "Effects of basal texture on mechanical behaviour of magnesium alloy AZ31B sheet," *Mater. Sci. Eng. A*, vol. 527, no. 15, pp. 3588–3594, Jun. 2010.
[112] B. Roebuck, J. D. Lord, M. Brooks, M. S. Loveday, C. M. Sellars, and R. W. Evans, "Measurement of flow stress in hot axisymmetric compression tests," *Mater. High Temp.*, vol. 23, no. 2, pp. 59–83, Jan. 2006.
[113] M. Knezevic, A. Levinson, R. Harris, R. K. Mishra, R. D. Doherty, and S. R. Kalidindi, "Deformation twinning in AZ31: Influence on strain hardening and texture evolution," *Acta Mater.*, vol. 58, no. 19, pp. 6230–6242, Nov. 2010.
[114] X. Lou, M. Li, R. Boger, S. Agnew, and R. Wagoner, "Hardening evolution of AZ31B Mg sheet," *Int. J. Plast.*, vol. 23, no. 1, pp. 44–86, Jan. 2007.
[115] M. Matsuzuki and S. Horibe, "Analysis of fatigue damage process in magnesium alloy AZ31," *Mater. Sci. Eng. A*, vol. 504, no. 1–2, pp. 169–174, Mar. 2009.
[116] S. Hasegawa, Y. Tsuchida, H. Yano, and M. Matsui, "Evaluation of low cycle fatigue life in AZ31 magnesium alloy," *Int. J. Fatigue*, vol. 29, no. 9–11, pp. 1839–1845, Sep. 2007.
[117] M. Huppmann, M. Lentz, S. Chedid, and W. Reimers, "Analyses of deformation twinning in the extruded magnesium alloy AZ31 after compressive and cyclic loading," *J. Mater. Sci.*, vol. 46, no. 4, pp. 938–950, Feb. 2011.
[118] S. Begum, D. Chen, S. Xu, and A. Luo, "Low cycle fatigue properties of an extruded AZ31 magnesium alloy," *Int. J. Fatigue*, vol. 31, no. 4, pp. 726–735, Apr. 2009.
[119] M. R. Barnett, Z. Keshavarz, A. G. Beer, and D. Atwell, "Influence of grain size on the compressive deformation of wrought Mg–3Al–1Zn," *Acta Mater.*, vol. 52, no. 17, pp. 5093–5103, Oct. 2004.
[120] M. R. Barnett, "Twinning and the ductility of magnesium alloys Part II. 'Contraction' twins," *Mater. Sci. Eng. A*, p. 9, 2007.
[121] S. Xu, V. Y. Gertsman, J. Li, J. P. Thomson, and M. Sahoo, "Role of mechanical twinning in tensile compressive yield asymmetry of die cast Mg alloys," *Can. Metall. Q.*, vol. 44, no. 2, pp. 155–166, Jan. 2005.
[122] M. Noban and H. Jahed, "Ratchetting strain prediction," *Int. J. Press. Vessels Pip.*, vol. 84, no. 4, pp. 223–233, Apr. 2007.
[123] T. Tang, S. Kim, and M. F. Horstemeyer, "Fatigue crack growth in magnesium single crystals under cyclic loading: Molecular dynamics simulation," *Comput. Mater. Sci.*, vol. 48, no. 2, pp. 426–439, Apr. 2010.
[124] X. S. Wang, F. Liang, J. H. Fan, and F. H. Zhang, "Low-cycle fatigue small crack initiation and propagation behaviour of cast magnesium alloys based on in-situ SEM observations," *Philos. Mag.*, vol. 86, no. 11, pp. 1581–1596, Apr. 2006.
[125] O. Cazacu, B. Plunkett, and F. Barlat, "Orthotropic yield criterion for hexagonal closed packed metals," *Int. J. Plast.*, vol. 22, no. 7, pp. 1171–1194, Jul. 2006.
[126] "LS-DYNA keyword user's manual volume II: material models." Livermore Software Technology Corporation (LSTC).
[127] R. von Mises, "Mechanik der festen Körper im plastisch-deformablen Zustand," *Nachrichten Von Ges. Wiss. Zu Gött. Math.-Phys. Kl.*, pp. 582–592, 1913.
[128] M. A. Khayamian, B. Behravesh, and H. Jahed, "Incorporation of asymmetric yield and hardening behaviour in axisymmetric elastoplastic problems," *Mater. Des.*, vol. 99, pp. 490–499, Jun. 2016.
[129] J. Morrow, "Fatigue properties of metals," in *Fatigue Design Handbook*, Warrendale, PA: Society of Automotive Engineers, 1968.

[130] F. Lorenzo and C. Laird, “A new approach to predicting fatigue life behavior under the action of mean stresses,” *Mater. Sci. Eng.*, vol. 62, no. 2, pp. 205–210, Feb. 1984.
[131] K. Tokaji, M. Kamakura, Y. Ishiizumi, and N. Hasegawa, “Fatigue behaviour and fracture mechanism of a rolled AZ31 magnesium alloy,” *Int. J. Fatigue*, vol. 26, no. 11, pp. 1217–1224, Nov. 2004.
[132] S. Ishihara, Z. Nan, and T. Goshima, “Effect of microstructure on fatigue behavior of AZ31 magnesium alloy,” *Mater. Sci. Eng. A*, vol. 468–470, pp. 214–222, Nov. 2007.
[133] A. N. Chamos, S. G. Pantelakis, G. N. Haidemenopoulos, and E. Kamoutsi, “Tensile and fatigue behaviour of wrought magnesium alloys AZ31 and AZ61,” *Fatigue Fract. Eng. Mater. Struct.*, vol. 31, no. 9, pp. 812–821, Sep. 2008.
[134] A. N. Chamos, S. G. Pantelakis, and V. Spiliadis, “Fatigue behaviour of bare and pre-corroded magnesium alloy AZ31,” *Mater. Des.*, vol. 31, no. 9, pp. 4130–4137, Oct. 2010.
[135] C. Potzies and K. U. Kainer, “Fatigue of Magnesium Alloys,” *Adv. Eng. Mater.*, vol. 6, no. 5, pp. 281–289, May 2004.
[136] A. Ince and G. Glinka, “A modification of Morrow and Smith-Watson-Topper mean stress correction models,” *Fatigue Fract. Eng. Mater. Struct.*, vol. 34, no. 11, pp. 854–867, Nov. 2011.
[137] S. H. Park, S.-G. Hong, B. Ho Lee, W. Bang, and C. S. Lee, “Low-cycle fatigue characteristics of rolled Mg–3Al–1Zn alloy,” *Int. J. Fatigue*, vol. 32, no. 11, pp. 1835–1842, Nov. 2010.
[138] V. V. Ogarevic and R. I. Stephens, “Fatigue of Magnesium Alloys,” p. 38, 1990.
[139] A. V. Beck, *The technology of magnesium and its alloys*. FA Hughes & Company Limited, 1943.
[140] G. H. Found, “The notch sensitivity in fatigue loading of some magnesium-base and aluminum-base alloys - discussion,” *Proc. - Am. Soc. Test. Mater.*, vol. 46, pp. 715–740, 1946.
[141] L. Jackson and H. Grover, “The fatigue strength of some magnesium sheet alloys - discussion,” *Proc. - Am. Soc. Test. Mater.*, vol. 46, pp. 783–798, 1946.
[142] T. Oberg and W. Trapp, “High Stress Fatigue of Aluminium and Magnesium Alloys,” *Prod. Eng.*, vol. 22, no. 2, pp. 159–163, 1951.
[143] Y. C. Lin, Z.-H. Liu, X.-M. Chen, and J. Chen, “Stress-based fatigue life prediction models for AZ31B magnesium alloy under single-step and multi-step asymmetric stress-controlled cyclic loadings,” *Comput. Mater. Sci.*, vol. 73, pp. 128–138, Jun. 2013.
[144] Y. Liu, G. Kang, and Q. Gao, “A multiaxial stress-based fatigue failure model considering ratchetting–fatigue interaction,” *Int. J. Fatigue*, vol. 32, no. 4, pp. 678–684, Apr. 2010.
[145] J. Dallmeier, J. Denk, O. Huber, H. Saage, and K. Eigenfeld, “A phenomenological stress–strain model for wrought magnesium alloys under elastoplastic strain-controlled variable amplitude loading,” *Int. J. Fatigue*, vol. 80, pp. 306–323, Nov. 2015.

Appendix A: Specimen specifications

All dimensions in millimetres.

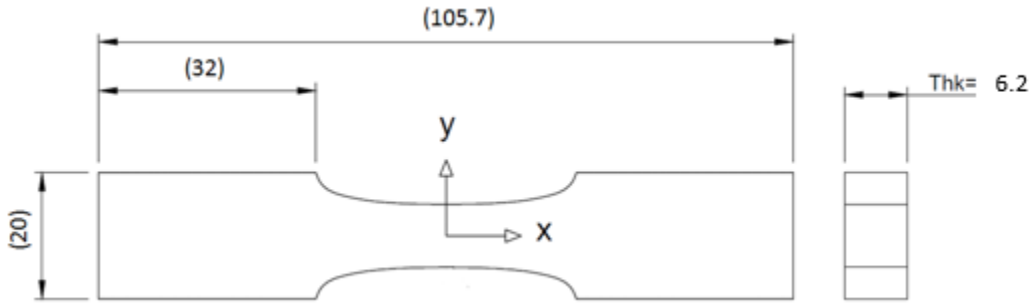

Figure 47 Dimensions and tolerances of smooth tensile specimen, which is designed at FATSLAB.

Table 17 Coordinates of points defining outline of smooth specimens.

x (mm)	y (mm)
0	5
1.14	5
2.28	5.01
3.42	5.02
4.56	5.04
5.7	5.07
6.85	5.11
8	5.17
9.15	5.25
10.33	5.33
11.51	5.45
12.72	5.61
13.95	5.81
15.23	6.05
16.53	6.35
17.8	6.74

x (mm)	y (mm)
17.8	6.74
18.91	7.28
19.6	7.84
20	8.29
20.4	8.89
20.85	10
52.85	10
52.85	0
17.8	6.74
18.91	7.28
19.6	7.84
20	8.29
20.4	8.89
20.85	10
52.85	10
52.85	0

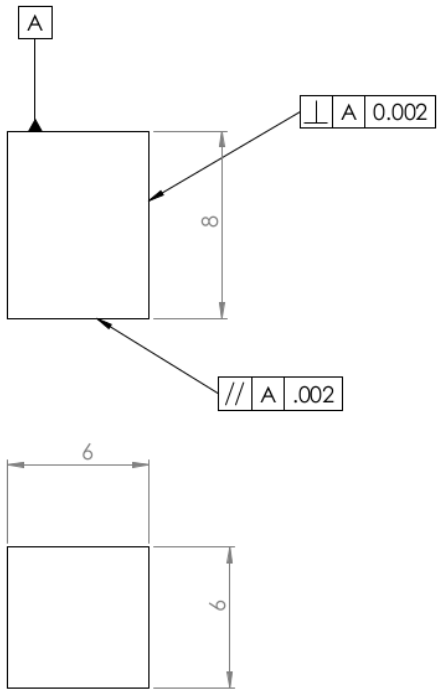

Figure 48 Dimensions and tolerances of compressive specimen.

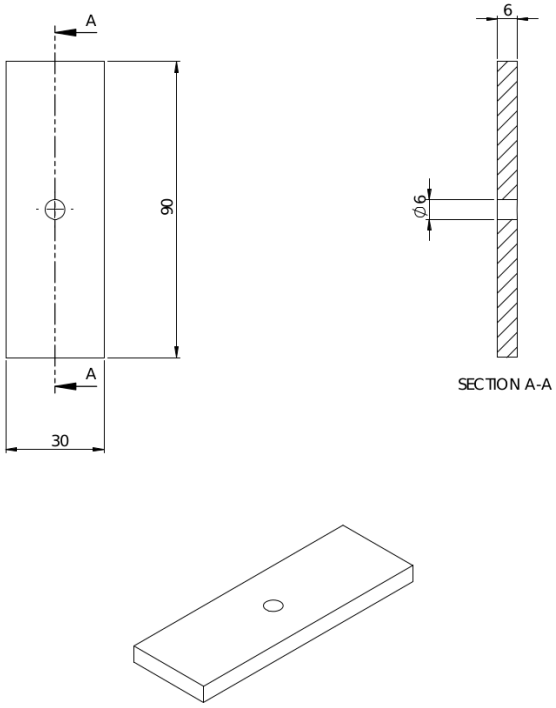

Figure 49 Dimensions of notched specimen.

Appendix B: LS-DYNA material cards

MAT_124 material card

```
*MAT_PLASTICITY_COMPRESSION_TENSION_TITLE
QUASISTATIC_AZ31B-H24_MAT_124
$#     mid        ro         e        pr         c         p      fail      tdel
        10   0.00177   43705.0      0.35       0.0       0.0 1.00000E20       0.0
$#   lcidc     lcidt     lcsrc     lcsrt    srflag    lcfail        ec      rpct
        11        13         0         0       0.0         0       0.0       0.0
$#      pc        pt     pcutc     pcutt     pcutf
       0.0       0.0       0.0       0.0       0.0
$#       k
       0.0
```

MAT_233 material card

```
*MAT_CAZACU_BARLAT_MAGNESIUM_TITLE
QUASISTATIC_AZ31B-H24_MAT_233
$#     mid        ro         e        pr        hr        p1        p2      iter
         8   0.00177   43705.0      0.35       3.0       0.0       0.0       0.0
$#       a       c11       c22       c33      lcid        e0         k        p3
       2.0   1.22475   1.22475   1.22475        13       0.0       0.0       0.0
$#    aopt                                    c12       c13       c23       c44
       2.0       0.0       0.0       0.0       0.0       0.0       0.0       0.0
$#                                   a1        a2        a3
         0         0         0       1.0       0.0       0.0
$#      v1        v2        v3        d1        d2        d3      beta       fit
       0.0       0.0       0.0       0.0       1.0       0.0       0.0         0
$#   lc1id     lc2id    numint     lccid    icflag    idflag     lc3id     epsfg
         0         0       0.0        11         1         0         0       0.0
```